HIGH TEMPERATURE OXIDATION OF SILICA FORMERS IN DISSOCIATED OXYGEN

By

Nirav D. Vora

Dissertation

Submitted to the Faculty of the

Graduate School of Vanderbilt University

in partial fulfillment of the requirements

for the degree of

DOCTOR OF PHILOSOPHY

in

Chemical Engineering

May 2009

Nashville, Tennessee

Approved:

Dr. Bridget R. Rogers

Dr. Ken A. Debelak

Dr. Kane Jennings

Dr. M. Douglas LeVan

Dr. D. Greg Walker

I dedicate this work to my family, who have supported me throughout my career as a graduate student

ACKNOWLEDGEMENTS

I acknowledge my adviser Dr. Bridget Rogers and Dr. Jochen Marschall and Dr. Dusan Pejakovic of the Molecular Physics laboratory at SRI for their support and guidance throughout this work. My thanks to the group members Mekha George, Bob Geil, Ben Schmidt, James Burst, and Zhe Song for their support. I would also like to thank the National Science Foundation and AFOSR for financially supporting this work.

TABLE OF CONTENTS

Page

Chapter

LIST OF TABLES

LIST OF FIGURES

Figure Page

LIST OF ABBREVIATION

UHTC	Ultra High Temperature ceramic Composites
CVD	Chemical Vapor Deposition
LPCVD	Low Pressure Chemical Vapor Deposition
NRA	Nuclear Reaction Analysis
SCCM	Standard Cubic Centimeter per Minute
MWP	Microwave Power
PMT	Photo-Multiplier
LIF	Laser Induced Fluorescence
UV	Ultra Violet
SE	Spectroscopic Ellipsometry
RBS	Rutherford Backscattering Spectrometry
FEM	Finite Element Method
PDE	Partial Differential Equation
GCI	Grid Convergence Index
OC	Order of Convergence

CHAPTER I

INTRODUCTION

The new generation of hypersonic vehicles being developed has sharp leading edges to increase the maneuverability. During atmospheric reentry the temperature at the leading edge is inversely proportional to the square root of the radius of curvature of the edge [1]. A leading edge with a small radius of curvature will thus result in high temperatures leading to dissociation of oxygen and nitrogen molecules in the surrounding environment during the reentry. The dissociated oxygen and nitrogen atoms recombine exothermically on the surface of the vehicle downstream, and thus significantly add to the heat load [2]. Ultra-high temperature ceramic composites (UHTCs) are being considered as potential construction material for these vehicles. Since the UHTC oxides have lower thermal conductivity and emittance than the virgin material, they are less able to dissipate this heat load by conduction inwards or by radiation back to the environment. This can raise the surface temperature into the ultra-high temperature range, i.e., above 1873 K (1600 ºC), and possibly exceed 2473 K (2200 ºC). Extensive research [3] is being carried out to develop materials that have the required combination of thermal, mechanical and chemical properties that enable sustained operation in this temperature range optimally without extra cooling required which would add to the weight of the vehicle.

UHTCs like ZrB_2-SiC and HfB_2-SiC composites are potential candidates for this application. This is because of their enhanced oxidation resistance as a result of formation of a borosilicate scale on the virgin material when oxidized. Oxidation of UHTCs has been studied in both thermal furnaces [4] and arc-jet facilities [5]. However, neither the arc jet nor the thermal studies sufficiently replicate the environment UHTCs are exposed to during reentry. The oxidation in a thermal furnace does not account for the effect of dissociated oxygen even at high temperatures, whereas the arc-jet dissociates most of the oxygen molecules.

Two important factors contributing to the oxidation of UHTCs during the atmospheric reentry are the supersonic flow environment (e.g. surface shear stresses and transport of reactants and products across shock and boundary layers) and partially dissociated oxygen chemistry. We are studying the oxidation properties of UHTCs and their base materials in a quartz flow reactor coupled with a microwave discharge to distinguish the partially dissociated oxygen chemistry effects from the supersonic flow environment. The discharge dissociates a fraction of the oxygen molecules and the samples are oxidized in the plasma afterglow. The samples sit downstream from the discharge to avoid any charged species produced in the discharge from reaching the sample. Varying the power input to the discharge controls the ratio of O atoms to oxygen molecules at the inlet of the reactor.

Understanding the oxidation mechanism of UHTCs in the high temperature partially dissociated environment requires understanding the oxidation mechanism of its base materials under the same environment. The presented work focuses on studying the oxidation mechanism of silica formers (Si, Si_3N_4, and SiC) in high temperature flowing oxygen plasma afterglow. As will be discussed in chapter II, a parallel oxidation model has been used in this work to account for simultaneous oxidation by both molecular and atomic oxygen. Chapter III describes in detail the experimental set-up used to generate the partially dissociated oxygen environment.

To determine the quantitative effect of O atom on the oxidation mechanism, it is necessary to accurately know the flux of O atoms reaching the sample. The O atoms formed in the discharge will recombine in the gas phase and on the walls of the reactor. Rate of this recombination is affected by the non-isothermal flow characteristics of the system. A detailed numerical model is required to take into consideration both radial and axial concentration gradients due to the non-isothermal nature of the flow apart from the gradient due to temperature dependent gas phase and surface recombinations and diffusion. A semi-empirical finite element model is used for representing such a system. The model takes concentration and temperature measurements at the inlet and pressure measurements at the outlet as inputs and solves for temperature, velocity, and concentration profiles within the reactor system, as detailed in Chapter IV. Chapter V discusses the validation of the reactor model and also the O atom concentration profiles calculated for oxidation conditions.

This calculated O atom concentration near the sample is then used to determine its quantitative effect on the oxidation process of Si, Si_3N_4, and SiC by incorporating it in the oxidation model as an input. Chapter VI discusses the results from the oxidation experiments and fitting of the oxidation model to this data. Conclusions based on these results are discussed in chapter VII.

CHAPTER II

OXIDATION

Oxidation of ZrB_2-SiC composite

Significant effort has been put into the development of ZrB_2-SiC composite for potential application in space shuttles. ZrB_2 with a melting point of ~ 3000 K is a good candidate for high temperature use by itself. Oxidation of ZrB_2 below 1373 K (1100 ºC) results in the formation of ZrO_2(s) and B_2O_3(l) [6]. The B_2O_3(l) forms a protective layer over the ZrO_2 layer and acts as a diffusion barrier to oxygen. But B_2O_3(l) evaporates above 1373 K (1100 ºC) and the rate of removal reaches the rate of formation at 1673 K (1400 ºC), thus decreasing the effectiveness of the barrier layer. Addition of SiC to ZrB_2 (ZrB_2 + 20 vol % SiC composite) resulted in improved oxidation resistance [7]. This improvement was a result of the formation of a protective borosilicate glass layer [8] due to the interaction of B_2O_3(l) with amorphous SiO_2.

Oxidation of ZrB_2-SiC composite in air above 1773 K (1500 ºC) results in the formation of a SiC depleted layer in the composite as shown in Figure 1. This layer is formed between the ZrB_2-SiC substrate and a mixed oxide (ZrO_2-SiO_2) layer. Fahrenholtz [9] explained this SiC depleted layer formation through a thermodynamic analysis of the oxidation process in air at 1773 K (1500 ºC). According to his analysis, the partial pressure of O_2 in this layer at the temperature considered is low enough to result in the active oxidation of SiC and prevent ZrB_2 from oxidizing. Active oxidation refers to the etching of the SiC (or for that matter Si) to form SiO(g) and CO(g) (in case of SiC) as opposed to formation of condensed layer of SiO_2 (passive oxidation). The SiO(g) formed diffuses upwards and combines with the inward diffusing oxidant to form condensed phase SiO_2 in the mixed oxide layer on top of the SiC depleted layer. Thus the global effect of this active oxidation of SiC is the formation of a passive SiO_2 layer. The problem arises when the CO(g) formed and trapped in the SiC depletion layer reaches a critical pressure and ruptures the protective scale. This limits the structural strength of the material.

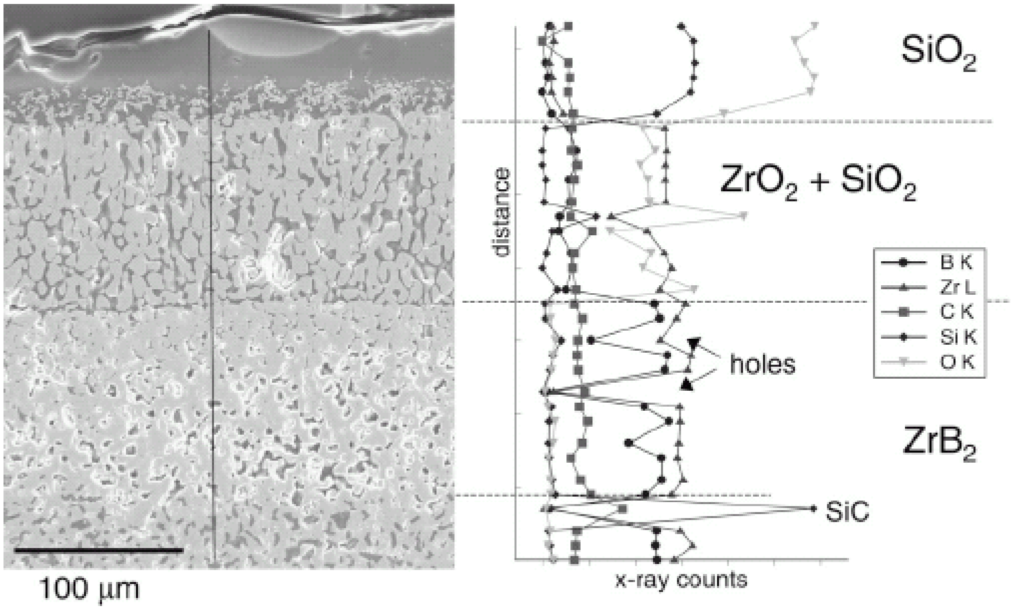

Figure 1: SEM micrograph and XEDS line scan of the sample after oxidation in air at 1900 K (1627 ºC) for 10 10-min cycles [10].

To understand the oxidation mechanism of these composites in the application environment, i.e. in presence of O atom, it is necessary to understand the mechanism of oxidation of their base materials in similar environments. This work discusses the oxidation mechanism of silica formers (Si, Si_3N_4, and SiC) in partially dissociated oxygen environments. Such an analysis in conjunction with an analysis of the oxidation mechanism of ZrB_2 in similar environment will enable the understanding of ZrB_2-SiC oxidation in the application environment.

Oxidation of Si

A linear–parabolic model proposed by Deal and Grove [11] is commonly used to describe thermal oxidation of Si (100) in O_2 over a temperature range of 973 K–1573 K (700°C-1300°C) and a pressure range of 0.1–1 atm (passive oxidation regime). This model was developed based on the following mechanism, (i) transport of O_2 from the gas bulk to the oxide surface, (ii) transport of O_2 molecules through the interstitials of the oxide layer, and (iii) its subsequent reaction with silicon at the oxide/Si interface. This model captures the initial linear regime and the later parabolic behavior experimentally observed. Mathematically this model can be described as,

$$t_{ox}^2 + A t_{ox} = B(t + \tau) \tag{1.a}$$

$$A = 2 D_{eff}\left(1/k + 1/h\right) \tag{1.b}$$

$$B = 2 D_{eff} C^* / N_{ox} \tag{1.c}$$

where, t_{ox} is the oxide thickness at any time t, τ is the time shift due to any initial oxide present, D_{eff} is the effective diffusivity of the oxidant through the oxide layer, C^* is the equilibrium concentration of the oxidant (O_2) in the oxide layer, N_{ox} is the number of the oxidant molecules incorporated in a unit oxide volume, k is the rate constant for the interface reaction, and h is the gas phase transport coefficient.

The model's limitation is its failure to describe the growth of oxide films less than 20 nm in dry oxidation. Much effort has been put into explaining this initial oxide growth phase. Irene [12,13] proposed a modified linear-parabolic model which considers transport in micro pores and the visco-elastic properties of silica to explain the initial growth regime. According to this model the initial oxide film is non-uniform resulting in the formation of micro pores, which offer less resistance to the diffusion of O_2. Thus the oxidation is essentially controlled by the surface reaction, resulting in the initial linear growth regime. This continues until the oxide film grows thicker and more uniform resulting in a transport controlled oxidation. This model provides a fair qualitative and conceptual assessment of the oxidation process, but was unsuccessful quantitatively due to lack of information regarding the viscosity and residual stress in SiO_2 films during oxidation. Doremus [14] explored the effect of strain produced in the oxide during growth and concluded that it reduces the diffusivity of O_2 giving rise to parabolic diffusion controlled growth in the later stages. Almeida and coworkers [15] assumed the reaction between O_2 and Si to be taking place in a reactive layer (oxide of varying stoichiometry) rather than at a sharp oxide/Si interface. Their model assumes the oxidation process to be transient, unlike the above-mentioned models. The reactive layer (defined by the simultaneous presence of both reacted and un-reacted Si in the model) is formed as a solution to the governing transient partial differential equations (PDEs). This model did fit the data better than the Deal-Grove model, but it predicts a much thicker reactive layer than the measurements reported in the literature [16].

All of the above models assume oxidation by just one oxidizing species, i.e. molecular oxygen. There is another school of thought that the limitations of the Deal-Grove model can be overcome by considering simultaneous oxidation due to more than one oxidizing species. Such a parallel oxidation mechanism was first discussed qualitatively by Hopper and coworkers [17] to describe the entire oxide growth. Revesz and coworkers [18] proposed a model with two components of the diffusive flux, one independent and another dependent of the oxide thickness. Based on their analysis they physically justified the independent and dependent components of the diffusive flux as that representing the transport of molecular and ionic oxygen in the oxide, respectively. They found that this model gives a better fit to the data than the Deal Grove model.

This idea was also explored by Han and Helms [19]. They proposed atomic oxygen or oxygen vacancies in the oxide structure as the second diffusing species, the first one being molecular oxygen. According to this model the total oxidation rate for two non-interacting oxidants can be expressed as

$$\frac{d\,t_{ox}}{dt} = \frac{B_1}{2L + A_1} + \frac{B_2}{2L + A_2} \qquad (2)$$

In the above equation the *B*'s and *A*'s have corresponding definition with the physical parameters in the Deal-Grove model and L represents the oxide thickness. Such a parallel oxidation model can be used to understand the effect of O atoms on oxidation of Si in partially dissociated oxygen environments (containing both O atoms and O_2).

Silicon oxidation in partially dissociated oxygen has not been studied as extensively as that in molecular oxygen. A mixed O_2/O atom oxidation mechanism would involve transport of O atom to the oxide surface and its diffusion through the oxide scale for subsequent reaction with the Si in addition to the steps involved for molecular O_2. Peeters and coworkers [20] presented a model for the oxidation of Si in oxygen plasma afterglow which assumed O atoms were the only oxidizing species. They assumed the fast diffusion of unbound O atoms through the oxide layer and their incorporation into the network at the oxide/Si interface to be responsible for the oxidation. However, recent computational studies [21-23] indicate that molecular oxygen is energetically more favored in the oxide interstitials than atomic oxygen and diffusion of atomic species will result in exchange with the oxide network. Peeters and coworkers did consider the recombination of diffusing O atoms in the oxide bulk to form O_2 molecules. If O_2 formed by recombination was responsible for oxidation, the solubility limit of O_2 in the oxide would drive less O_2 to enter the oxide from gas phase. This would not lead to experimentally observed exaggerated growth. Tatsumura and coworkers [24] proved experimentally that the incorporation of O atoms in the oxide network modifies the network. An analysis was carried out assuming that this network modification increases the solubility of O_2 in the oxide layer, as detailed in Chapter VI. The increased solubility could not explain the exaggerated growth.

The transport mechanism of O_2 and O atoms through the oxide network can be explored further with the tracer experiments carried out in dry thermal and partially dissociated oxygen environments, respectively. Results from tracer experiments [25,26] in dry $^{18}O_2$ environments suggest that permeation of molecular oxygen through the oxide interstices (without any interaction with the oxide structure) and its subsequent reaction with the Si at the oxide/Si interface is primarily responsible for dry thermal oxidation of silicon, as assumed by the Deal Grove model [11]. Most (93%) of the ^{18}O tracer was found near at near the oxide/Si interface and the rest at the gas/oxide interface.

Tracer studies in partially dissociated oxygen environments showed that ^{18}O atoms were seen throughout the existing oxide scale even without any additional oxide growth [27]. This indicates rapid diffusion of O atoms through the network. Hoff and coworkers [28] have reported a dependence of oxide thickness (caused by transport of O atoms through the network) on the free O atom concentration in the gas phase at constant process conditions in the 673 K–973 K (400 °C–700 °C) temperature range and was also seen in this work at 1323 K (1050 °C) as will be discussed later. Furthermore, in the tracer experiments [27] the % of ^{18}O in the oxide near the gas/oxide interface was found to be the same as that in the gas phase initially. The % of ^{18}O in the oxide bulk was found lesser than that at the surface. But with time, the % of ^{18}O in the oxide bulk increased depending on its proximity to the gas/oxide interface. Eventually it was the same as that in the gas phase throughout the oxide. This suggests that the transport of O atoms takes place by incorporation at the surface and subsequent diffusion towards the oxide/Si interface. Therefore there was more ^{18}O near the gas/oxide interface than in the bulk initially in the oxidation process. This mechanism was also confirmed by Tatsumura and coworkers [24] using X-ray diffraction analysis. So the oxidation process of Si can be seen as resulting from simultaneous transport of O_2 through the interstitials and O atoms through the network and their subsequent reaction with Si at the oxide/Si interface.

To take into consideration the parallel diffusion of the two oxidizing species, as shown in Figure 2, a parallel oxidation model is used to fit our data. The following mass balances (diffusion of the oxidizing species) in the oxide scale can mathematically present such a steady state model,

$$D_O \frac{\partial^2 c_O}{\partial x^2} = 0 \tag{3.a}$$

$$D_{O2} \frac{\partial^2 c_{O2}}{\partial x^2} = 0 \tag{3.b}$$

where, c_o and c_{o2} are the concentrations in (mol/m^3) and D_o and D_{o2} are the diffusivities in m^2/s of O and O_2, respectively. Both the oxidants are assumed to diffuse through the oxide scale before reacting with Si at the oxide/Si interface.

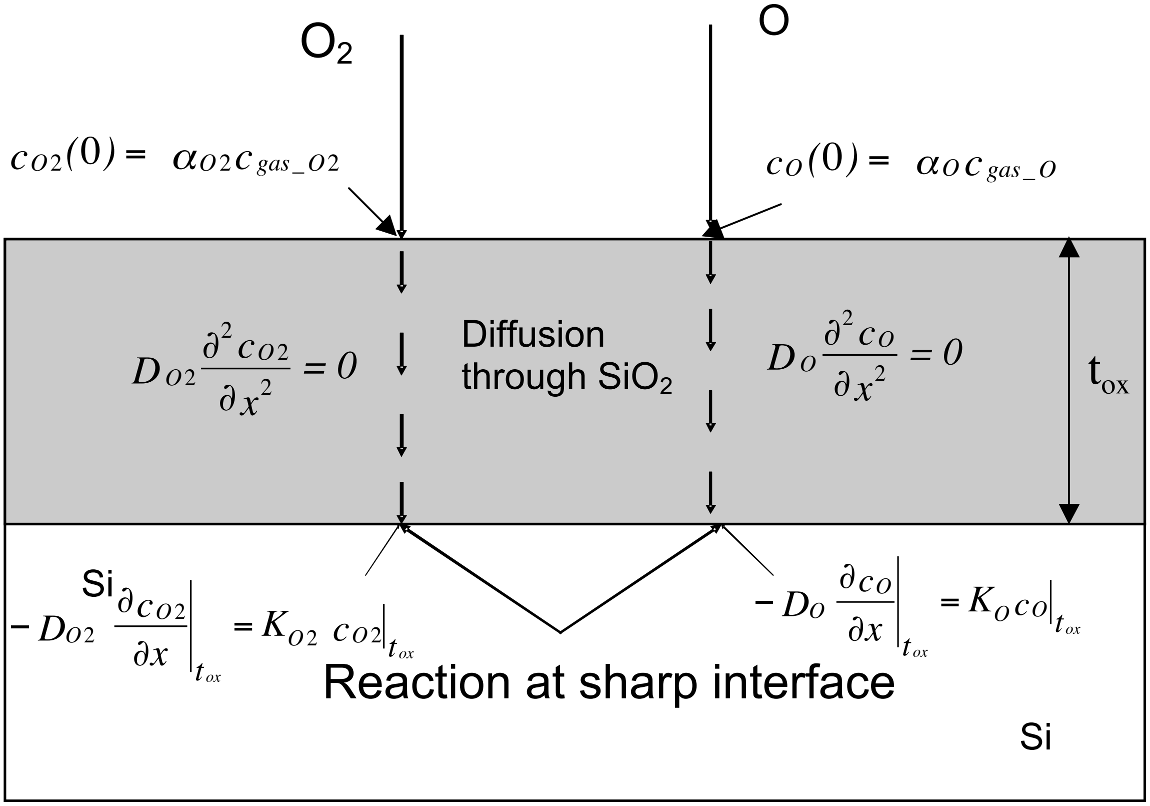

Figure 2: Proposed mechanism of parallel oxidation of Si (100) by O_2 and O atom in oxygen plasma afterglow.

The above equations are then solved by assuming saturation concentration of the oxidizing species at the gas/oxide interface and reaction of the diffusing oxidizing species at the oxide/Si interface with Si.

These boundary equations are mathematically described as shown below,

$$c_O(0) = \alpha_O c_{gas\_O}, \quad -D_O \left. \frac{\partial c_O}{\partial x} \right|_{t_{ox}} = K_O \left. c_O \right|_{t_{ox}} \tag{4.a}$$

$$c_{O2}(0) = \alpha_{O2} c_{gas\_O2}, \quad -D_{O2} \left.\frac{\partial c_{O2}}{\partial x}\right|_{t_{ox}} = K_{O2}\, c_{O2}\Big|_{t_{ox}} \qquad (4.b)$$

where, t_{ox} is the oxide thickness in m, α_o is the incorporation probability of O atoms and α_{o2} is the solubility of O_2 in SiO_2, K_O and K_{O2} are the rate constants in m/s for the reaction of O atoms and O_2 respectively with the Si at the oxide/Si interface, and c_{gas_O} and c_{gas_O2} are the average bulk O atom and O_2 concentration above the sample surface. The incorporation probability of O atoms, α_o, is defined as the ratio of the O atoms incorporated at the oxide surface (for subsequent diffusion in to the oxide) to that available near the oxide surface. The above steady state equations are then solved for various time periods and the increment in thickness Δt_{ox} (in meters) after each time interval is calculated as

$$\Delta t_{ox} = \frac{M_{SiO_2}}{\rho_{SiO_2}}\left[J_{O_2} + \frac{1}{2}J_O\right]\Delta t \qquad (5)$$

where, M_{SiO2} (60 g/mol) and ρ_{SiO2} (2.2×10^6 g/m^3) are the molecular weight and density of SiO_2 in and, Δt is the time interval in s, and J_{O2} and J_O are the fluxes in mol/(m^2.s) of O_2 and O atoms respectively at the oxide/Si interface.

This oxidation model will be used to determine the significance of each species in the oxidation process. Previous work on plasma afterglow oxidation have assumed O atom concentrations near the sample based on the measurements at the entrance of the reactor. In this work we determine the O atom concentration near the sample surface using a semi-empirical model of the reactor, discussed in following chapters.

Oxidation of Si_3N_4

Dry thermal oxidation of Si_3N_4 has typically been studied over a temperature range of 1273 K–1673 K (1000 °C–1400 °C) [29-35]. The oxidation rate of Si_3N_4 in O_2 was found to be significantly lower and the activation energy higher than that for Si both for crystalline [31,35] and non-crystalline [34] Si_3N_4. We studied dry thermal oxidation of n type Si and amorphous Si_3N_4 film at 1183 K (910 °C) [36]. Significantly lower oxide thickness on Si_3N_4 was observed as compared to that on Si at constant process conditions. The steps involved in oxidation of Si_3N_4 are, (i) transport of O_2 from the gas bulk to the oxide surface, (ii) transport of O_2 molecules through the interstitials of the oxide layer, (iii) its subsequent reaction with un-reacted Si_3N_4 at the Si_3N_4/oxide interface, and (iv) out-diffusion of by-products through the oxide scale into the gas phase. The lower oxidation rate of Si_3N_4 compared to Si has been explained in several ways.

Du and coworkers [31] performed oxidation studies on crystalline CVD Si_3N_4 at atmospheric pressure in the temperature range of 1273 K–1673 K (1000 °C–1400 °C). They attributed the lower oxidation rate to lower diffusivity of O_2 through the oxide scale. They claimed the lower diffusivity was the result of a Si_2N_2O formed between the bulk Si_3N_4 substrate and SiO_2. This layer would have a higher resistance to diffusion of oxygen than the silica layer. It is possible that the slower diffusion of O_2 is a result of the out-diffusion of the by-product N_2, which is absent in the oxidation of Si. But Du and coworkers claimed that formation of a single scale of SiO_2 and out-diffusion of N_2 through this scale could not account for the retarded growth rate. This theory of slow diffusion through the oxynitride layer (diffusion controlled oxidation rate) was then showed by Luthra and coworkers [37,38] to yield N_2 pressures of ~ 10^{24} bar (at 1400 °C) at the SiO_2/SiN_2O_2 interface. So they neglected the presence of the oxynitride layer in their analysis. They considered the partial pressure gradients of various species across the oxide scale and argued that if the diffusion of either O_2 and or N_2 is the rate-limiting step by itself then the oxidation rate of Si_3N_4 should be same as that for Si. They also argued that if the oxidation rate was limited by the interfacial reaction the rate could be lower relative to Si, but would follow a linear trend and not the observed parabolic trend. Therefore they proposed a simultaneous control by both an interface reaction and diffusion. They also analyzed this mixed control system and found that a nearly parabolic law is possible for a mixed interface-reaction/nitrogen-diffusion controlled mechanism [38].

Ogbuji et.al [39] compared the models proposed by Du [31] and Luthra [38] (for oxidation of single crystal Si_3N_4) and found that the model proposed by Du better fits the experimental results better than Luthra's model. They attributed the problem of high N_2 pressures at the interface to the assumption of reaction at a sharp interface [32]. To support this, they carried out compositional depth profiles [33] using Auger electron spectroscopy (AES) and Rutherford backscattering spectrometry (RBS). Based on their observations they suggested that the oxide layer is not divided into two discrete layers of SiO_2 and Si_2N_2O as suggested by Du and coworkers, but has a composition that changes continuously from SiO_2 near the surface to Si_3N_4 near the substrate. They suggested a qualitative model involving progressive replacement of N by O in a $SiN_{2-n}O_{2+n}$ tetrahedral, with n as a function of depth. The slow growth rate was attributed to the varying diffusivity of O_2 in this sub-oxide (diffusion controlled oxidation rate), which is highest for SiO_2 and decreases as N content increases.

Sheldon [40] described a transient model (unlike the models described above, which were steady state) for the dry thermal oxidation of Si_3N_4. He represented the oxy-nitride using the formula $Si_3N_{4(1-n)}O_{6n}$. This formula describes the entire range of oxy-nitride stoichiometry ranging from SiO_2 for n = 1 to Si_3N_4 for n = 0. He solved the model as a system of coupled PDEs solving for n and O_2 concentration. He did not include N_2 concentration in the system, assuming that its outward diffusion is much faster than inward diffusion of O_2 and hence is not the rate limiting step. In absence of any experimental data on the variation of diffusivity and solubility of O_2 with the oxy-nitride composition (n) he assumed them to vary between that for SiO_2 and Si_3N_4 using a functional form based on ‘n’ as shown below.

$$\alpha(n) = \alpha(n=0)\left[\frac{\alpha(n=1)}{\alpha(=0)}\right]^n \tag{6}$$

$$D(n) = D(n=0)\left[\frac{D(n=1)}{D(n=0)}\right]^n \tag{7}$$

He also assumed that the ratio of the solubility of O_2 in SiO_2 and Si_3N_4 is the same as the ratio of the diffusivities of O_2 in those two. This model does address the problem of unrealistic N_2 pressures at the oxide/substrate interface using the mixed control (by diffusion and reaction in the oxide) theory that Luthra [38] proposed. Although this model takes into consideration the graded stoichiometry of the oxy-nitride layer and the resolves the problem of excess N_2 pressure at the interface, it still makes many simplifying assumptions as described above. This could be eliminated by more detailed experimental data such as compositional depth profiles across the oxy-nitride layer and the dependence of diffusivity and solubility of O_2 on composition.

No attempts have been made so far to model the oxidation of Si_3N_4 in an oxygen plasma afterglow. Apart from the steps involved for oxidation of Si_3N_4 in O_2, oxidation in plasma afterglow will involve transport of O atom to the oxide surface and its diffusion through the oxide scale for subsequent reaction with Si_3N_4.

There is sparse data available for the oxidation of Si_3N_4 in oxygen plasma containing charged species. Kennedy and coworkers [41] carried out oxidation of low-pressure chemical vapor deposited (LPCVD) thin Si_3N_4 films in plasma environment at 673 K (400 ºC). Using Auger electron spectroscopy (AES) they found that the oxidized films had a three layer structure with a SiO_2 – like layer at the surface and near the Si substrate and a Si_3N_4 - like structure between them. Jimenez and coworkers [42] analyzed the oxidation of chemical vapor deposited (CVD) thin Si_3N_4 films in oxygen plasma environment using ^{18}O tracer. They used nuclear reaction analysis (NRA) to determine the ^{18}O depth profiles in the oxidized samples. Based on ^{18}O profiles in the oxide layer they claimed the absence of the oxy-nitride interlayer for as high as 1073 K (800 °C), but also expressed their concern regarding the poor depth resolution of NRA. But the fact that oxidation rates and activation energy were similar to that for Si under similar condition, points towards the absence of the interlayer which is primarily considered responsible for the slower oxidation rates of dry thermal oxidation rates of Si_3N_4.

This similarity between the oxidation rates of Si_3N_4 and Si was found true also in our initial studies [43] of oxidation of Si_3N_4 in a plasma afterglow at 1183 K (910 ºC). Comparable oxide thicknesses were found on Si(100) and CVD Si_3N_4 at constant process conditions (an order of magnitude greater than that for dry thermal oxidation of Si(100)), when oxidized in the afterglow. This indicates that the oxidation mechanism in Si_3N_4 is similar to that for Si in plasma afterglow. Thus the same parallel oxidation model used for Si can be used for Si_3N_4 too.

Oxidation of SiC

High temperature oxidation studies on single crystal as well as poly-crystalline SiC have been generally aimed at understanding the passive-to-active transition at various pressures [44-50]. Much discrepancy has been reported regarding the transition temperature and pressure conditions in both experimental and theoretical work. The differences in the theoretical results arise from different enthalpies and the diffusion coefficients used. The discrepancies in experimental results arise due to factors such as the gas compositions, total pressures, flow rates used, processing method of the SiC oxidized, and the criterion indicating of the transition (presence of bubbles, mass changes, or only presence of the silica layer, etc.).

We did not observe bubbles, but observed an exaggerated oxide growth indicating passive oxidation during our experiments. The passive oxidation studies in the literature indicate that the oxide growth is a strong function of the crystal orientation of SiC and is different from that for CVD (polycrystalline) SiC like that used in our work. Passive oxidation studies on CVD SiC have been carried out in the temperature range of 1473 K–1773 K (1200 ºC–1500 ºC) and at atmospheric pressure by Ogbuji and coworkers [51] and Fox [52]. Ogbuji and coworkers reported an activation energy of 120 kJ/mol over the entire temperature range studied similar to that of Si oxidation as predicted by the Deal-Grove [11]. This indicates that the interstitial diffusion of O_2 through the oxide layer is responsible for the oxidation process. Fox reported activation energy of 190 kJ/mol and claimed that the mechanism of oxidation is likely a combination of molecular oxygen diffusion and network exchange of oxygen ions over the entire temperature range studied.

Furthermore, in our studies we found the oxide thickness to be comparable to that of Si and Si_3N_4 under similar conditions. This suggests that the oxidation mechanism is similar in all three cases. Therefore oxidation of SiC will also be analyzed using the same parallel oxidation model as described before.

CHAPTER III

EXPERIMENTAL DETAILS

Oxidation experiments

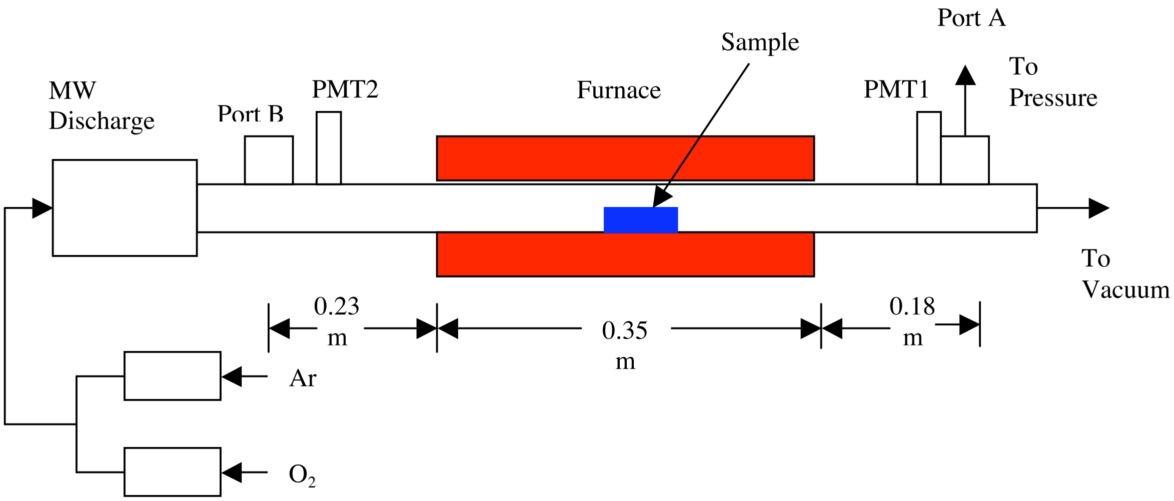

Figure 3: Schematic of the experimental set-up used for oxidation experiments.

Oxidation of n-type Si (100), CVD SiC, and low-pressure chemical vapor deposition (LPCVD) Si_3N_4 was studied. Both the SiC and Si_3N_4 films were deposited on silicon wafers. The SiC films were polycrystalline with a nominal thickness of 630 nm. The Si_3N_4 films were amorphous with a nominal thickness of 143 nm.

The experimental set-up for carrying out oxidation experiments at various temperatures, pressure, and oxygen dissociation fractions is shown in Figure 3. It consists of a 2.2 cms diameter quartz tube downstream to a 6 kW microwave discharge. A tube furnace is used to heat a 0.35 m section of the flow tube, 0.23 m downstream from port B. The sample was cleaned with methanol and placed on an alumina substrate and then placed at the middle of the furnace. At this position the sample is ~ 0.5 m away from the midpoint of microwave discharge cavity minimizing the flux of charged species reaching the sample. Electronic flow controllers are used to feed mixtures of oxygen (BOC gases, 99.994 %) and argon (BOC Gases, 99.999%) into the reactor. Gases are evacuated from the other end of the furnace using a roots blower pumping system. The gas velocity in the flow tube is on the order of tens of meters per second, minimizing the residence time thereby minimizing losses of atomic oxygen due to bulk and surface recombination. Experimental conditions used were 2300 sccm (standard cubic centimeter per minute) of 87%-13% Ar gas mixture, 431.3 Pa (3.2 Torr) outlet pressure, at temperatures of 1183 K (910 °C) and 1323 K (1050 °C), and at microwave powers (MWP) in the range of 1.2 kW–6 kW.

Pressure measurement

Gas pressures are measured at several locations using Baratron capacitance manometers. A 10-Torr pressure gauge is positioned to measure the pressure just before the throttle valve (not shown in the Figure) connecting the flow tube to the vacuum pump, where it serves as a reference for adjusting the pumping efficiency. A second 10-Torr pressure gauge is connected via a manifold to two ports, one located 0.23 m upstream of the furnace (port B) and another located 0.18 m downstream of the furnace (port A); the spacing between ports is 0.76 m. This second gauge is used to measure the pressure drop along the flow tube, which is used to validate the flow component of the model.

Temperature measurement

Gas temperature measurements are necessary to determine the total gas density and flow parameters at the entrance. Furthermore, wall temperature measurements are used as boundary conditions in the computational model. The temperatures (both gas and reactor wall) were measured using a bare 0.003" diameter type K thermocouple. The gas temperatures were also measured using nitrous oxide laser induced thermometry (NO-LIF) thermometry using the photomultiplier (PMT2) to determine the effect of O atom recombination on the thermocouple. This spectroscopic technique determines rotational temperature of the NO molecule in the $v = 0$ level of its ground state. It is assumed that this temperature is equal to the translational temperature of NO owing to a rapid rotational-translational energy transfer. Furthermore, it is assumed that NO is translationally equilibrated with the bulk gas in the flow tube.

O atom concentration measurement at the inlet

Centerline O atom concentrations near port B (PMT2) were measured using a combination of two techniques, NO titration [53] and two photon laser-induced fluorescence (LIF) [54,55]. The two photon LIF method is based on raising the atom to be detected from its ground state to the first electronically excited state of the same symmetry and multiplicity through the absorption of two ultraviolet photons of equal wavelength. This is followed by a transition to an excited state of opposite symmetry. During the process the excited atom emits an infrared photon, which constitutes the observed signal. The intensity of this signal is directly proportional to the number density of excited species in the analyzed gas volume.

Atomic oxygen is detected using UV radiation at 225.65 nm (vacuum wavelength) to excite ground state oxygen via the $3p\ ^3P_{1,2,0} \leftarrow 2p\ ^3P_2$ two-photon transition, with subsequent fluorescence at 844.87 nm via the $3p\ ^3P_{1,2,0} \rightarrow 3s\ ^3S_1^0$ transitions [56,57]. The $3p\ ^3P_{1,2,0}$ excited state has a radiative lifetime of about 35 ns [58]. The most recently measured values of the room temperature rate constants for quenching of O atoms on O_2 and Ar are approximately $9.4 \times 10^{-16}\ m^3s^{-1}$ and $1.4 \times 10^{-16}\ m^3s^{-1}$, respectively [58,59]. The atoms are excited using a tunable dye laser. PMT2 was used near port B of the reactor to measure the fluorescence. The O atom LIF signal is then converted to absolute concentrations at PMT2 by calibrating the detection system using NO titration as described below.

The NO titration method is based on flowing pure N_2 through the discharge and adding NO downstream to form O atoms as per the reaction,

$N + NO \rightarrow O + N_2$ (R1)

If more N atoms than NO molecules are present then they react with the formed O atoms via the reaction

$N + O + M \rightarrow NO^* + M$ (R2)

Addition of excess NO removes all the N atoms by the faster reaction (R1) and the O atoms formed then reacts with the excess titer NO as shown below,

$O + NO \rightarrow NO_2 + h\nu$ (R3)

Before the endpoint of the titration is reached one O atom is formed for each NO molecule added. The titration endpoint can be determined by increasing the flow of NO until a plateau in the O atom LIF signal (O atom density) is seen. The other indications of the endpoint are the disappearance of N atom LIF signal and the appearance of ground electronic state NO LIF signal. The N atom density near port B can thus be assigned to the number of molecules of NO added when the endpoint is reached. Since all the N atoms are converted to O atoms at the endpoint, the O atom LIF signal at the endpoint can be assigned to a known number density. The gas in the reactor is then immediately changed from N_2 to a standard O_2/Ar mixture used in the oxidation studies so that no time is allowed for laser beam alignment to change. The LIF signal measured is then compared with the LIF signal at the end point of the titration experiment to extract the O atom density near port B for standard conditions.

Calibration of the outlet

After, determining the O atom density near the entrance of the reactor (PMT2), the O atom density near the outlet (port A) was determined by calibrating port A with respect to PMT2 (near port B). There are many sources of difference between the signals at the two locations. The two ports have different O atom densities due to O atom recombination taking place in the region between them, and due to temperature and pressure differences. The differing process conditions at the two ports results in different rate coefficients for quenching of the fluorescing state in LIF. In addition, differences will be introduced due to sources inherent to the method used, such as different quantum efficiencies and amplification factors of the PMTs used at the two ports, the slightly different optical filter center wavelength and transmittance, different laser beam sizes due to imperfect collimation, and different solid angles used for detection.

Two-photon LIF from xenon near the two ports and O atom LIF signal at PMT2 were used to cross-calibrate the ports. The excitation processes for both Xe and O atom involves two photons, and their two two-photon resonances are very close. Therefore it can be assumed that excitation conditions in the two cases are identical. Furthermore, there will be no loss of Xe due to recombination in the region between the two ports. Any difference in the Xe LIF signals acquired at the two ports at the same pressure and temperature will be due to the sources inherent to the method. If fluorescence from O atoms and Xe is observed with the same excitation and same observation volume, then the ratio of the fluorescence signals from the two species can be expressed as [60]

$$\frac{S_{\mathrm{O}}}{S_{\mathrm{Xe}}} = \frac{[\mathrm{O}]_0}{[\mathrm{X}e]_0} \frac{\mathrm{T_O}}{\mathrm{T_{Xe}}} \frac{\eta_{\mathrm{O}}}{\eta_{\mathrm{Xe}}} \frac{\sigma_{\mathrm{O}}}{\sigma_{\mathrm{Xe}}} \frac{a_{\mathrm{O}}}{a_{\mathrm{Xe}}} \left(\frac{h\nu_{\mathrm{Xe}}}{h\nu_{\mathrm{O}}} \right)^2 \tag{8}$$

where, S is fluorescence signal integrated over fluorescence wavelength, excitation wavelength, and laser pulse time, and normalized to the square of laser pulse energy; $[..]_0$ is number density of ground-state atoms in the level from which excitation occurs (i.e., $J = 2$ level for O atom, while the Xe ground state is singlet); T is the transmittance of the filters used for fluorescence detection; η is the quantum efficiency of the PMT for the respective fluorescence wavelength; σ is the cross section for the two-photon excitation; ν is the excitation frequency; a is the branching ratio for the observed radiative transition (determined by the relative rates of spontaneous emission and collisional quenching of the excited state). Using Equation 8, an unknown O atom density can be extracted from the known xenon density and measured LIF signals from the two species. The accuracy of this approach is limited by the uncertainty in the values of the radiative lifetimes, two-photon absorption cross-sections, and rate coefficients for quenching of the fluorescing states used in the calculation.

In this work, absolute O atom density is determined at one location along the flow tube by NO titration, and calibration using Xe LIF is used only for *relative* calibration of the detection systems at two locations and for subsequent determination of the ratio of the O atom densities at the two locations. A very low mass flow of pure Xe (~2.5 sccm), with a low pumping speed is used. Under these conditions, the Xe pressures measured at ports A and B are nearly equal (about 1.2 Torr) and, consequently, the Xe densities at the two PMT locations are essentially equal. If the same PMT is used for LIF detection at ports A and B, the ratios of O atom and Xe energy-normalized LIF signals at the two ports can be written as,

$$\frac{S_{\mathrm{O}}^{\mathrm{A}}}{S_{\mathrm{Xe}}^{\mathrm{A}}} = \mathrm{T}_{\mathrm{A}}^{2} \frac{[\mathrm{O}]_0^{\mathrm{A}}}{[Xe]_0} \frac{\mathrm{T}_{\mathrm{O}}}{\mathrm{T}_{\mathrm{Xe}}} \frac{\eta_{\mathrm{O}}}{\eta_{\mathrm{Xe}}} \frac{\sigma_{\mathrm{O}}}{\sigma_{\mathrm{Xe}}} \frac{a_{\mathrm{O}}^{\mathrm{A}}}{a_{\mathrm{Xe}}} \left(\frac{h\nu_{\mathrm{Xe}}}{h\nu_{\mathrm{O}}} \right)^2, \quad \frac{S_{\mathrm{O}}^{\mathrm{B}}}{S_{\mathrm{Xe}}^{\mathrm{B}}} = \mathrm{T}_{\mathrm{B}}^{2} \frac{[\mathrm{O}]_0^{\mathrm{B}}}{[\mathrm{X}e]_0} \frac{\mathrm{T}_{\mathrm{O}}}{\mathrm{T}_{\mathrm{Xe}}} \frac{\eta_{\mathrm{O}}}{\eta_{\mathrm{Xe}}} \frac{\sigma_{\mathrm{O}}}{\sigma_{\mathrm{Xe}}} \frac{a_{\mathrm{O}}^{\mathrm{B}}}{a_{\mathrm{Xe}}} \left(\frac{h\nu_{\mathrm{Xe}}}{h\nu_{\mathrm{O}}} \right)^2 \tag{9}$$

These equations contain additional factors T^{A} and T^{B}, which represent transmittances (at the excitation beam wavelength) of the gas in the beam path between the front Brewster window and the respective ports. These transmittances are determined by the amount of ozone present in the flow tube, and they are measured independently, as described later. Combining equations (8) and (9), we have

$$\frac{[\mathrm{O}]_0^{\mathrm{A}}}{[\mathrm{O}]_0^{\mathrm{B}}} = \frac{S_{\mathrm{O}}^{\mathrm{A}}}{S_{\mathrm{O}}^{\mathrm{B}}} \frac{S_{\mathrm{Xe}}^{\mathrm{B}}}{S_{\mathrm{Xe}}^{\mathrm{A}}} \frac{a_{\mathrm{O}}^{\mathrm{B}}}{a_{\mathrm{O}}^{\mathrm{A}}} \left(\frac{\mathrm{T}^{\mathrm{B}}}{\mathrm{T}^{\mathrm{A}}} \right)^2 \tag{10}$$

In derivation of Equation 10, the effect of the finite laser line width on the excitation rate was neglected.

Average O_3 concentration measurements

O atoms in the reactor can recombine with the excess molecular oxygen to form O_3. Ozone formation has two unwanted effects. First, O_3 combines with O atom to form O_2 thus resulting in loss of O atoms. Secondly, it absorbs the UV laser beam used for the LIF measurements of O atom, thus interfering with the O atom measurements. The later phenomenon can be used to measure average O_3 concentrations in the reactor by UV absorption near 226 nm using the same laser system used for LIF measurements. Absorption by O atoms is avoided by tuning the wavelength slightly off the two-photon resonance. Any detected decrease in laser energy with the activation of the microwave discharge indicates the presence of ozone.

Spectroscopic ellipsometry

Spectroscopic Ellipsometry (SE) was used to determine oxide thicknesses on Si (100) and LPCVD Si_3N_4 substrates. The method involves focusing a polarized light on the sample to be analyzed. The measured change in polarization, both amplitude and phase, of the reflected light beam is then used to deduce the material properties [61].

A JA Woollam M2000 ellipsometer along with its software WVASE32® was used for analyzing the oxide films. Data for each sample was collected over a spectral range of 193 nm to 1100 nm. A Xenon lamp is used to produce the light, which is then polarized by passing it through a monochromator and then a polarizer. This light beam when focused on the sample reflects from the sample and enters a detector. The measurements are expressed in terms of ψ (amplitude ratio upon reflection) and Δ (phase shift) using the

Fresnel reflection equation for polarized light encountering boundaries in planar multilayered materials [62],

$$tan(\psi) \bullet e^{i\Delta} = \frac{r_p}{r_s} \tag{11}$$

where, r_p and r_s are the complex Fresnel reflection coefficients of the sample for p- (in the plane of incidence) and s- (perpendicular to the plane of incidence) polarized light. The measurements ψ and Δ are expressed in terms of optical constants (n and k) using the angle of incidence and the ratio of the Fresnel constants [63]. These optical parameters are a function of the wavelength, which makes ψ and Δ a function of wavelength too. A model is then developed which describes the thickness of the film as a function of its optical parameters. The thickness is then calculated by varying it and the optical constants to fit the model to the measured ψ and Δ vs. wavelength data.

The software WVASE32® has an extensive library of such relationships for various materials. The model is built bottom-up by specifying the relationship first for the substrate material and then for the individual films on the substrate. In this work a model was developed with fixed optical constants and thickness (1mm) for the Si substrate. The SiO_2 layer was modeled using a Cauchy relationship (with three adjustable parameters) [63] to describe the dispersion in optical constants. The model was then fitted to the acquired data using a non-linear regression analysis by varying the thickness and the adjustable parameters (of the Cauchy relationship) of the oxide film.

Rutherford Backscattering Spectrometry

Backscattering spectrometry involves accelerating energetic ions towards the sample to be analyzed and determining the material properties by counting the elastically backscattered ions as a function of energy. The number and energy of the ions backscattered from the sample allows identification of the atomic masses and determination of the distribution of constituent elements as a function of depth below the surface [64].

The number of ions backscattered from an element in the target sample depends on the scattering cross-section of that element for a particular incident energy and the number of atoms of that element present in the sample. Scattering cross-section is the probability that an incident ion will be backscattered from an element at the detector solid angle. If the force between the incident and target nuclei is assumed to be Coulomb force, then the cross-section is called the Rutherford cross-section. Hence, the name Rutherford backscattering spectroscopy (RBS). Values of Rutherford cross-sections for various elements at various incident energies and detector solid angles are documented in the literature [64].

The energy of an incident ion backscattered from an atom (for a perfectly elastic collision) is proportional to the incident energy. The constant of proportionality is called the kinematic factor. The kinematic factor depends on the masses of the incident ion, the target atom, and the detection geometry. Values of kinematic factors for various incident ions and target elements at various detection angles are documented in the literature [64]. The energy of the backscattered ions also depends on the energy lost while traveling, into and out of the sample. This loss of energy can be calculated using the stopping powers [64] of the constituent elements. The elemental composition of the sample (thin film) as a function of depth is then determined by plotting the counts of backscattered ions at various backscattered energies (backscattering spectrum).

RBS analysis was performed using the Van de Graff accelerator at Vanderbilt University, using He^{4+} ions with an incident energy of 1.8 MeV. A surface barrier detector placed ~180 ° relative to the target normal was used to measure the counts and energy of the backscattered ions. A backscattering spectrum was simulated for the sample analyzed using an application package Particle-Solid Tools, written using Mathematica by Robert A. Weller [65]. The software contains a library of the Rutherford cross-sections, kinematic factors, and stopping powers. The thickness of the thin oxide film was determined by fitting the simulated spectrum (for assumed stoichiometry and density of the oxide) to the measured spectrum. A sample of the spectrum fitted to the data collected for a 180 nm thick oxide film on CVD SiC is as shown in Figure 4. In the figure each channel on the X-axis represents 4.2 eV. So a channel number 100 represents 420 eV.

The spectrum consists of a leading silicon edge resulting from the ions backscattered from the Si atoms of the SiC substrate. The second edge at lower energy is due to the ions backscattered from the Si atoms in the oxide layer. A peak for oxygen, the width of which depends on the oxide thickness, follows this. A carbon edge is seen at lower energies, as the kinematic factor is the lowest for carbon.

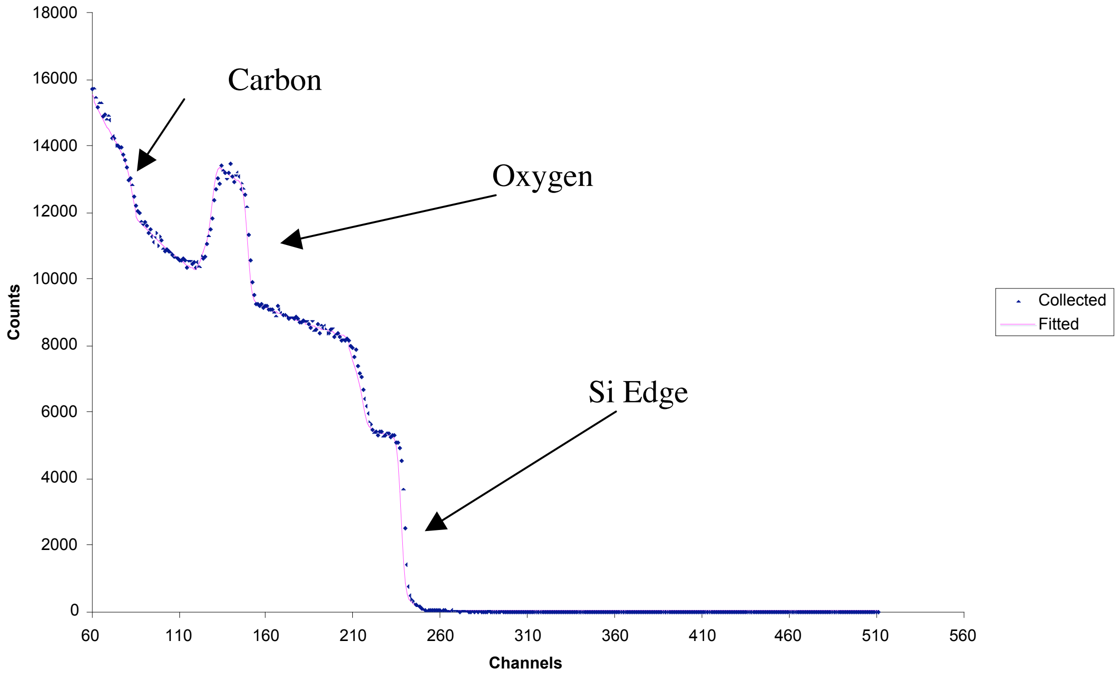

Figure 4: Collected and simulated backscattering spectrum for a 180 nm thick oxide film on the CVD SiC substrate.

CHAPTER IV

REACTOR FINITE ELEMENT MODEL

This finite element model for the reactor combines the non-isothermal compressible flow in the reactor with the high temperature oxygen plasma afterglow chemistry. The goal of the model was to determine the flux of O atoms reaching the surface and not the amount consumed by the sample, and so the reactor is modeled, both experimentally and computationally, without a sample in it. Since no sample is included in the experimental characterization procedure and since the reactor is just a cylindrical quartz tube without any internal barriers to the flow, an axis-symmetric model was used to model the system. Thus the model will hold irrespective of the sample being oxidized and can be used to understand the effect of O atoms on oxidation properties of various materials provided the flow conditions and the microwave discharge power is known.

Equation system

The flow in the system under relevant temperature and pressure conditions was found to be continuous (Knudsen number = 2.82×10^{-3}), laminar (Reynolds number = 50-160), and compressible (due to the non-isothermal nature of the system). This multi-component reactive compressible flow is represented by the partial differential equations (PDEs) shown in Table 1.

Table 1: General equations representing a reactive, laminar, and non-isothermal compressible flow

Equations	
Momentum balance & Continuity equation	$\rho \frac{Dv}{Dt} = -\nabla p - [\nabla \bullet \tau] + \rho g$ $\frac{\partial c}{\partial t} + (\nabla \bullet cv) = \sum_{i=1}^{n} R_i$
Energy balance	$0 = -\nabla.e + v.\nabla p + \tau : \nabla v$
Mass balance	$\nabla \bullet (c_i v) = \nabla \bullet (D_i \nabla c_i) + R_i$

In the above equations, v is the velocity in m/s, p is the pressure in Pa, ρ is the density in kg/m^3, τ is the viscous stress in kg/m^2/s, c is the total concentration in mol/m^3, R_i is the rate of generation of species "i" in mol/m^3/s, c_i = concentration of species "i", D_i is the diffusivity of species "i" in the carrier gas in m^2/s, $\nabla \bullet e$ is the energy flux due to diffusion and convection of various species in the system, $v \bullet \nabla p$ is the work required to compress the fluid (the compressibility term), and $\tau : \nabla v$ is the viscous dissipation, or the conversion of kinetic energy to heat due to internal friction in the fluid.

The terms representing compressibility and viscous dissipation are neglected in the incompressible Navier-Stokes equation as well as in non-isothermal flows with low temperature changes ~ 30K. In the later case the change in density of the fluid due to change in temperature is taken into account by the Boussinesq approximation [66]. This approximation considers constant thermo-physical quantities and takes into account the density change only in the body force term of the momentum equations. This approximation requires that $\Delta\rho/\rho << 1$, which is not true in our case as the temperature changes are on the scale of 1000 K and hence $\Delta\rho/\rho > 1$. Taking into consideration the above arguments, the above equations can be written for an axis-symmetric cylindrical system as shown in Table 2. In the above equations, v_r and v_z are the r and z components of the velocity in m/s, μ is the viscosity of the gas mixture in Pa.s, k is the thermal conductivity of the gas mixture in W/m°K, N_{ir} and N_{iz} are the total flux components of the i^{th} species in the r and z directions respectively in mol/m^2/s, H_i is the enthalpy of the i^{th} species in J/mol, and Cp_i is the specific heat of species *"i"* in J/mol/K.

The thermo-physical quantities, viscosities, thermal conductivities, and heat capacities, for various species were determined using the correlations from the literature [67-69]. The diffusivity of O atoms in O_2 (D_o) was calculated as a function of temperature and pressure using the empirical relations suggested by Pallix and coworkers [70]. The correlations used to calculate the above quantities are discussed in Appendix A.

Assumptions

Molecular oxygen constitutes ~ 87% of the gas mixture entering the microwave discharge. The maximum dissociation fraction of O_2 at maximum microwave discharge power was found to be ~ 0.05 from the O-atom measurement at PMT2. The dissociation in the microwave discharge is the most significant sink of O_2 in the system and also O_2 will be generated due to O atom recombination in the afterglow. So there will be an insignificant decrease in O_2 concentration in the reactor at a particular temperature and pressure and thus it is assumed to be the carrier gas. Other species are assumed to diffuse only in the carrier gas and inter-diffusivities are neglected.

Table 2: Equations representing a reactive, laminar, and non-isothermal compressible flow, simplified for an axis-symmetric cylindrical flow

Equation
Momentum balance r – component $-\frac{4}{3}\mu\frac{\partial^2 v_r}{\partial r^2}-\mu\frac{\partial^2 vr}{\partial z^2}=-\frac{\partial p}{\partial r}+\frac{\partial vr}{\partial r}\left[\frac{2\mu}{3r}-\rho vr\right]-\frac{\partial vz}{\partial z}\left[\frac{2\mu}{3r}\right]+\frac{\partial^2 vz}{\partial z\partial r}\left[\frac{\mu}{3}\right]+\rho g_r-\rho vz\frac{\partial vr}{\partial z}$ z – component $-\frac{4}{3}\mu\frac{\partial^2 v_z}{\partial z^2}-\mu\frac{\partial^2 vz}{\partial r^2}=-\frac{\partial p}{\partial z}+\frac{\partial vz}{\partial r}\left[\frac{\mu}{r}-\rho vr\right]+\frac{\partial vr}{\partial z}\left[\frac{\mu}{3r}\right]+\frac{\partial^2 vr}{\partial z\partial r}\left[\frac{\mu}{3}\right]-\rho vz\frac{\partial vz}{\partial z}$ Continuity equation $c\left[\frac{\partial v_r}{\partial r}+\frac{v_r}{r}+\frac{\partial v_z}{\partial z}\right]+v_r\frac{\partial c}{\partial r}+v_z\frac{\partial c}{\partial z}=R_O+R_{O2}+R_{O3}$
Energy balance $k\left(\frac{\partial^2 T}{\partial z^2}+\frac{\partial^2 T}{\partial r^2}\right)=\sum_{i=1}^{2}\left[\frac{\partial(N_{ir}H_i)}{\partial r}+\frac{\partial(N_{iz}H_i)}{\partial z}+\frac{N_{ir}H_i}{r}\right]-v_z\frac{\partial p}{\partial z}-v_r\frac{\partial p}{\partial r}$ $+\mu\left[2\left[\left(\frac{\partial v_z}{\partial z}\right)^2+\left(\frac{\partial v_r}{\partial r}\right)^2\right]+\left[\frac{\partial v_z}{\partial r}+\frac{\partial v_r}{\partial z}\right]^2-\frac{2}{3}\left[\frac{\partial v_z}{\partial z}+\frac{\partial v_r}{\partial r}\right]^2\right]$ *where*, $N_{iz}=-cD\nabla x_i+x_i c v_z$, $N_{ir}=-cD\nabla x_i+x_i c v_r$, $H_i=C_{pi}(T-298)$
Individual Mass balance $c_i\left[\frac{\partial v_r}{\partial r}+\frac{v_r}{r}+\frac{\partial v_z}{\partial z}\right]+v_r\frac{\partial c_i}{\partial r}+v_z\frac{\partial c_i}{\partial z}=D_i\left[\frac{\partial^2 c_i}{\partial r^2}+\frac{1}{r}\frac{\partial c_i}{\partial r}+\frac{\partial^2 c_i}{\partial z^2}\right]-R_i$

Boundary conditions

The above equations were solved using the boundary conditions shown in Table 3. The momentum equation was solved using a parabolic velocity profile at the entrance, assuming a no-slip wall, and the measured outlet pressure (p_{outlet}). The mean velocity

(v_{mean}) at the entrance was calculated using the flow rate, mean inlet temperature, and the measured inlet pressure.

The energy equation was solved using a semi-empirical inlet temperature profile (T_{in}), inner wall temperature (T_{wall}), and assuming that the temperature at the outlet is affected primarily by convection. The gas leaving the microwave discharge was heated due to the discharge, with its temperature dependent on the microwave power (with no heating at 0% MWP). Furthermore, measurements at PMT2 indicate higher temperature at the center of the reactor than at the wall. A temperature profile (T_{in}) is calculated at the entrance (PMT2) varying between the measured centerline and wall temperature as will be discussed in Chapter V. The inner wall temperature was assumed to be equal to the measured outer wall temperature, i.e., the wall was considered isothermal in the radial direction. This assumption was supported by a low Biot number (Appendix A) of ~ 0.05, suggesting a negligible solid resistance to heat transfer as compared to the fluid resistance.

Table 3: Boundary conditions for the 2D axis-symmetry model

Equation	Entrance	Centerline	Wall	Outlet
Momentum balance	$v = 2v_{mean}(1-(r/R)^2)$	$dv/dr = 0$	$v = 0$	$p = p_{outlet}$
Energy balance	$T = T_{in}$	$dT/dr = 0$	$T = T_{wall}$	Diffusive flux = 0
Mass balance	$c_i = c_{io}(T)$	$dc_i/dr = 0$	$dc_{o3}/dr = dc_{ar}/dr = 0$ $D_o(dc_o/dr) = \gamma w c_o/4$	Diffusive flux = 0

The mass balance equations were solved using the measured centerline concentration (c_{io}) at the entrance, a reactive boundary condition at the wall for O atoms and a closed boundary for other species, and assuming diffusive fluxes to be insignificant at the outlet. The concentration of various species at the entrance is assumed to be dependent on the temperature as per the ideal gas law. Specifically, a mole fraction of O atoms at the entrance centerline was calculated by assigning the measured centerline concentration to the measured centerline temperature at the entrance. The concentration of individual species was then calculated by assuming the mole fraction to be constant in the radial direction at the entrance. Recombination of oxygen atoms on the walls in laminar flows have been modeled using a first order rate constant k_w [71]. The total number of wall recombinations per unit area are expressed as $\gamma \boldsymbol{N_o c_o}$, where γ is the recombination coefficient (fraction of collisions leading to recombination), N_o is the total number of collisions per unit area per sec and per unit concentration of O atom, and c_o is the concentration of O atoms at the wall. By kinetic theory of gases,

$$N_o = \frac{\overline{w_o}}{4} \tag{10}$$

$$\text{where,}\ \overline{w_o} = \left(\frac{8RT}{\pi M_o}\right)^{1/2} = 36.38\sqrt{T}\ \text{m/s} \quad \text{(thermal velocity of O atoms)} \tag{11}$$

The concentration at the wall in the laminar flow will depend only on the radial diffusion of oxygen atoms to the wall (negligible radial velocity). At steady state, the diffusive flux to the wall is equal to the reactive flux. Thus the reactive boundary condition can be written as,

$$D_{o-o2}\frac{dc_o}{dr} = \frac{-k_w c_o r}{2} = \frac{-\gamma \bar{w}_o c_o}{4} \tag{12}$$

The first order rate constant for the recombination of O atoms on the reactor wall is thus given as,

$$k_w = \frac{\gamma \bar{w}}{2r} \qquad (1/s) \tag{13}$$

High temperature plasma afterglow chemistry

In addition, the model contains the equations describing rate of generation/consumption of O atom, O_2, and O_3 as a function of temperature. Two types of reactions involving O atoms that can take place in the O-O_2-O_3-Ar mixture are the homogeneous recombination in the gas phase and the heterogeneous recombination on the wall. Two types of mechanisms are possible for homogeneous recombination, direct recombination and the ozone mechanism [71-73]. The direct recombination mechanism, as the name suggests, refers to direct recombination of two O atoms on a third body, i.e.

$O + O + M \rightarrow O_2 + M$, (R4)

where $M \equiv O, O_2, O_3$, and Ar

The third body can be any other atom or molecule in the system. The ozone mechanism refers to the loss of O-atoms via ozone formation as shown below,

$O + O_2 + M \rightarrow O_3 + M$ (R5)

$O + O_3 \rightarrow O_2 + O_2$ (R6)

$O_3 + M \rightarrow O_2 + O + M$ (R7)

where $M \equiv O, O_2, O_3$, and Ar

The rate data available for these reactions is widely variant. The variation arises due to factors such as the method used to study the reaction (shock tubes, flame studies, or flow tube reactors), method of concentration measurements, temperatures at which the studies were performed, etc. The relevant reactions for the considered pressure and temperature ranges and the corresponding reaction rates [72,74-80] suggested in the literature are shown in Table 4.

The model was solved by finite element method (FEM) software, COMSOL MULTIPHYSICS®. This software allows the user to specify their own partial differential equations and boundary conditions and solves them using the Galerkin's weighted residual method [81] as described below. It uses the MATLAB platform for assembling the FEM matrices.

Table 4: Reaction afterglow chemistry at the relevant pressure and temperature conditions

Reaction (M = O, O_2, O_3, Ar)	**Rate Coefficient**	**Uncertainty**
Direct Recombination: 1. $O + O + M \rightarrow O_2 + M$ [72]	$K1_{Ar} = 5.2 \times 10^{-35} \exp(900/T)$, $K1_{O} = K1_{O2} = K1_{O3} = K1_{Ar}$ [cm^6 molecule^{-2} s^{-1}]	20 % at 300 K 60 % at higher temperatures
Ozone Mechanism: 2. $O + O_2 + M \rightarrow O_3 + M$ [79]	$K2_{Ar} = 5.5 \times 10^{-34} \exp(T/300)^{-2.6}$, 300 K – 400 K $K2_{Ar} = 3 \times 10^{-35} \exp(300/T) \exp(637.2/T)$, 400 K – 700 K $K2_{Ar} = 5.2 \times 10^{-35} \exp(1000/T)$, 700 K – 2000 K $K2_{O2} = K2_{O} = K2_{O3} = 1.5 \times K2_{Ar}$ [cm^6 molecule^{-2} s^{-1}]	15 % at 400 K
3. $O + O_3 \rightarrow O_2 + O$ [74,80]	$K3 = 8 \times 10^{-12} \exp(-2060/T)$ [cm^3 molecule^{-1} s^{-1}]	15 % at 300 K ~ 100 % at 1000 K
4. $O_3 + M \rightarrow O_2 + O + M$ [76,78]	$K4_{O3} = 7.16 \times 10^{-10} \exp(-11180/T)$, [cm^6 molecule^{-2} s^{-1}] $K4_{Ar} = K4_{O3}/4$; $K4_{O2} = K4_{O} = K4_{O3}/2$	
Surface Reaction [75,77]: $O + O[Surface] \rightarrow O_2$	$K5 = gamma \times V_t/d$, [/s] Where gamma is the recombination coefficient at the surface, V_t is the thermal velocity of O atoms, and d is the internal diameter of the tube.	100 % at 300 K Rises at higher temperature

Finite Element Method (FEM)

The basic premise of FEM is that the system to be modeled can be approximated by replacing it with an assemblage of discrete interconnecting elements [82]. This is different from the finite difference method, which envisions the solution region as an array of grid points (nodes). While, finite difference method solves for the field variables (dependent variables) only at the nodes, FEM solves for them both at the nodes and between them (or within the elements). FEM also allows for different element sizes and shapes in the same model and thus is suited for modeling complex geometries. The assembly of the interconnected elements is called as the mesh. Furthermore, FEM allows the use of adaptive and deformed meshes for moving boundaries. A mesh can be either be structured (regular arrangement of similar elements) or unstructured depending on the complexity of the geometry being modeled. COMSOL MULTIPHYSICS® uses an unstructured mesh with triangular elements as default. A structured mesh made of rectangular elements was used in this work due to simplicity of the geometry.

This FEM discretization procedure reduces the problem to a finite number of unknowns by expressing the unknown dependent variables in terms of assumed approximating functions, also known as interpolating functions, within each element. The interpolating functions are defined in terms of the values of the dependent variables specified at nodes on the boundary of the element. Nodal values along with the interpolating functions describe the complete behavior of the dependent variables in an individual element. The dependent variables used to model the system under consideration, are v_r and v_z for the r and z components, respectively, of the momentum equation, p for the continuity equation, T for the energy equation, and c_o, c_{o3}, and c_{Ar} for the mass balances for O-atom, O_3, and Ar, respectively. O_2 being the carrier gas, its concentration is derived by subtracting concentration of other species from the total concentration. Based on the dependent variables used, the model can be termed as a velocity-pressure model or a mixed model as the velocity variables are mixed with a force-like variable, pressure.

Usually polynomials are used as interpolating functions since they are easy to integrate and differentiate. The degree of polynomials used depends on the number of nodes in each element, the number and nature of unknowns at each node, and certain continuity requirements. To be more specific, the dependent variables are required to be continuous and have continuous partial derivatives up through the order of the equation. In this work, second order Lagrange interpolating functions are used to represent the behavior of the dependent variables within an element, except for pressure, which was solved using a linear Lagrange interpolating function, because it is the dependent variable for a 1st order continuity equation.

The next step after choosing the element type and the interpolating function is to convert the governing PDEs into matrix equations. These equations express the properties of individual elements in terms of the dependent variables. This can be done using different approaches like the direct approach, variational approach, or the weighted residual approach [82]. COMSOL MULTIPHYSICS® does this using the Galerkin's weighted residual method [81]. The method involves calculating a residual by substituting a trial function in place of the dependent variable in a PDE and subsequently minimizing the residual. The residual is multiplied with a weight function (thus the name weighted residual method) and integrated over the domain. Integration converts the governing PDE along with its boundary conditions (also called as the *strong form*) into a *weak form*. The *weak form* does not require the dependent variables to be continuous and have continuous partial derivative up through the order of the equation as long as discontinuities are integrable, which is a *weaker* restriction.

To simplify the process, COMSOL MULTIPHYSICS® assumes the weight function to be the same as the trial function (Galerkin's method). The trial and weight functions are then defined as a series of the interpolating function used for the model such that the series will have a non-zero value only for the element under consideration. This series is then substituted into the residual weight equation and the latter is then minimized with respect to the dependent variables. This minimization reduces the system of equations into simultaneous algebraic equations. This procedure is followed for each governing PDE. All the resulting simultaneous equations (for all PDEs) resulting from the above procedure are then assembled into a matrix form. These system equations are then modified to take into consideration the boundary conditions. COMSOL MULTIPHYSICS® does this by using Lagrange multipliers [81], a method used to deal with equality constraints in optimization problems.

The equations are then solved to determine the set of values of dependent variables at each node and within the elements, which minimizes the residual. Since more than one such minimum is possible, the equations are solved using a set of initial guesses, based on the user's judgment of the behavior of the system. COMSOL MULTIPHYSICS® uses an affine invariant Newton method [83] to solve this coupled system of highly non-linear stationary PDEs. The above procedure thus solves for the set of values of dependent variables over the entire solution region that will minimize the weighted residual.

CHAPTER V

REACTOR CHARACTERIZATION

This chapter starts with a discussion on the results from the computational and experimental characterization of the reactor. Continuous non-isothermal compressible flow and the high temperature oxygen plasma afterglow chemistry are the two constituents of the model. The flow component significantly effects the O atom concentration in the system. Therefore the model was first developed with a focus on the fluid dynamics. The high temperature oxygen plasma afterglow chemistry was then added to the validated flow model. The model was solved for the process conditions at which experimental data were available.

Verification of the flow component

Before modeling the various process conditions in the reactor, the flow was first verified with the Hagen – Poiseuille (HP) equation as shown below.

$$\dot{m} = \left[\frac{\pi R^4 M_{mix}}{8\mu_{mix} rT}\right]\frac{P_{in} - P_{out}}{L_R}\left[\frac{P_{in} + P_{out}}{2} + \frac{\mu_{mix}}{R}\sqrt{\frac{8\pi rT}{M_{mix}}}\right] \tag{14}$$

In the above equation, m is the mass flow rate in kg/s, R is the universal gas constant in J/K/kmol, M_{mix} is the molecular weight of the gas mixture in kg/kmol, μ_{mix} is the viscosity of the gas mixture in Pa.s, T is the temperature in K, LR is the length of the reactor in m, Pin and Pout are the inlet and outlet pressures, respectively in Pa, and r is the radius of the reactor in m.

HP equation is commonly used for calculating pressure differences for an isothermal viscous incompressible flow. So this equation was used to verify the pressure measurements for the isothermal flow at 300 K as shown in Figure 5.

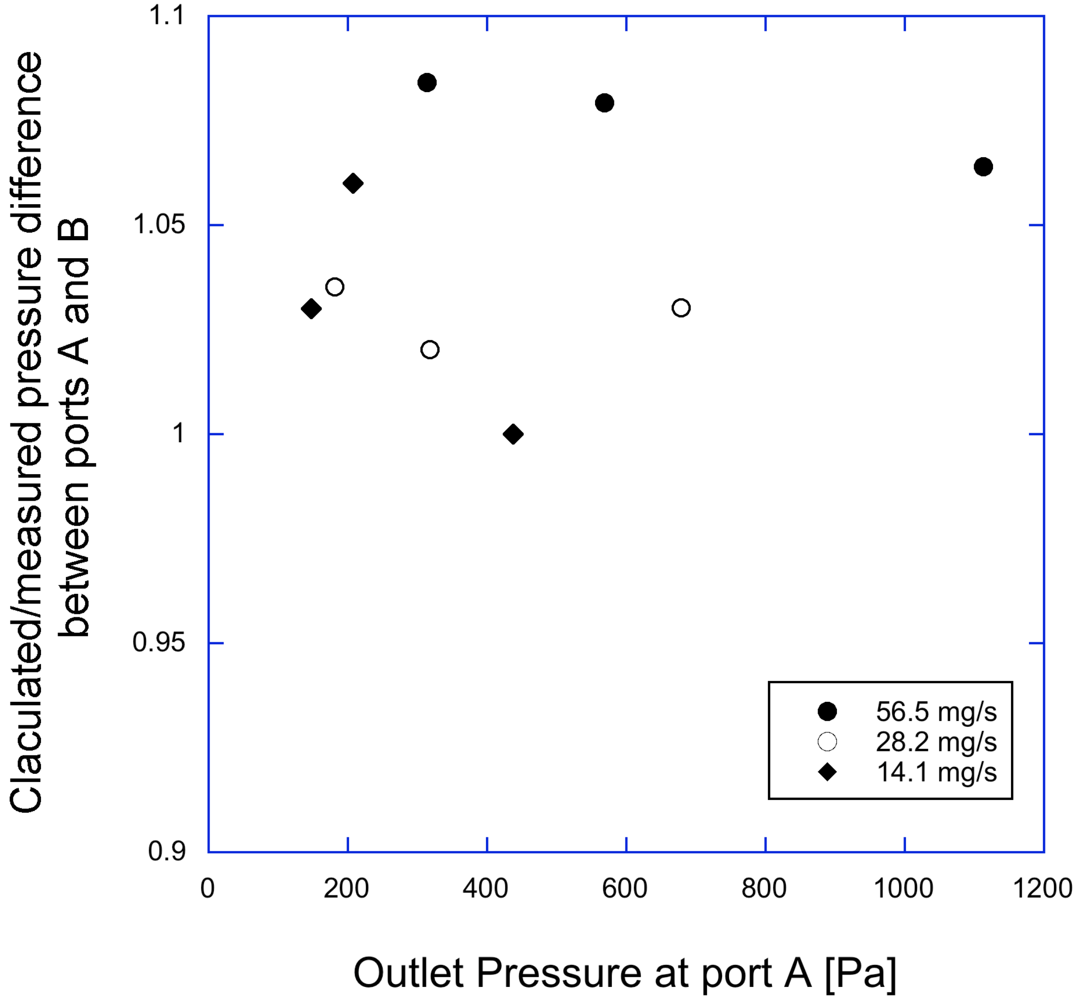

Figure 5: Ratio of calculated (using Hagen-Poiseuille equation) to measured pressure differences between ports A and B for isothermal flow (300 K) of 87% O_2–13% Ar gas mixture at different mass flow rates and outlet pressures through the reactor with the discharge turned *off*.

Validation of the flow component

The model was first solved for flow with no afterglow chemistry for various combinations of flow rates and outlet (port A) pressures. Model inputs include the inlet velocity and outlet pressure for the isothermal case and the inlet pressure is calculated.

Additional inputs, temperature profiles at the entrance and the wall, are required for the non-isothermal case. In both cases a parabolic inlet velocity profile was assumed with the mean velocity calculated using the measured inlet pressure, mean temperature at the inlet, and the flow rate. Four different flow conditions were characterized and are as discussed below.

Case I: Discharge *off*, Furnace *off*

This condition was experimentally characterized by determining the pressure difference between port A and port B for various combinations of mass flow rates and outlet pressures (Experiment RC1 in Appendix C). Computational characterization was performed using the incompressible Navier-Stokes equation (Model I in Appendix B). As seen in Figure 6 the calculated and measured values of pressure differences agree to within 10%.

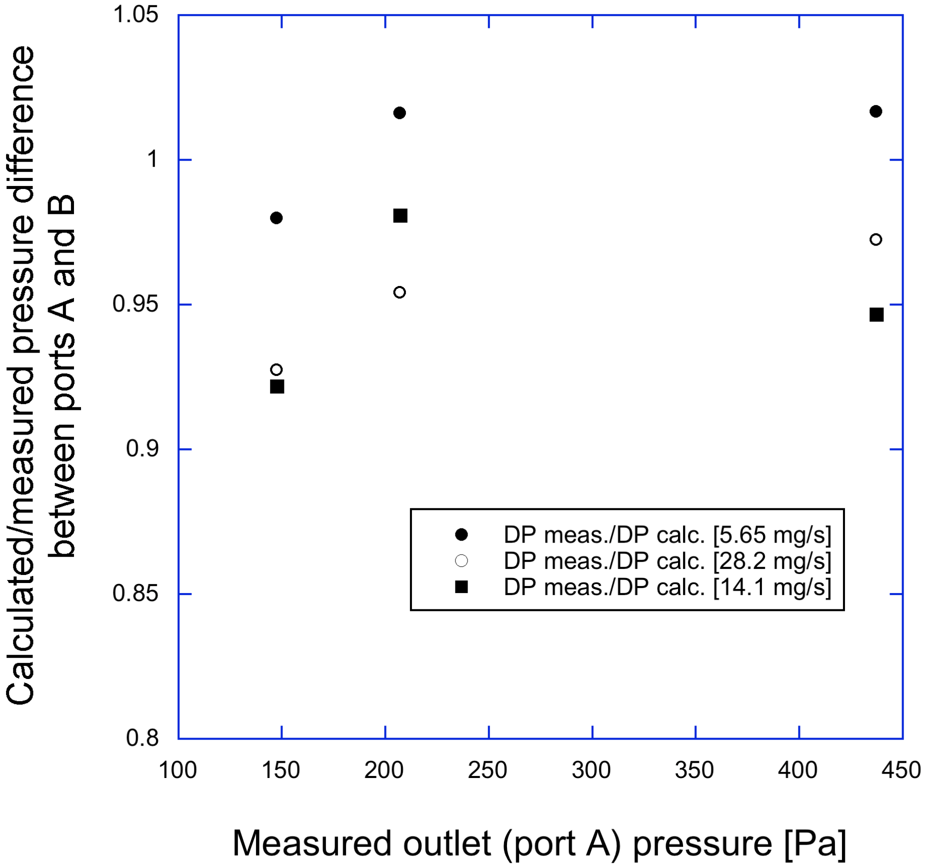

Figure 6: Ratio of calculated/measured pressure differences between ports A and B for isothermal flow (300 K) of 87% O_2–13% Ar gas mixture at different mass flow rates and outlet pressures through the reactor with the discharge turned *off*.

Case II: Discharge *off*, Furnace *on*

This condition was experimentally characterized by measuring the pressure difference between ports A and B for various combinations of flow rates and outlet pressure (Experiment RC2 in Appendix C) with the furnace maintained at 1323 K (1050 °C). The assumed wall temperature profile (used as a boundary condition) and the calculated centerline temperature profile are shown in Figure 7. The furnace consists of 0.35 m of SiC heating elements. The reactor wall surrounded by the heating elements was assumed to be at the furnace temperature. A 0.05 m section of the quartz tube before and after the 35 cm furnace section was insulated. The temperature in these 0.05 m sections was assumed to ramp steeply as shown in Figure 7. The temperature of the wall between the end of the furnace section (including the heating elements and the insulation) and port A was measured to be 380 K, 350 K, and 320 K for flow rates of 2300 sccm, 1100 sccm and 550 sccm, respectively.

Using these assumptions, the calculated pressure differences again agreed to 10 % of the measured as shown in Figure 8. Furthermore, the calculated centerline temperature at port A (outlet) was found to be within 10 % of the measured value. This indicates that the semi-empirical temperature profile at the reactor wall predicts the flow characteristics in the reactor with acceptable uncertainty. There is a possibility that conduction from the furnace could affect the temperature of the gas near the entrance. But, the calculated temperature close to the entrance was found to be independent of the furnace.

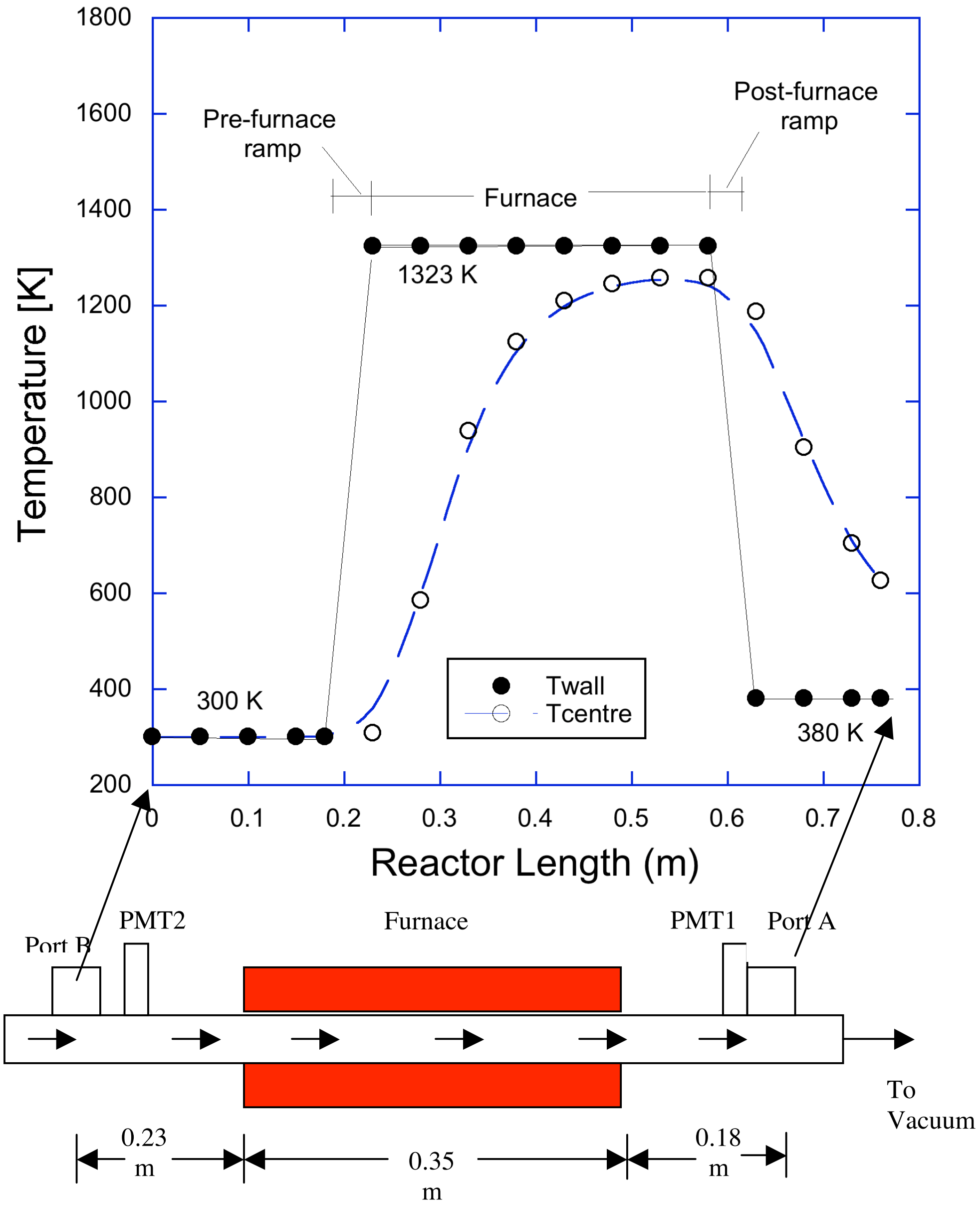

Figure 7: Assumed wall and calculated centerline temperature profiles in the reactor for a flow rate of 2300 sccm of 87% O_2–13% Ar gas mixture, outlet pressure of 431.3 Pa, with the discharge *off*, and the furnace maintained at 1323 K.

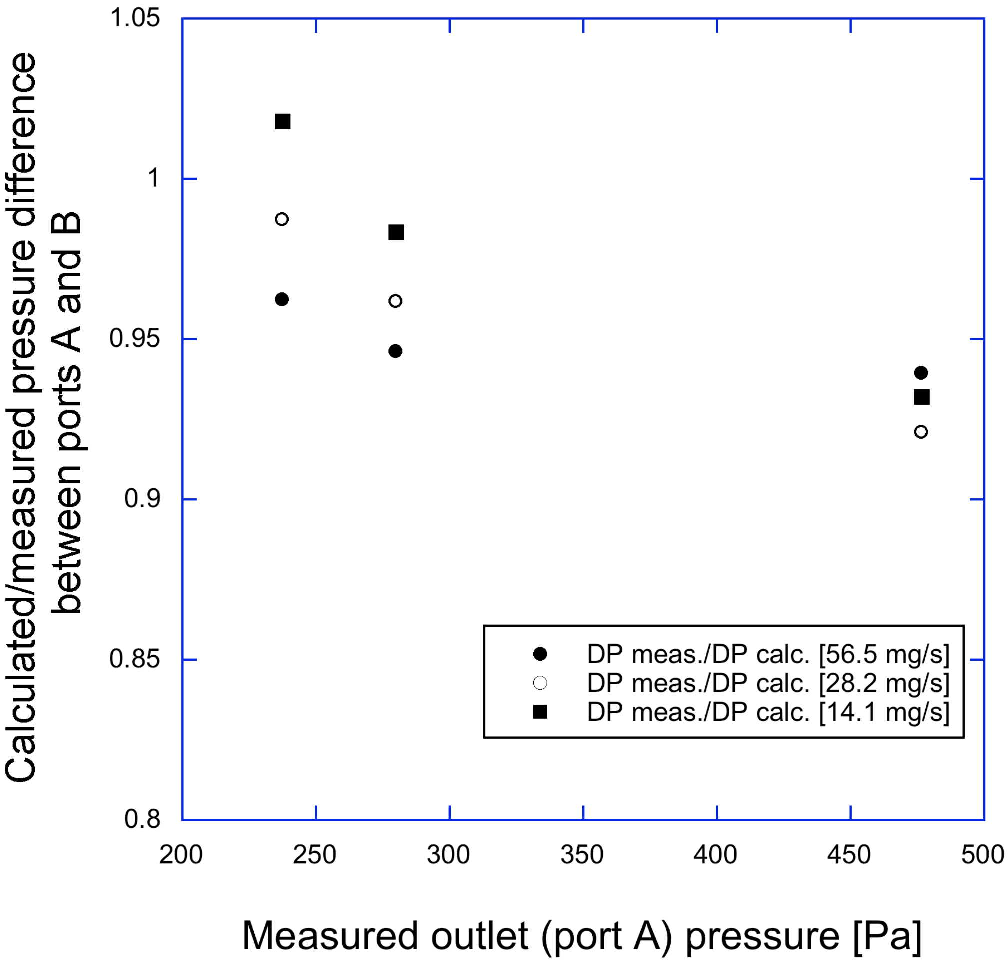

Figure 8: Ratio of calculated/measured pressure differences between ports A and B for non-isothermal flow of 87% O_2 – 13% Ar gas mixture at different mass flow rates through the reactor with furnace maintained at 1323 K with the discharge turned *off*.

Case III: Discharge *on*, Furnace *off*

Pressures at ports A and B were determined for various discharge powers for 2300 sccm of 87% O_2–13% Ar, without turning *on* the furnace (Experiment RC3 in Appendix C). It was observed that although the furnace was not turned *on,* the flow was non-isothermal due to heating of the incoming gas in the microwave discharge. The temperature of the gas measured at PMT2 was dependent on the MWPs as shown in Figure 9. Therefore, to model the system between ports A and B one has to take into consideration both thermal and non-thermal radiative fluxes in addition to the conductive and convective heat fluxes. Validation of such a model requires temperature and radiation measurements in this entrance region. However, the objective of this work is to determine the concentration profiles near the sample and not near the discharge itself. Thus, a detailed study of this entrance region was not carried out and the centerline concentration and temperature measurements were done at PMT2 0.075 m (7.5 cm) downstream of port B. The system between PMT2 and port A was modeled using only the conductive and convective heat fluxes, neglecting any radiative fluxes. Centerline temperature measurements were taken at four axial locations between PMT2 and port A for conditions at which oxidation experiments were carried out, but with the furnace *off*. These data were used to validate the assumption that radiative heat flux was negligible in this region.

The system was modeled between ports A and B to determine the radial temperature profile at PMT2. Radial temperature profiles at PMT2 were calculated by first assuming a linear and then a parabolic radial temperature gradient at port B. The wall temperature was varied between 370 K at port B to 305 K at port A as per experimental data. In both cases the temperature profile at PMT2 was found to be similar as shown in Figure 10. This temperature gradient at PMT2 will be referred to as "the OB gradient" in the following text. When the OB gradient was used at port B instead of the linear or parabolic temperature gradients, the radial temperature gradient at PMT2 was found same as before. Hence for three different entrance temperature gradients at port B, similar temperature profiles at PMT2 were obtained as shown in Figure 10. In addition, the calculated centerline temperatures at four axial locations between PMT2 and port A agreed to within 10 % of the measured values for all the assumed temperature gradients at port B, as shown in Figure 11. Thus, it was concluded that the calculated temperature profile at PMT2 is an acceptable representation of the actual radial temperature profile at PMT2. Also, the velocity profile at PMT2 was calculated to be parabolic. Thus it is reasonable to use a parabolic entrance velocity profile when modeling the system between PMT2 and port A.

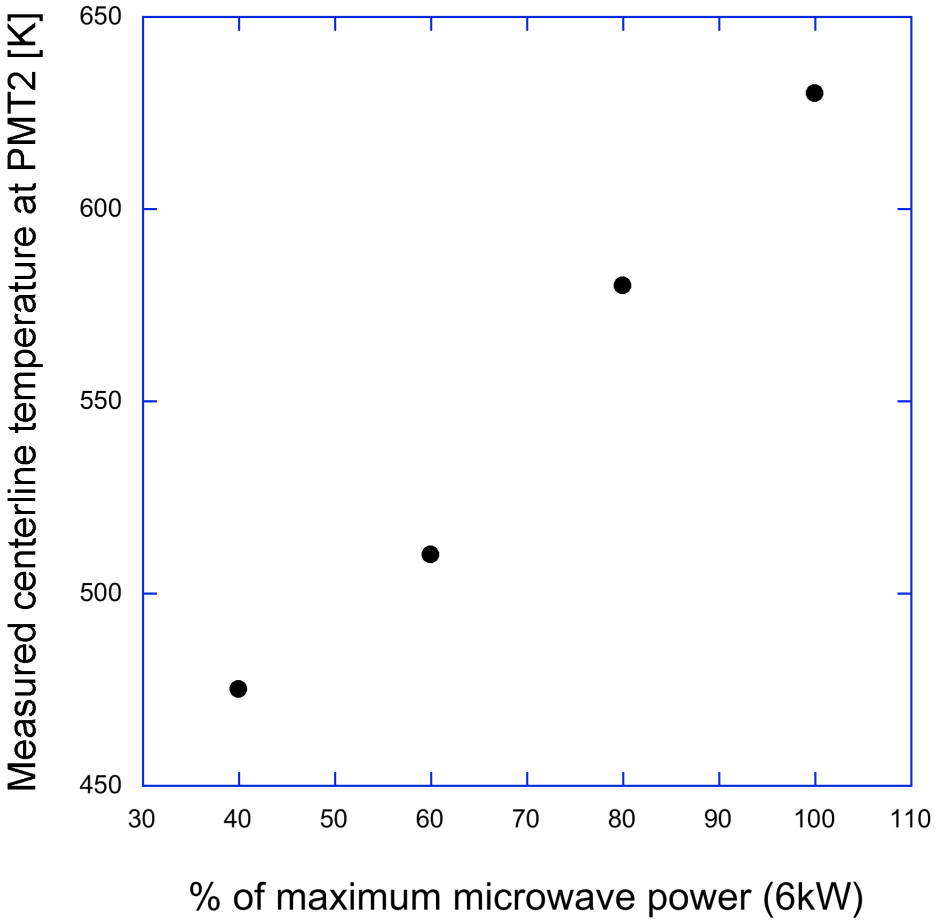

Figure 9: Measured centerline temperature at PMT2 for various microwave powers for a 2300 sccm of 87% O_2-13% Ar gas mixture, at 431.3 Pa outlet pressure, and 80% of full discharge power with the furnace turned *off*.

Having determined the temperature profile and pressure at PMT2, the flow component between PMT2 and port A can be validated. The wall temperature was varied between 345 K at PMT2 and 305 K at port A as per the measurements. The calculated (using Model II in Appendix B) and measured pressure differences were found to be within 10 % of the measured values as shown in Figure 12.

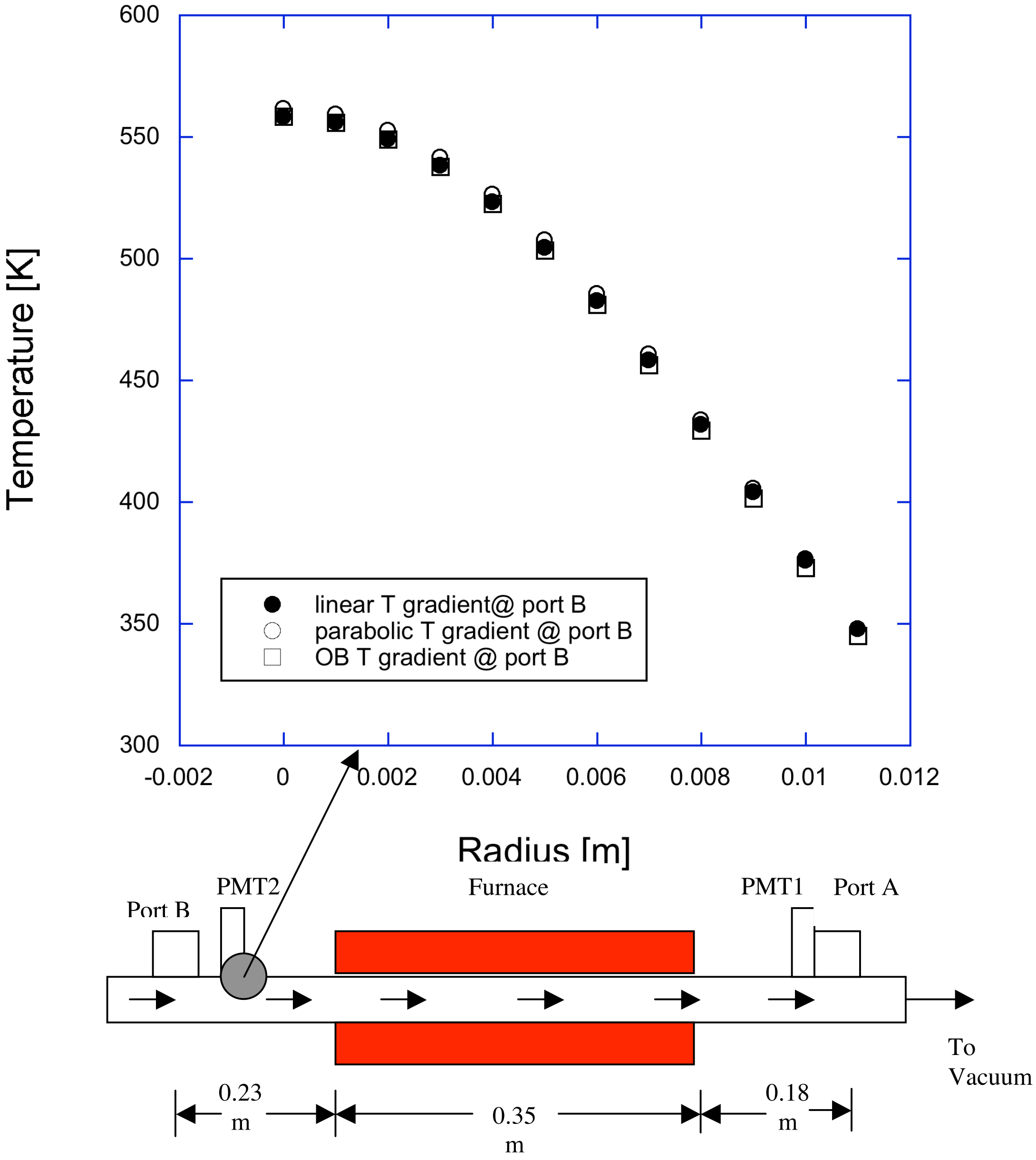

Figure 10: Radial temperature profile at PMT2 for different temperature profiles at port B for a 2300 sccm of 87% O_2-13% Ar gas mixture, at 431.3 Pa outlet pressure, and 80% of full discharge power with the furnace turned *off*.

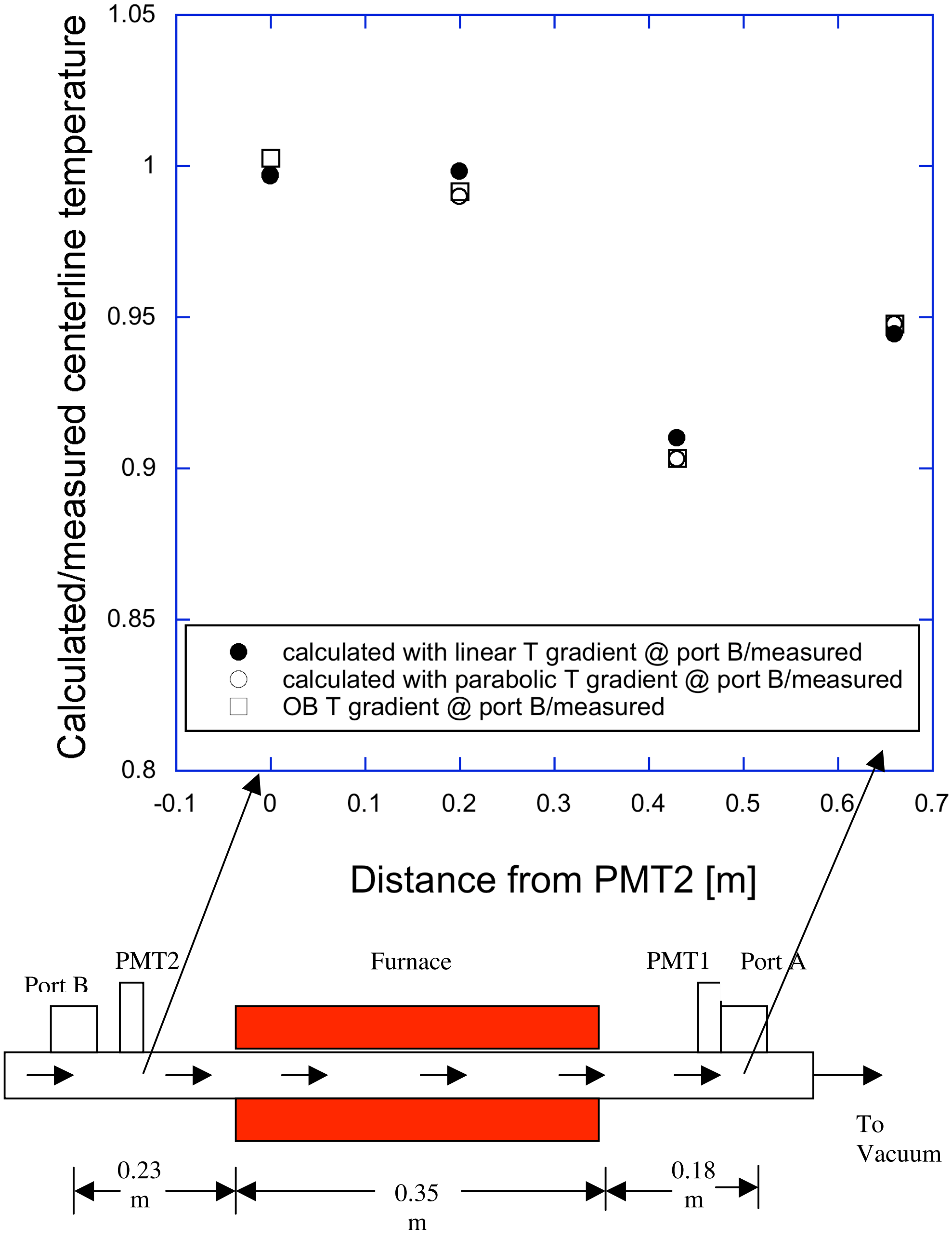

Figure 11: Centerline temperature profile for 80% of full discharge power, 2300 sccm of 87%O_2-13%Ar gas mixture, at 3.2 Torr outlet pressure, and with the furnace turned *off*.

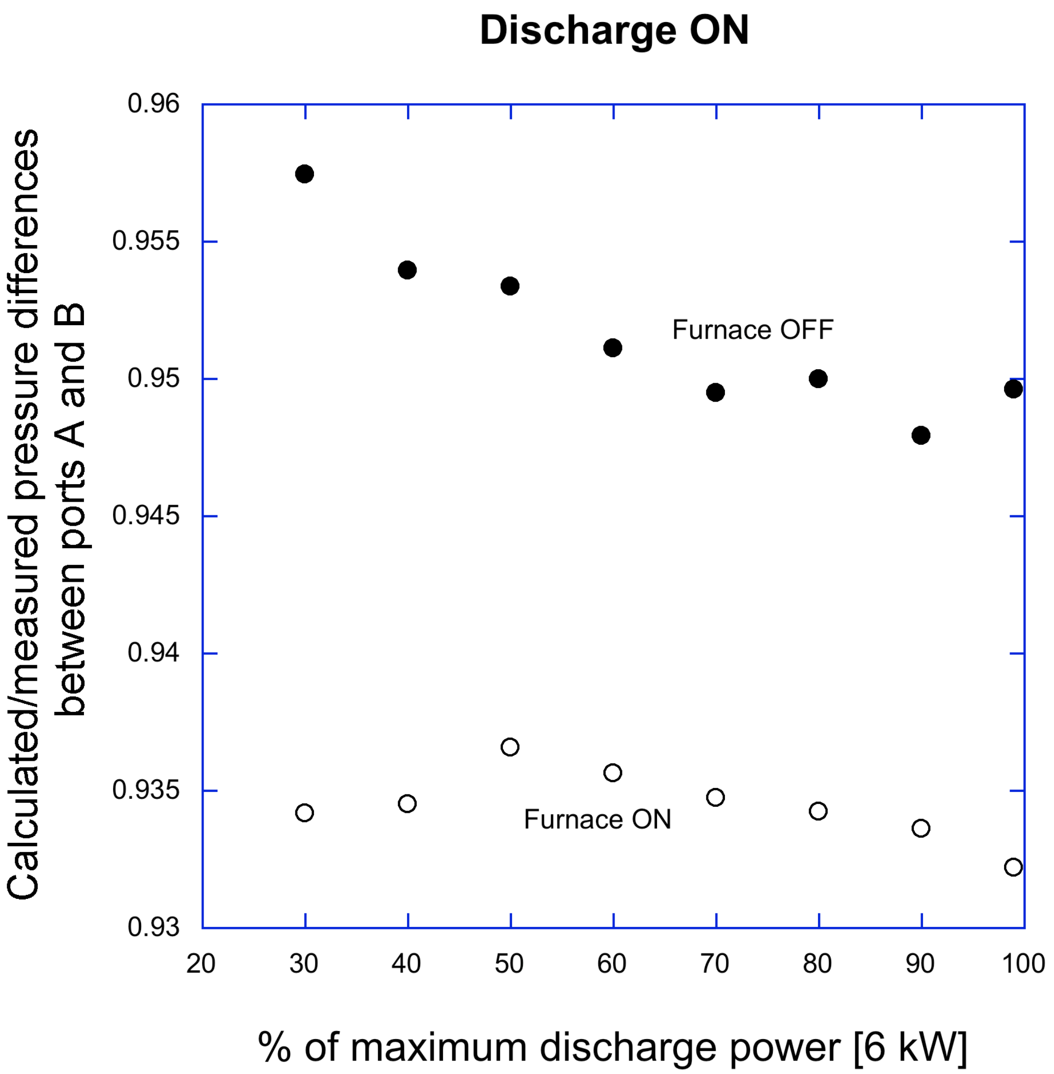

Figure 12: Ratio of calculated/measured pressure difference between port A and PMT2 at different discharge powers, for 2300 sccm of 87% O_2-13% Ar gas mixture, at 431.3 Pa outlet pressure, and with the furnace turned *off* and then maintained at 1323 K.

Case IV: Discharge *on*, Furnace *on*

Pressure differences were measured for various microwave powers and a furnace temperature of 1323 K at a constant flow rate of 2300 sccm of 87% O_2–13% Ar, at an outlet pressure of 431.3 Pa (Experiment RC4 in Appendix C). These conditions are representative of the conditions of the oxidation experiments. From case II (discharge *off*, furnace *on*), it was seen that the furnace temperature did not affect the entrance temperature. Therefore the entrance temperature profile was assumed to be similar to that used in case III (discharge *on*, furnace *off*). The wall temperature profile used is as described in section case II (discharge *off*, furnace *on*). The measured and calculated (using Model III in Appendix B) pressure differences were again found to agree within 10 % as seen in Figure 12. The calculated centerline temperature profile for this case is shown in Figure 13. It was observed that the temperature of the gas heated in the microwave discharge, entering the reactor at PMT2 decreases rapidly.

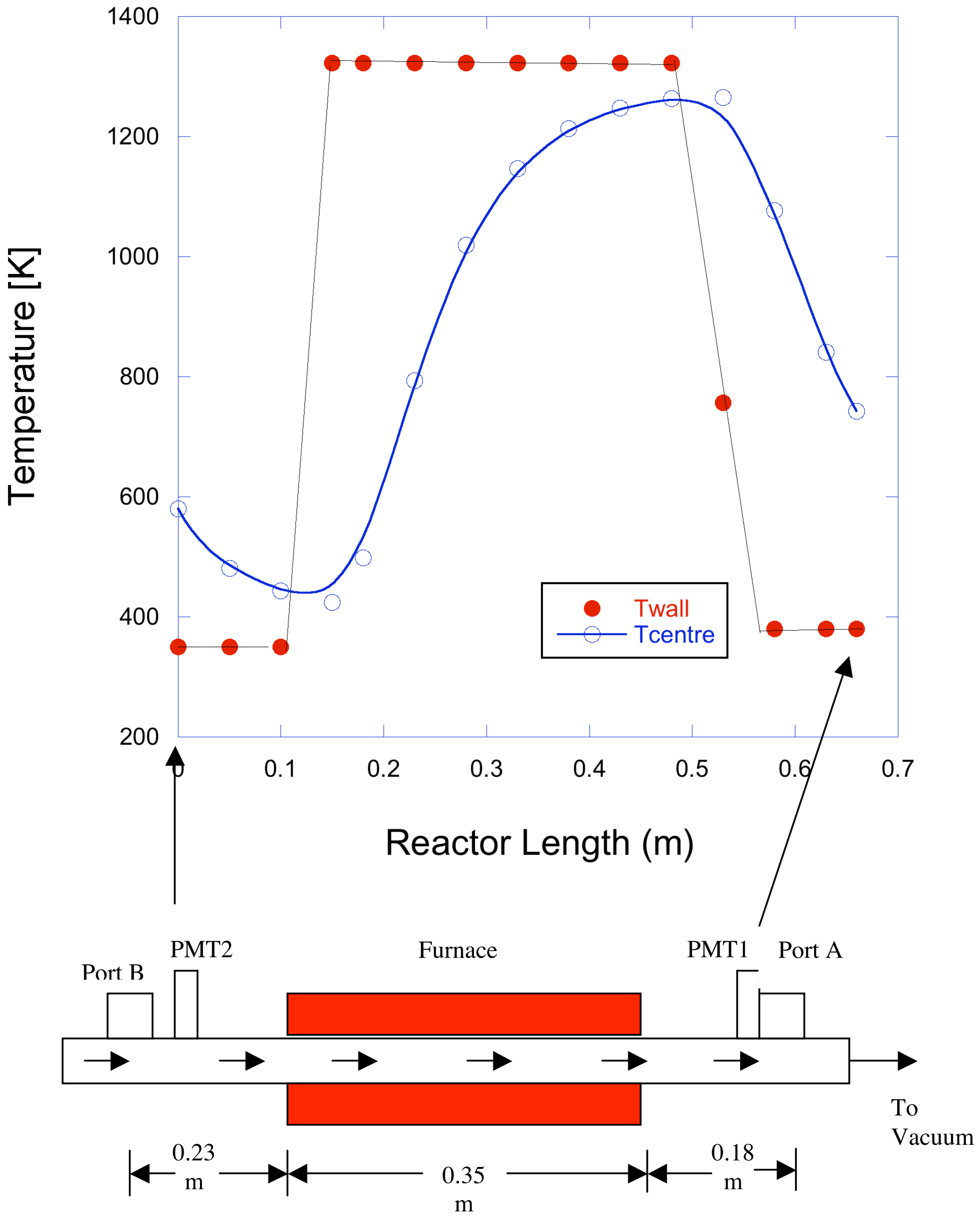

Figure 13: Wall and centerline temperature profiles in the reactor for a flow rate of 2300 sccm of 87%O_2–13%Ar gas mixture, outlet pressure of 431.3 Pa, at 80% microwave discharge power, and the furnace maintained at 1323 K.

Convergence Studies

The discretization error is a significant source of error in finite element method. This error arises due to the representation of the model equations in a discrete domain of space (grid) rather than in a continuum. Grid convergence study is used to determine the discretization error by solving the model at three different grid sizes with a constant grid refinement ratio. A grid convergence index (GCI) [1] is used to provide a consistent method in reporting the results of grid convergence and to determine whether the solutions are in the asymptotic range of convergence. The GCI is the measure of the percentage by which the calculated value differs from the numerical asymptotic value. Conditions of 2300 sccm (of 87% O_2–13% Ar gas mixture), outlet pressure of 277.31 Pa, 80 % microwave discharge power, and with furnace maintained at 1323 K were used for the convergence studies. The inlet pressure measured for these conditions was 503.56 Pa.

The model was solved at three different grid sizes. A grid refinement ratio (rr) of 2 was used for each mesh refinement. A summary of grid sizes used in each direction and the results obtained are as shown in Table 4. The order of convergence (OC) was found to be 2.93 for these conditions. Using this OC and a Richardson extrapolation the solution at zero grid spacing is 495.12 Pa. Thus, the error between the extrapolated value and the measured value is 1.67%. Also the solutions were found to be in the asymptotic range, as the ratio of grid convergence indices after each refinement was $\sim(\mathrm{rr})^{\mathrm{oc}}$, which satisfies the criteria [1] for asymptotic convergence.

Once the flow component has been validated, the oxygen plasma afterglow chemistry was added to the model since the main focus of this characterization effort is to determine the amount of O atoms lost through homogenous and heterogeneous recombination at different flow conditions.

Table 5: Calculated inlet pressure at different mesh sizes

	No. of elements			**Calculated inlet pressure (Pa)**
	r direction	*z* direction	Total	
P1	1	16	16	486.04
P2	2	32	64	493.92
P3	4	64	256	494.96

Validation of chemistry

Validation of chemistry was carried out with the furnace *off* and then with furnace *on*. Calculated and measured O atom concentrations were compared to determine the O atom recombination mechanism that can minimize the difference between them, both in the low and high temperature regimes.

Validation at low temperature

The ratio of the centerline outlet to inlet O atom concentrations were measured using the calibration procedure described in Chapter III for conditions of 2300 sccm of 87% O_2–13% Ar gas mixture, outlet pressure of 293.3 Pa, with the furnace *off*, and at various MWP. The outlet O atom concentrations were calculated by adding chemistry to the model (between PMT2 and port A) described in case III (Discharge *on*, Furnace *off* - Model II in Appendix B). The additional model inputs needed are the concentration of various species at the entrance. The entrance concentration profile was assumed to be function of temperature as described in Chapter IV. The heterogeneous recombination was taken into account by using a reactive boundary condition at the wall with γ set at 1×10^{-4} as reported in the literature [2]. The rate constants used for the gas phase recombination are as shown in Table 4. The ratio of the calculated centerline O atom concentration at the outlet to the measured centerline O atom concentration at the inlet (an input to the model) was then compared to the measured values resulting from a range of MWPs. As seen in Figure 14, there is a significant discrepancy between the measured and calculated ratios. Possible sources of this discrepancy are the governing equations, the rate constants used, and the calibration procedure for determining the O atom concentrations at the outlet. However, the same governing equations were successfully used to define the flow in the reactor system. Since, the chemistry is significantly affected by the flow, there won't be any significant error introduced due to the governing equations.

The calculated ratios, as shown in Figure 14, were found to be greater than 1 in most case, suggesting that there are more O atoms at the outlet than at the inlet. The outlet being at lower temperature than the inlet will have higher density of O atoms if the recombination chemistry is not the dominant factor affecting the O atom concentrations. Therefore, the model suggests that O atom concentrations are mainly dependent on the flow conditions at the two ports and not the recombination chemistry between the ports for the rate constants used. This could also mean that there is an error in the rate constants used. As shown in Table 4, there is a significant uncertainty in the rate constants reported in the literature. But as seen in Figure 14, the rate constants required for the calculated values to match the calculated values are significantly higher than that reported in the literature even after considering the uncertainty in them. For example, γ needs to be 3×10^{-3}, rather than 1×10^{-4} (other rate constants being held constant) for the calculated values to match the measured values. This is more than an order of magnitude increase in γ. Similar analysis was carried out varying the rate constant $K2_{Ar}$ for the reaction $O + O_2 + M \rightarrow O_3 + M$. This reaction was chosen as it is the dominant gas-phase reaction for systems with excess O_2 [3] as is the case in our system. As shown in Figure 14, $K2_{Ar}$ needs to be increased by a factor of 50 for the calculated values to match the measured values. Thus one can eliminate the rate constants used as the sole source of error.

Another possible source of error is the way centerline O atom concentrations at the outlet are measured. The procedure as described in Chapter III is based on determining the absolute centerline O atom density at the inlet and then calibrating the system to determine the ratio of centerline O atom concentration at the outlet to the inlet. There was significant difference between the temperature at the inlet and outlet (~ 200 K) when the experiment was carried out at 80% MWP and with the furnace *off*, but the Xe calibration was done at isothermal and isobaric conditions. The calibration procedure equations do take into account this temperature and pressure difference between the outlet and inlet. The outlet concentrations are then derived from this ratio. There is a possibility that the source of error might be in the equations, which the calibration procedure uses to take into account the change in temperature. To verify this a series of control experiments were run at isothermal conditions as described below.

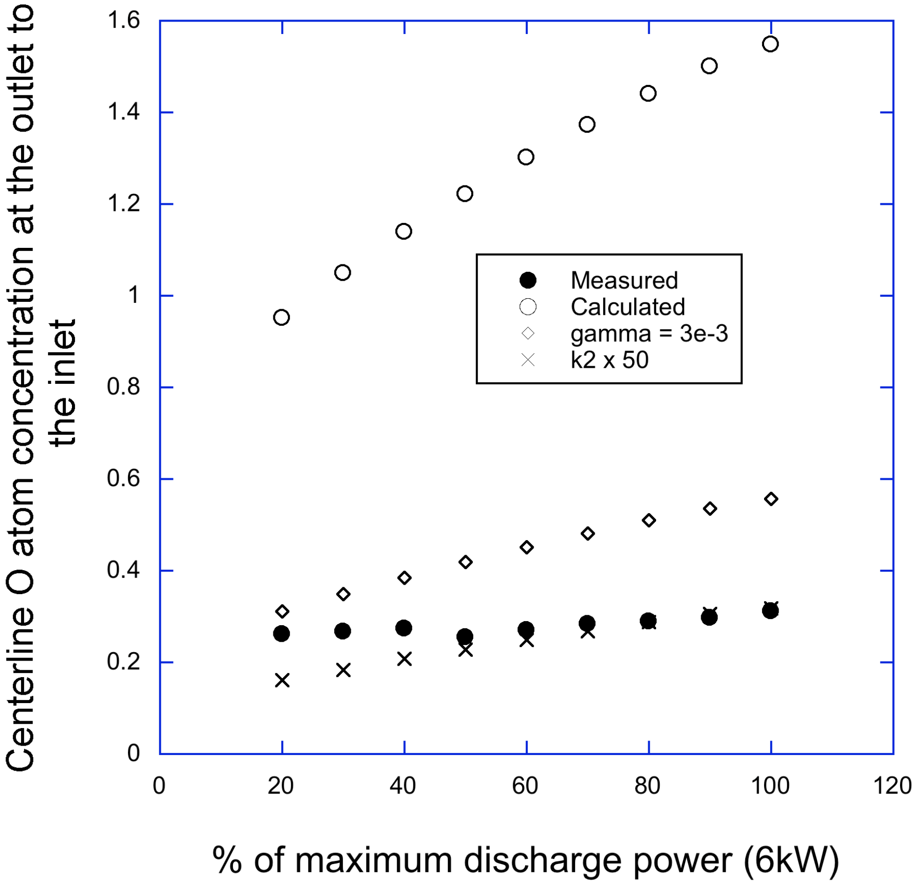

Figure 14: Comparison of measured and calculated ratios of centerline O atom concentrations at the outlet to that of the inlet at various MWPs at a mass flow rate of 2300 sccm (87% O_2-13% Ar gas mixture) and an outlet pressure of 293.3 Pa.

Control experiments at isothermal conditions

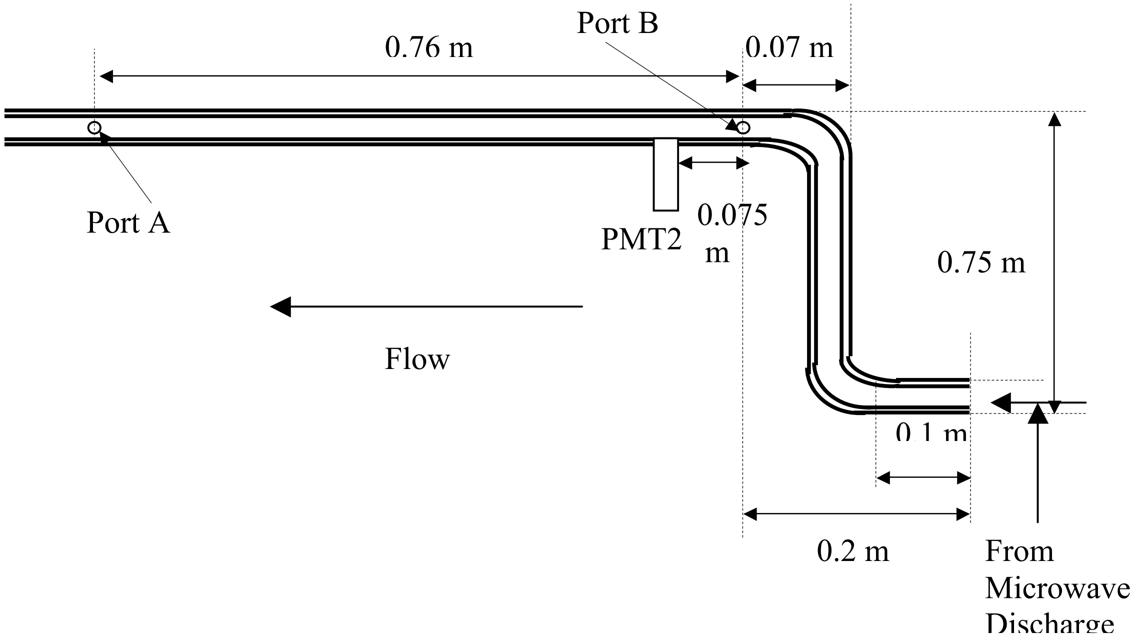

Figure 15: Experimental set-up for the control experiments.

As shown in Figure 13, the temperature of the gas at the entrance cools down from 600 K to ~ 400 K in the first 10 cms of the flow tube. So a bend in the tube was added between the microwave discharge and the entrance to the reactor to serve two purposes. First, it adds to the distance that the gas has to travel before it reaches port B, thus giving it more time to cool down. The temperature both at ports B and A was measured to be 300 K. Secondly, it eliminates any contributions of UV radiation from the discharge on O atom dissociation.

Using the above set-up, experiments were run at 80% MWP, 300 K, and at pressures and flow rates as shown in Table 6. Absolute centerline O atom concentration was measured at PMT2. The ratios of centerline O atom concentration to that at PMT2 were determined for three other axial locations using the calibration procedure described in

Chapter III. The ratio of centerline O atom concentrations at the outlet to the inlet measured for this experimental configuration were higher than that measured for the standard experimental conditions (non-isothermal conditions). This is counter-intuitive, as more recombination of O atoms should take place at lower temperature (lower velocity and higher O atom concentration) prevailing in the control experiments. This is an indication of an error in the calibration procedure for the non-isothermal case. Corresponding O atom concentration ratios were calculated by adding chemistry to the model described in case I (Model I in Appendix B). The heterogeneous recombination was taken into account by a reactive boundary condition at the wall using a γ of 1×10^{-4} as reported in the literature [2]. The rate constants used for the gas phase recombination are as shown in Table 4. The ratios of calculated to measured centerline O atom concentrations at various axial locations for different process conditions are shown in Figure 16. The calculated values were always greater than the measured values, even after eliminating the temperature difference between the inlet and the outlet. Thus, temperature doesn't seem to be the sole source of error for the non-isothermal case.

The calculated values were significantly different than the measured values even when the flow was neglected as shown in Table 7, i.e. when the system of coupled ordinary differential equations representing the consumption/generation of various species were solved separately as if the gas mixture was contained in a batch reactor. This means that the governing flow equations are not a source of error at isothermal conditions.

Another possible source of error at these isothermal conditions can be the rate constants used to represent the chemistry in the model. To check if this was the case, the model was solved for different conditions (C1-C5) by varying each rate constant individually for each process condition. Such an analysis was also done for the non-isothermal case as shown in Figure 14. As seen in Table 4, the rate constants are functions of temperature alone in the pressure range considered. And this being an isothermal flow, the idea was to vary rate constants individually to find one value of rate constant under consideration that eliminates the discrepancy for all the five conditions described in Table 6.

Such an analysis was first carried out on the surface recombination coefficient, γ. As shown in Table 7, no one value of γ could eliminate the discrepancies in all the control experiments. In addition, the value of γ required for C1 and C3 were a lot higher than that reported in the literature [2]. Similar analysis was done by varying rate constant K2 for the gas-phase reaction $O + O_2 + M \rightarrow O_3 + M$ as it has the most significant effect on the O atom chemistry in systems having excess O_2 [3]. Again, no one value of $K2_{Ar}$ could eleminate the discrepancies for all the control experiments.

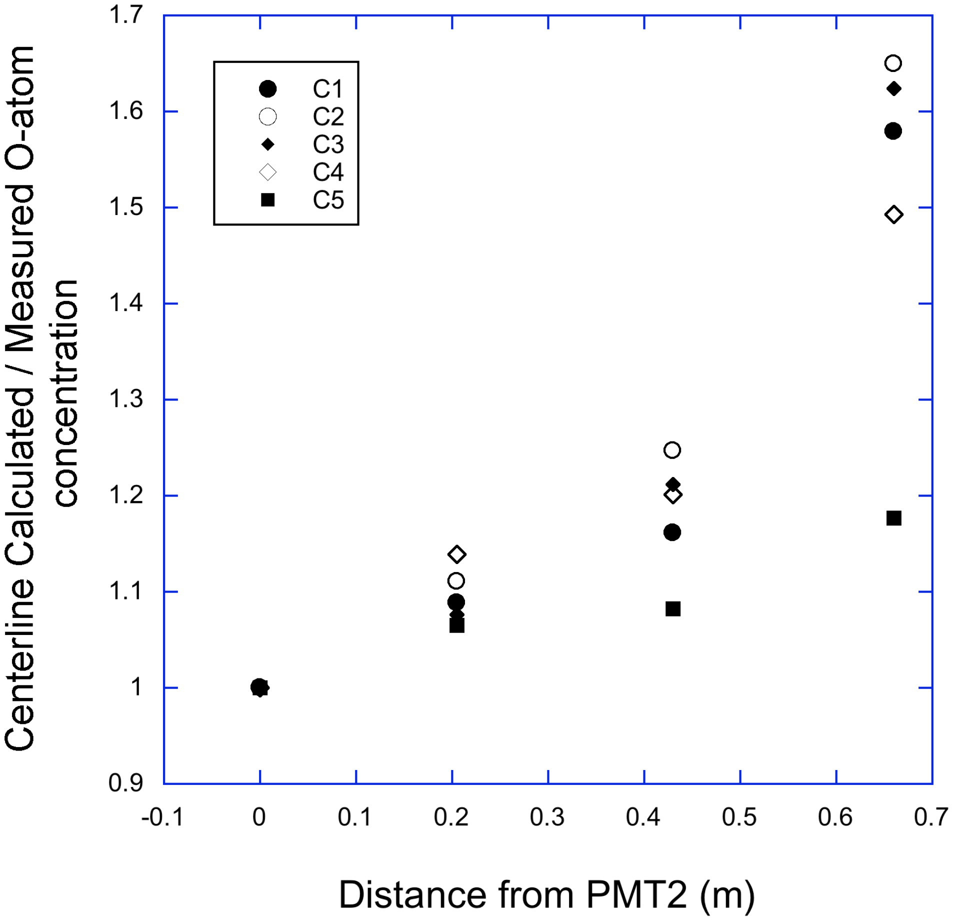

Figure 16: Ratio of calculated/measured centerline O-atom concentration at various axial positions for an isothermal flow at 300 K, 80% MWP, and at a flow rate of 2300 sccm (87% O_2-13% Ar gas mixture) and 466.6 Pa outlet pressure (C1), at a flow rate of 2300 sccm (87% O_2-13% Ar gas mixture) and 346.6 Pa outlet pressure (C2), at a flow rate of 767 sccm (87% O_2-13% Ar gas mixture) and 173.3 Pa outlet pressure (C3), at a flow rate of 767 sccm (87% O_2-13% Ar gas mixture) and 346.6 Pa outlet pressure (C4), at a flow rate of 767 sccm (87% O_2-13% Ar gas mixture) and 466.6 Pa outlet pressure (C5).

Table 6: Outlet Pressures and flow rates for control experiments run at 80% MWP and 300 K.

Experiment #	Outlet Pressure (Pa)	% of maximum flow rate (2300 sccm of 87% O_2 – 13% Ar)	Mean entrance velocity - u_m (m/s)
C1	466.63	100	23.8
C2	346.6	100	32.3
C3	173.3	33	21.3
C4	346.6	33	11.7
C5	466.63	33	8.29

Table 7: Ratio of centerline O-atom concentrations at an axial location (z) 0.66 m away from PMT2 (z = 0) to that at PMT2 for control experiments C1 and C2.

Experiment #	Measured (c_o@z=0.66 m/ c_o@z=0m)	Calculated (c_o@z=0.66m/ c_o@z=0m) with flow equations	Calculated (c_o@z=0.66m/ c_o@z=0m) without flow equations
C1	0.46	0.73	0.65
C2	0.53	0.88	0.84

Table 8: Values of γ required for the measured values to match the calculated values of concentration ratios for all the control experiments.

Experiment #	Outlet Pressure (Pa)	% of maximum flow rate (2300 sccm of 87% O_2 – 13% Ar)	γ required to eliminate the discrepancy	(j×K2) required to eliminate the discrepancy (j)
C1	466.63	100	7×10^{-4}	2
C2	346.6	100	1×10^{-4}	5
C3	173.3	33	7×10^{-4}	15
C4	346.6	33	3×10^{-4}	2
C5	466.63	33	1×10^{-4}	1

Table 9: Various empirical loss terms used to explain the error in the measurements carried out during the control experiments

Experiment #	**Empirical loss = -** $C/(p\times c_o)$, **C (Torr/s) =**	**Empirical loss = -** $C\times u_m/(p\times c_o)$ **C (Torr/m) =**	**Empirical loss = -** $C\times u_m\times p\times c_o$ **C (1/m/Torr) =**
C1	62.55	2.48	0.22
C2	64.92	1.9	0.29
C3	19.43	0.96	0.56
C4	16.46	1.3	0.2
C5	10.87	1.29	0.1

So in summary, the calculated O atom concentrations at the outlet were compared with the measured values for both non-isothermal and non-isothermal case. Significant discrepancies were seen between the calculated and measured values for the non-isothermal case. Governing equations and the rate constants used for the recombination chemistry in the model were eliminated as the significant source of error. To determine the effect of non-isothermal conditions on the calibration procedure, control experiments were run at isothermal conditions. Calculated outlet O atom concentrations were found to be significantly different from the measured values even at controlled conditions. Again, the governing equations and the rate constants were eliminated as the significant source of error for the isothermal case. An indication of error was found in the calibration procedure, when the measured ratios of O atom concentration at the outlet to the inlet were found higher for isothermal case (300 K) than that measured for non-isothermal case (inlet at 580 K and outlet at 300 K). Lower temperatures of the isothermal case should result in higher recombination of O atoms due to lower velocities (higher residence times) and higher densities. Thus the measured ratios of O atom concentrations at the outlet to the inlet should have been higher for non-isothermal case, which is not the case. Thus, a conclusion was reached that there is an error in the method of measuring the outlet concentration. So the O atom concentration near the sample at oxidation conditions was calculated by inputting the measured O atom concentration at the inlet into the model, whose flow had been validated. This calculated O atom concentration near the sample was then used as an input to the oxidation model.

Validation at high temperature

Significant discrepancies were seen between the measured and calculated O atom concentration also with the furnace *on* as shown in Figure 17. Hence a sensitivity analysis at oxidation conditions to minimize the uncertainty in the chemistry at high temperatures could not be performed. The O atom concentrations near the sample at oxidation conditions (to be put into the oxidation model) were thus calculated using the suggested rates in the literature (Table 4) and the measured absolute O atom concentrations at the inlet as input to the model as described below.

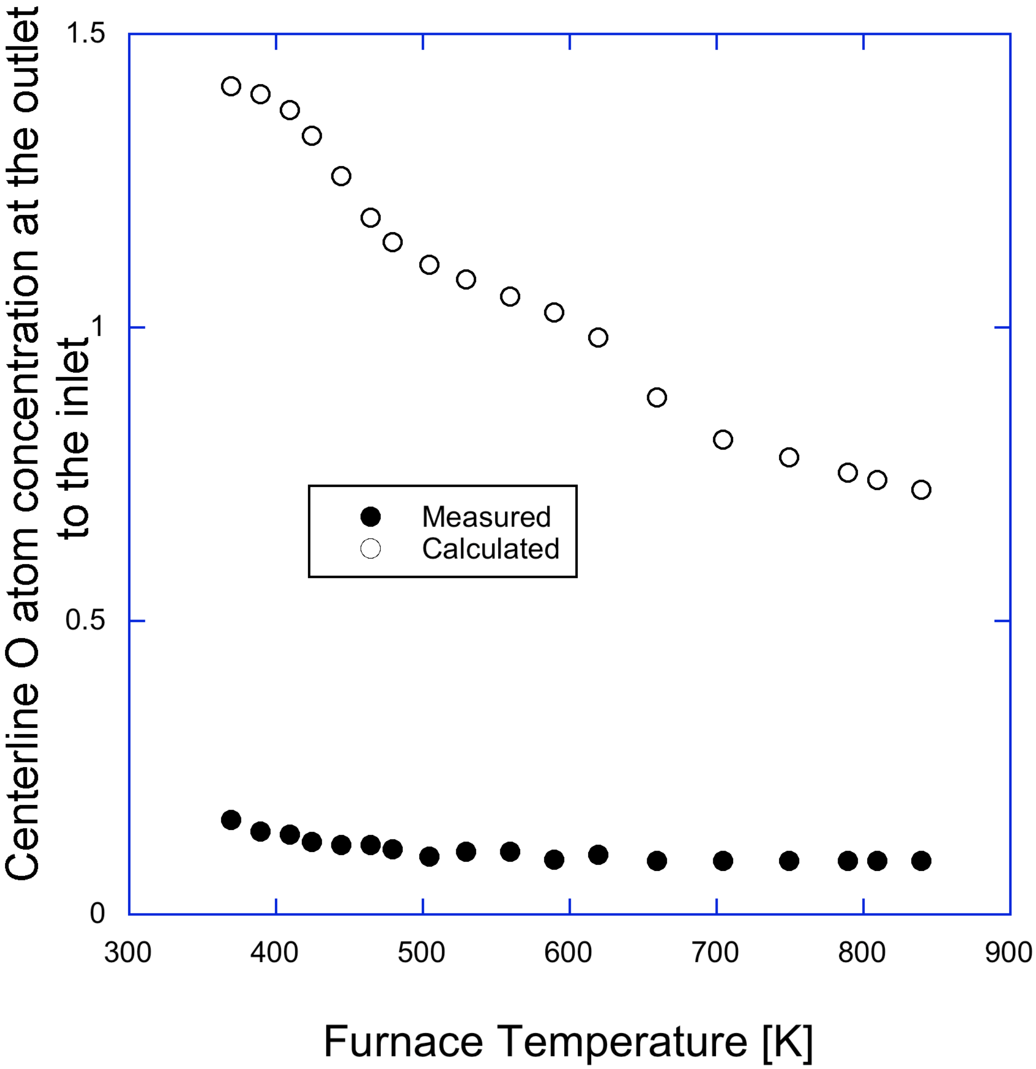

Figure 17: Comparison of measured and calculated ratios of centerline O atom concentrations at the outlet to that of the inlet at a mass flow rate of 2300 sccm (87% O_2-13% Ar gas mixture) 80% MWP, at an outlet pressure of 431.3 Pa

Oxidation conditions

The oxidation experiments were performed using furnace temperatures of 1183 K and 1323 K and outlet pressure of 3.2 Torr. At these conditions, the gas mixture enters the microwave discharge at room temperature, is heated in the microwave discharge, rapidly cools downstream of the discharge, and then is heated in the furnace section of the reactor. It is necessary to understand the effect of these temperature changes on the average O atom concentration near the sample (0.3 m–0.4 m downstream from PMT) and on the concentration gradient in the radial direction. Therefore the model was solved at oxidation conditions and the calculated concentration profile is compared with that calculated with the furnace *off*.

The model was used to calculate the O atom concentration profile in the reactor at a flow rate of 2300 sccm (of 87% O_2–13% Ar gas mixture), outlet pressures of 431.3 Pa, and at 80% MWP. These conditions are representative of the oxidation experiments, but with the furnace *off*. The calculations were carried out by adding chemistry to the model described in case III (discharge *on*, furnace *off* - Model II in Appendix B).

The centerline O atom concentration profile calculated is shown in Figure 18. It was found to initially increase, and then decreased with distance. This is because the centerline temperature in the reactor equilibrates rapidly as shown in Figure 10. This decrease in temperature increases the residence time of O atoms in the reactor and hence more O atoms recombine in the gas phase.

Effect of furnace temperature

The reactor was then modeled at oxidation conditions. The calculations were carried out by adding chemistry to the model described in case IV (discharge *on*, furnace *off*) of flow validation (Model III in Appendix B). The total concentration at the entrance was calculated using the entrance temperature profile (as in case III of flow validation – discharge *on*, furnace *off*). The inlet pressure in this case was different than that for case III as the higher temperatures in the reactor results in higher pressure differences. The concentration at the entrance had to be corrected for this change in inlet pressure when the furnace was turned *on*. The surface recombination coefficient γ was assumed to be 10^{-4} between 200 K - 400 K, 5×10^{-4} in the 400 K - 700 K range, and 10^{-3} above 700 K based on the available data in the literature [2,4-9].

The centerline concentration of O atoms near the sample (0.3 m – 0.4 m from PMT) was found to decrease with increasing furnace temperature as shown in Figure 18. Furthermore, the calculated O atom concentration near the sample is lower than at the inlet, unlike when the furnace is *off*. This is despite the fact that O atom concentration at the inlet is higher with the furnace *on*, due to higher inlet pressures. This holds even when recombination of O atom in the gas phase and on the walls of the reactor was neglected in the model. Since, the temperature near the sample (~1323 K) is higher than at the inlet (~600 K), the O atom density near the sample will be lower than at the inlet in case of insignificant recombination of O atoms. Thus the model suggests that O atom concentration near the sample is dependent more on the process parameters rather than the recombination chemistry for the oxidation conditions.

To determine the average O atom concentration near the sample, a radial average was taken at 0.3 m and 0.4 m and then a value obtained by averaging those two averages. The calculated O atom concentration near the sample had an insignificant radial gradient at these axial locations as shown in Figure 19. Furthermore, no significant difference exists between the radially averaged concentrations at the two axial locations. Thus, the calculated O atom concentration in the region of the furnace where the sample is placed during the oxidation experiments is uniform.

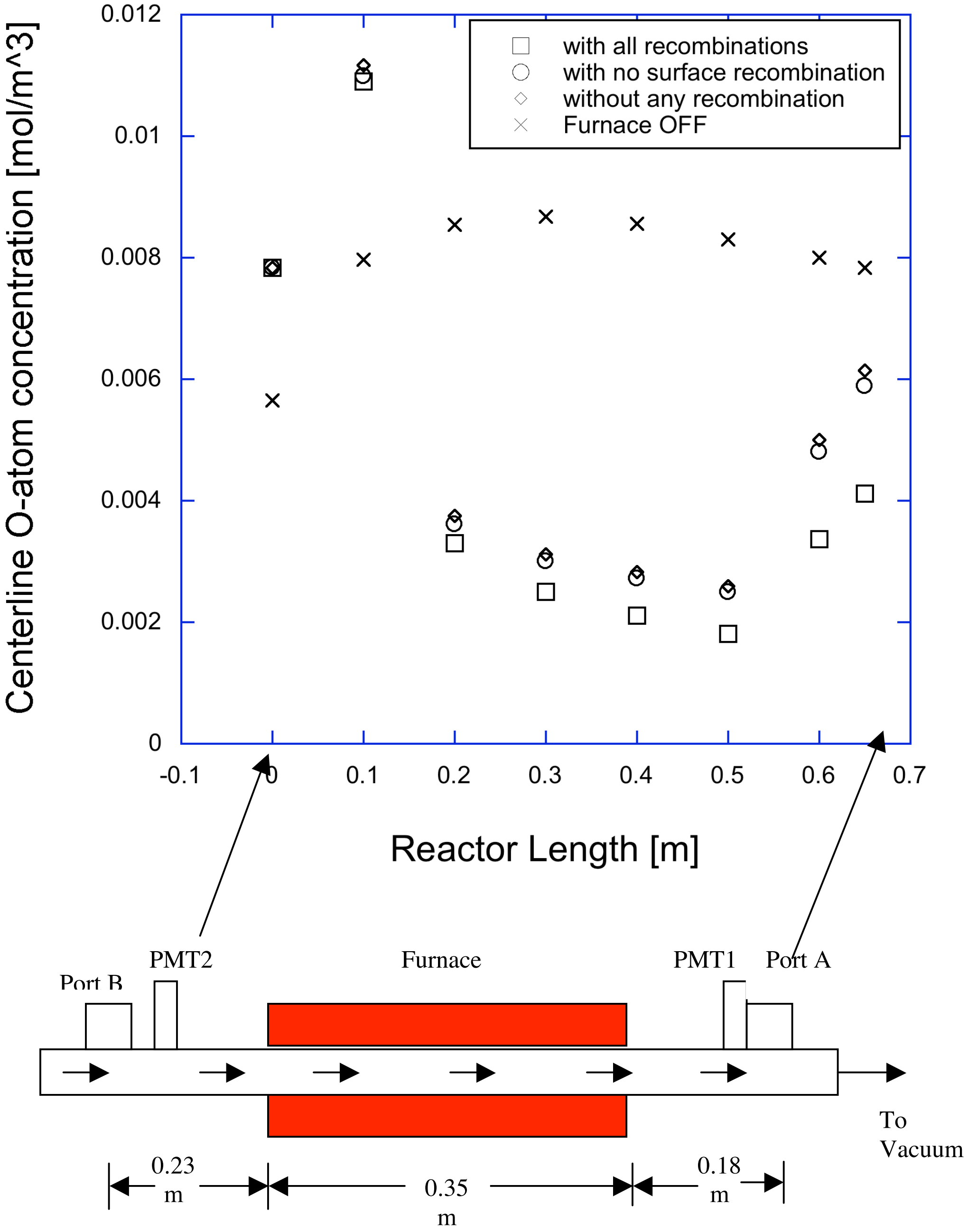

Figure 18: Comparison of the centerline O atom concentrations for a furnace temperature of 1323 K with that for furnace turned *off*, for a flow rate of 2300 sccm (of 87% O_2–13% Ar gas mixture), 431.3 Pa outlet pressure, and 80% MWP

Effect of diffusion

Axial diffusion was found to have no effect on the calculated O atom concentration profile. Furthermore, the concentration of O atoms near the sample (0.3 m–0.4 m from PMT) was nearly constant in the radial direction for a low pressure of 431.3 Pa. Furthermore, when the radial diffusion was neglected in the model, a variation in concentration was seen in the radial direction due to the combined effect of the parabolic velocity profile and radial gradient in temperature. Negligible O atom concentration was seen near the wall due to surface recombination and higher gas phase recombination (due to lower velocities) as one approaches the wall. So at the oxidation conditions, the radial diffusion of O atoms is fast enough to negate any concentration variation in the radial direction, caused due to recombination at the wall and the parabolic velocity profile. This explains the uniform concentration near the sample.

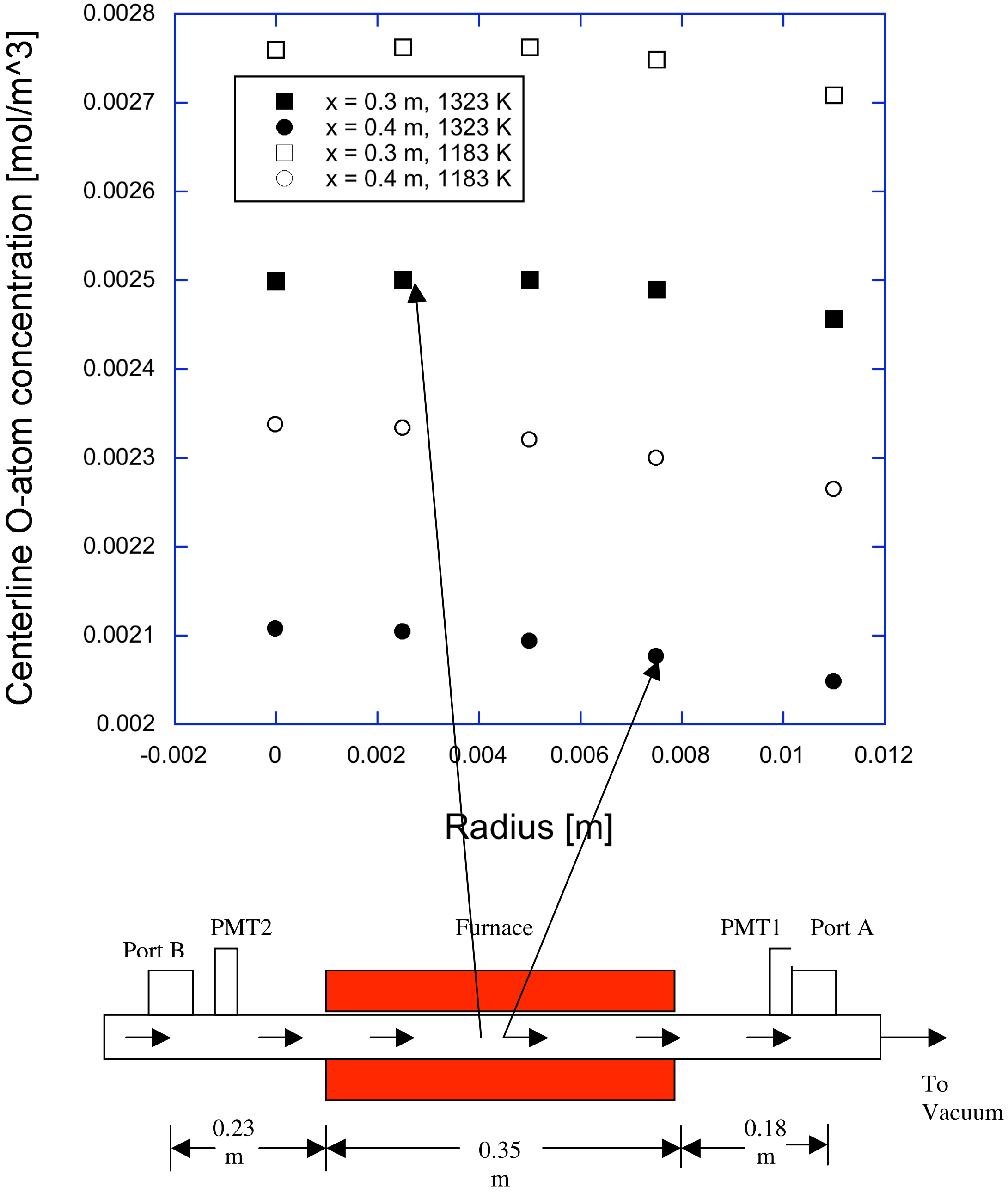

Figure 19: Radial O atom concentration profiles at axial locations of 0.3m and 0.4m downstream of the PMT2 for furnace temperatures of 1323 k and 1183 K at a flow rate of 2300 sccm (of 87% O_2–13% Ar gas mixture), 431.3 Pa outlet pressure, and 80% MWP

Effect of microwave power on O atom concentration

To isolate the quantitative effect of O atoms on the oxidation (of the sample) from the combined effect of O atoms and O_2, O atom concentrations were measured at the inlet for various MWPs. The model was solved for a flow of 2300 sccm (of 87% O_2–13% Ar gas mixture), outlet pressures of 431.3 Pa, furnace temperature of 1323 K, and at 30 %, 50 %, and 100 % MWP as oxidation experiments were carried out at these conditions. It was found that there was a significant increase in the O atom concentration (as observed from the measured value at the inlet and calculated value near the sample) with the microwave power, whereas there was an insignificant decrease in O_2 concentration as shown in Figure 20. This is because O_2 constitutes 87% of the gas mixture and the O_2 dissociation fraction at the highest microwave power (6 kW) was experimentally found to be ~ 0.05 at the reactor inlet. Thus any change in the oxide thickness or structure of the sample, as a function of MWP will be solely due to change in O atom concentration and not O_2. This will be discussed in more detail in the following chapter. The average O atom concentration calculated for the oxidation conditions will be tabulated in the following chapter while discussing the results from the oxidation modeling.

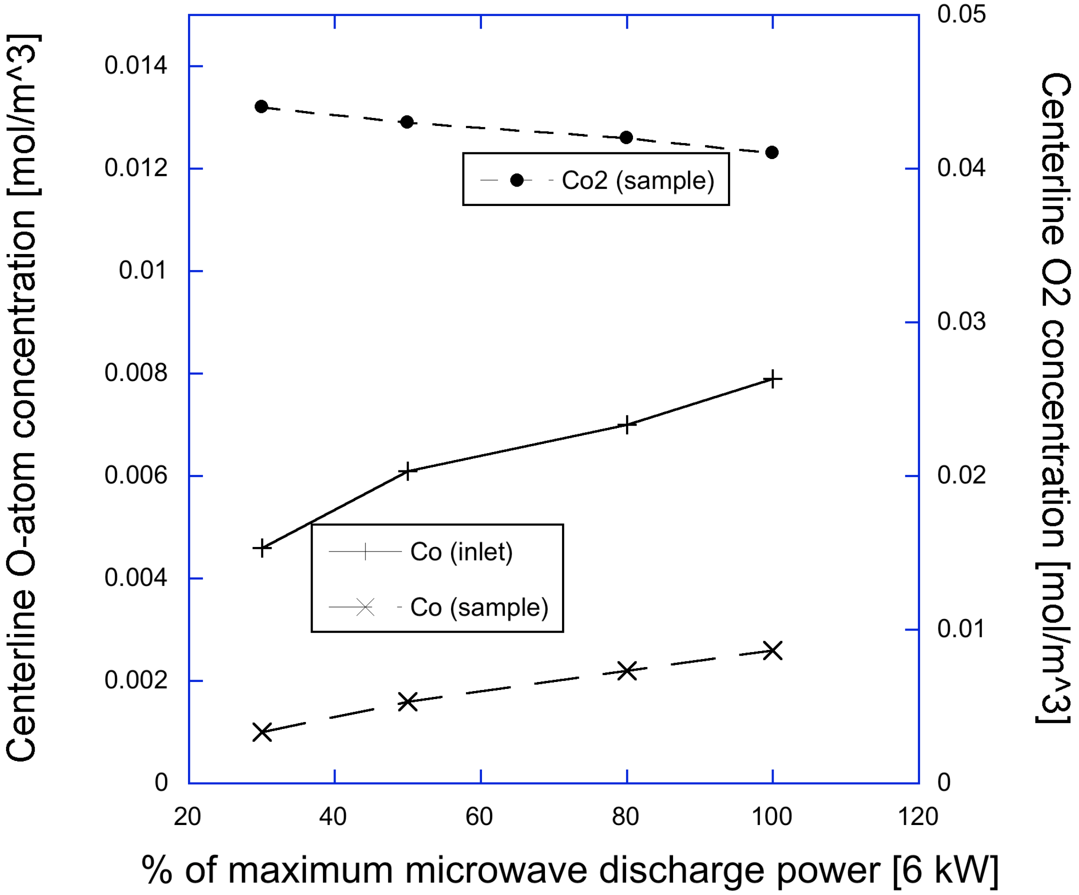

Figure 20: Average O-atom and O_2 concentrations near the sample and inlet for a flow rate of 2300 sccm (of 87% O_2–13% Ar gas mixture), outlet pressures of 431.3 Pa, furnace temperature of 1323 K (1050 °C), and at various MWPs

CHAPTER VI

OXIDATION MODELIING

Oxidation of Si (100)

The oxidation in the presence of O atoms was found to be ~ 15 times higher than that for dry thermal oxidation at same process conditions, as shown in Figure 21.

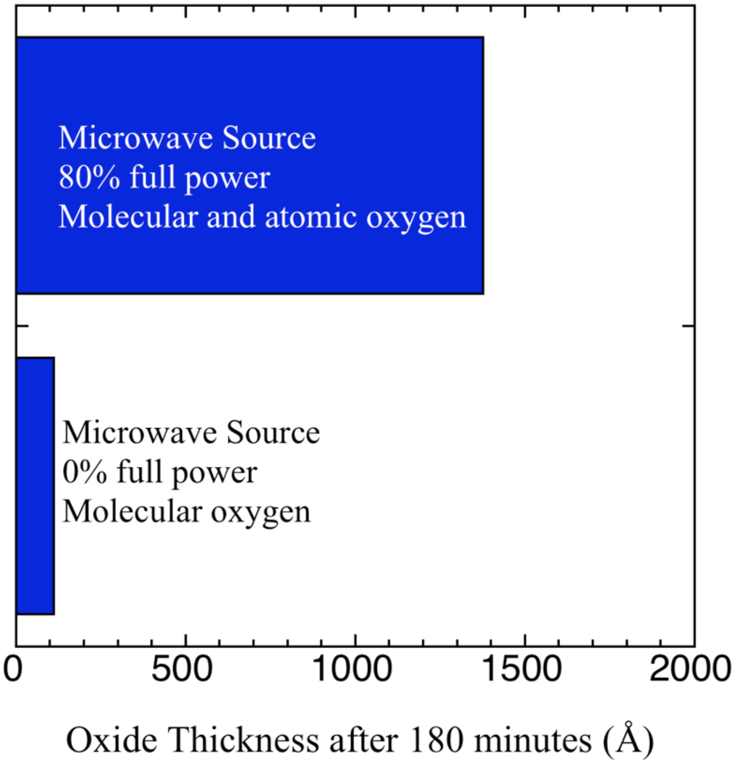

Figure 21: SiO_2 thicknesses for oxidation of Si (100) for 3 hours at 1323 K at a mass flow rate of 2300 sccm (of 87% O_2–13% Ar) gas mixture, 431.3 Pa outlet pressure, at 0% and 80 % of maximum microwave power.

The parallel oxidation model described in Chapter II was fitted to data (oxide thickness vs. time) collected at 1183 K and 1323 K. The governing equations were solved using COMSOL MULTIPHYSICS®, a finite element method software. Its compatibility with Matlab's Optimization toolbox, which uses a trust-region method for non-linear least squares curve fitting, was used to fit the model to the data. The parallel oxidation model has six parameters (diffusivities and reactivities of O_2 and O, solubility of O_2, and incorporation probability of O atoms on the oxide surface) that can be varied to fit the model to the data. To reduce the number of fitting parameters, the diffusivity, reactivity, and solubility for O_2 were fixed to the values from literature [11,15,91] as shown in Table 10. These values are well documented in the literature without any significant discrepancies.

Table 10: Parameters for O_2 at different temperatures fixed from literature

Parameter	**1183 K**	**1323 K**
Diffusivity of O_2, D_{O2} (m^2/s)	2.95×10^{-13}	5×10^{-13}
Solubility of O_2, α_{O2}	0.01	0.01
Reactivity of O_2, K_{O2} (m/s)	1×10^{-5}	1×10^{-5}
C_{gas_O} (mol/m^3)	2.43×10^{-3}	2.17×10^{-3}
C_{gas_O2} (mol/m^3)	0.047	0.04

These values were determined for dry thermal oxidation conditions. Hence in using these values assumption was made that the presence of O atoms in the oxidizing environment does not have any effect on the parameters for O_2. Fitting the model to the data for various fixed values of incorporation probability (α_o) of O atoms in the silica layer further reduced the number of fitting parameters. The average bulk gas concentrations near the oxide surface of O and O_2, shown in Table 10 were determined using the reactor model described earlier. This oxidation model, with diffusivity and reactivity of O atoms as fitting parameters, was then fitted to the data first by considering parallel oxidation by O_2 and O atom and then by O atom alone. This was done to understand the significance of O atom as an oxidizing species. Results tabulated in Tables 11 & 12 show that the parameters fitted to the data set at 1183 K and 1323 K respectively, have identical values whether oxidation by O_2 was considered or not. This suggests that the O atom is the dominant oxidizing species at these temperatures. The data colleted at 1183 K and 1323 K and the corresponding fits are plotted in Figure 22 and 23.

Table 11: Parameters determined by fitting the model to the data for oxidation of Si (100) at 1183 K, at a mass flow rate of 2300 sccm (of 87% O_2–13% Ar gas mixture), 431.3 Pa outlet pressure, and 80% maximum MWP for various α_o

Parameter	$\alpha_O = 0.1$	$\alpha_O = 0.5$	$\alpha_O = 1$
Diffusivity of O, D_O (m^2/s) (with O_2)	7.76×10^{-11}	1.53×10^{-11}	7.76×10^{-12}
Reactivity of O, K_O (m/s) (with O_2)	3.97×10^{-2}	7.95×10^{-3}	3.80×10^{-3}
Diffusivity of O, D_O (m^2/s) (without O_2)	7.7571×10^{-11}	1.55×10^{-11}	7.76×10^{-12}
Reactivity of O, K_O (m/s) (without O_2)	3.79×10^{-2}	7.6×10^{-3}	3.80×10^{-3}

Table 12: Parameters determined by fitting the model to the data for oxidation of Si (100) at 1323 K, at a mass flow rate of 2300 sccm (of 87% O_2–13% Ar gas mixture), 431.3 Pa outlet pressure, and 80% maximum MWP for $\alpha_o = 1$

Parameter	$\alpha_O = 0.1$	$\alpha_O = 1$
Diffusivity of O, D_O (m^2/s) (with O_2)	4.53×10^{-10}	4.53×10^{-11}
Reactivity of O, K_O (m/s) (with O_2)	9.42×10^{-3}	9.42×10^{-4}
Diffusivity of O, D_O (m^2/s) (without O_2)	4.54×10^{-10}	4.55×10^{-11}
Reactivity of O, K_O (m/s) (without O_2)	9.5×10^{-3}	9.46×10^{-4}

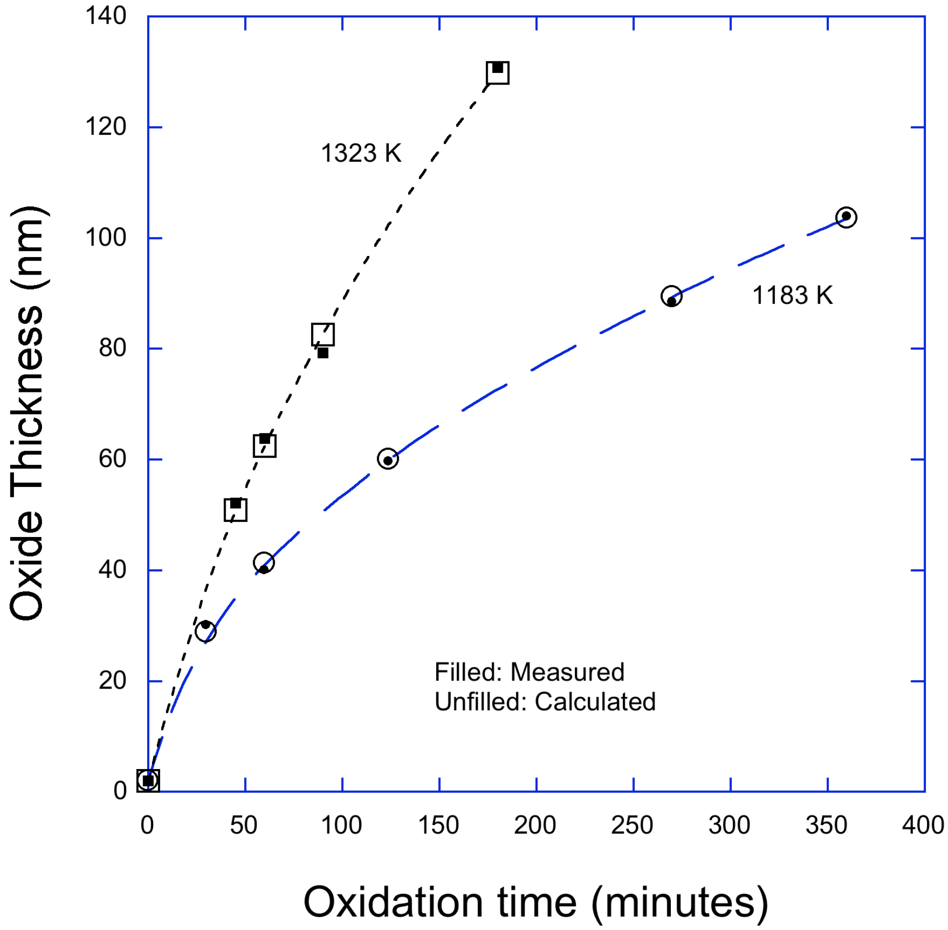

Figure 22: SiO_2 thicknesses for oxidation of Si (100) at various time and temperatures at a mass flow rate of 2300 sccm (of 87% O_2–13% Ar) gas mixture, 431.3 Pa outlet pressure, and 80 % of maximum MWP.

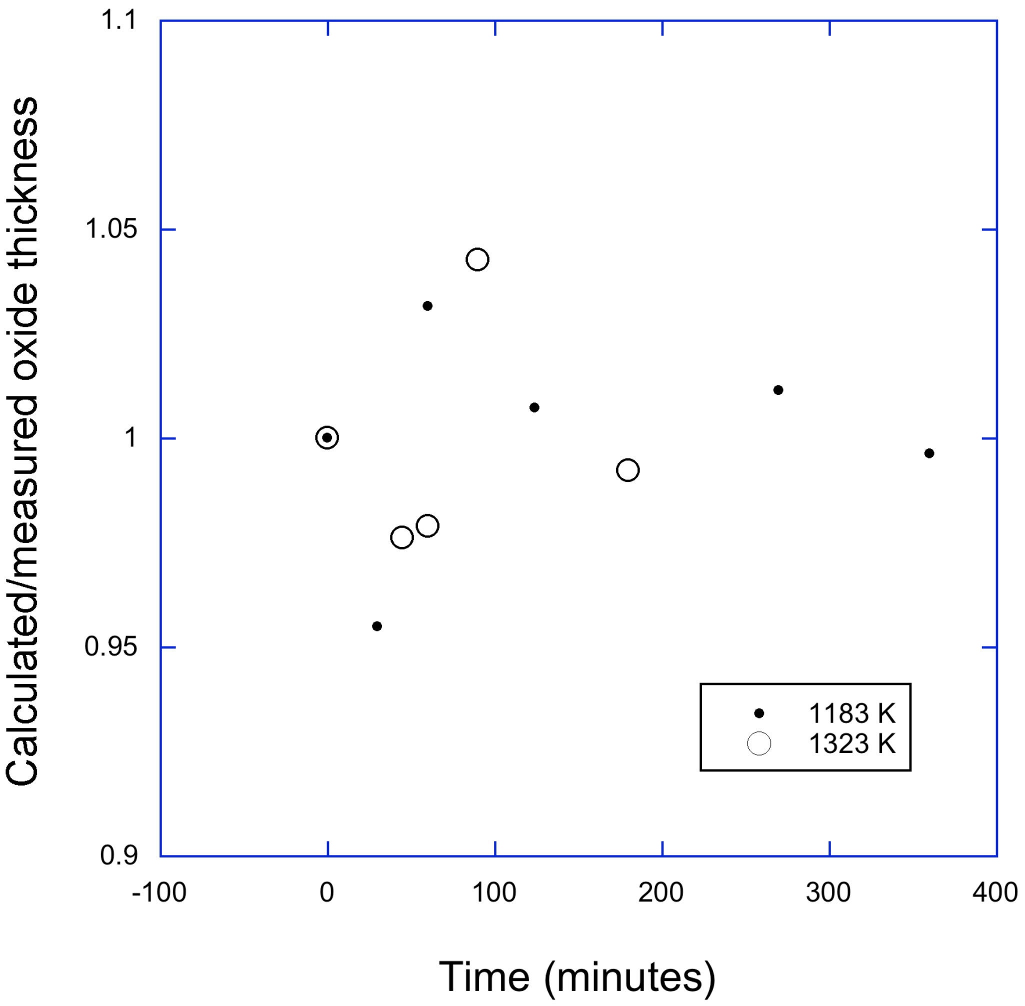

Figure 23: Ratio of calculated/measured SiO_2 thicknesses for oxidation of Si (100) at various time and temperatures at a mass flow rate of 2300 sccm (of 87% O_2–13% Ar) gas mixture, 431.3 Pa outlet pressure, and 80 % of maximum MWP.

Effect of O atom incorporation probability

As seen from Table 13 for the data set at 1183 K, the diffusivity (D_o) and reactivity (K_o) of O atoms change with the incorporation probability (α_o) such that the terms '$\alpha_O \times D_O$' and '$\alpha_O \times K_O$' always remain constant. This means that D_o and K_o change by a constant factor with the change in α_o. If the diffusivity or reactivity were the dominant parameter, then one would have changed differently than the other in response to a change in value of α_o. This suggests that the oxidation is not limited either by diffusion of

O atoms through the oxide surface or the subsequent reaction at the Si/SiO_2 interface but on the amount of O atoms incorporated at the oxide surface. This is consistent with the results from sequential ^{16}O – ^{18}O tracer experiments with and without O atoms in the gas bulk. Diffusion of tracer ^{18}O atoms through the network was seen only near the oxide surface in dry thermal oxidation conditions [26], while in the presence of ^{18}O atoms in the gas bulk [27] tracer atoms were found throughout the existing oxide even before any additional oxide growth was observed. Hence to get a better estimate of the diffusivity and reactivity values for O atoms, more fundamental research is needed to understand the incorporation of O atoms on the oxide surface.

Table 13: Parameters determined by fitting the model to the data for oxidation of Si (100) at 1183 K, at a mass flow rate of 2300 sccm (of 87% O_2–13% Ar gas mixture), 431.3 Pa outlet pressure, and 80% maximum MWP for various α_o

Parameter	**$\alpha_O = 0.1$**	**$\alpha_O = 0.5$**	**$\alpha_O = 1$**
$(\alpha_O \times D_O)$ (m^2/s) with O_2	7.76×10^{-12}	7.66×10^{-12}	7.76×10^{-12}
$(\alpha_O \times K_O)$ (m/s) with O_2	3.97×10^{-3}	3.97×10^{-3}	3.80×10^{-3}
$(\alpha_O \times D_O)$ (m^2/s) (without O_2)	7.76×10^{-12}	7.76×10^{-12}	7.76×10^{-12}
$(\alpha_O \times K_O)$ (m/s) (without O_2)	3.79×10^{-3}	3.8×10^{-3}	3.8×10^{-3}

Effect of O atom concentration on oxide thicknesses

To further explore the effect of O atoms on the oxidation of Si, we measured oxide thicknesses resulting from the use of various microwave powers (various O atom concentrations) at 1323 K and 431.3 Pa for 3 hours, using a flow rate of 2300 sccm (of a 87% O_2–13% Ar gas mixture). As discussed in Chapter V, increasing the microwave power at constant process conditions increases the O atom concentration without causing any significant change in O_2 concentration. This suggests that any change in oxide thickness with changing microwave power will be solely due to increasing O atoms in the oxidation environment. As shown in Figure 24, the measured O atom concentration at the entrance of the reactor and measured oxide thickness follow similar trend when plotted as a function of microwave power. This suggests an apparent dependence of oxide thickness on O atom concentration in the reactor.

To quantitatively establish this dependence, oxide thicknesses were calculated for various microwave powers using the O atom concentrations near the sample (calculated from the reactor model) and the diffusivity and solubility of O atom (extracted using the data collected at 1323 K at 80 % full microwave power) as inputs to the oxidation model. The incorporation probability ($\propto_o$) of O atoms on the oxide surface was assumed to be 1 in this analysis. As can be seen from Figure 25 and Table 14, the calculated oxide thicknesses for various microwave powers are within 10 % error range of the measured thicknesses. It was found that the calculated oxide thicknesses follow the same trend as the calculated O atom concentration near the oxide surface. Hence the difference in measured and calculated values seems to be introduced due to the bulk O-atom concentration used for various microwave powers.

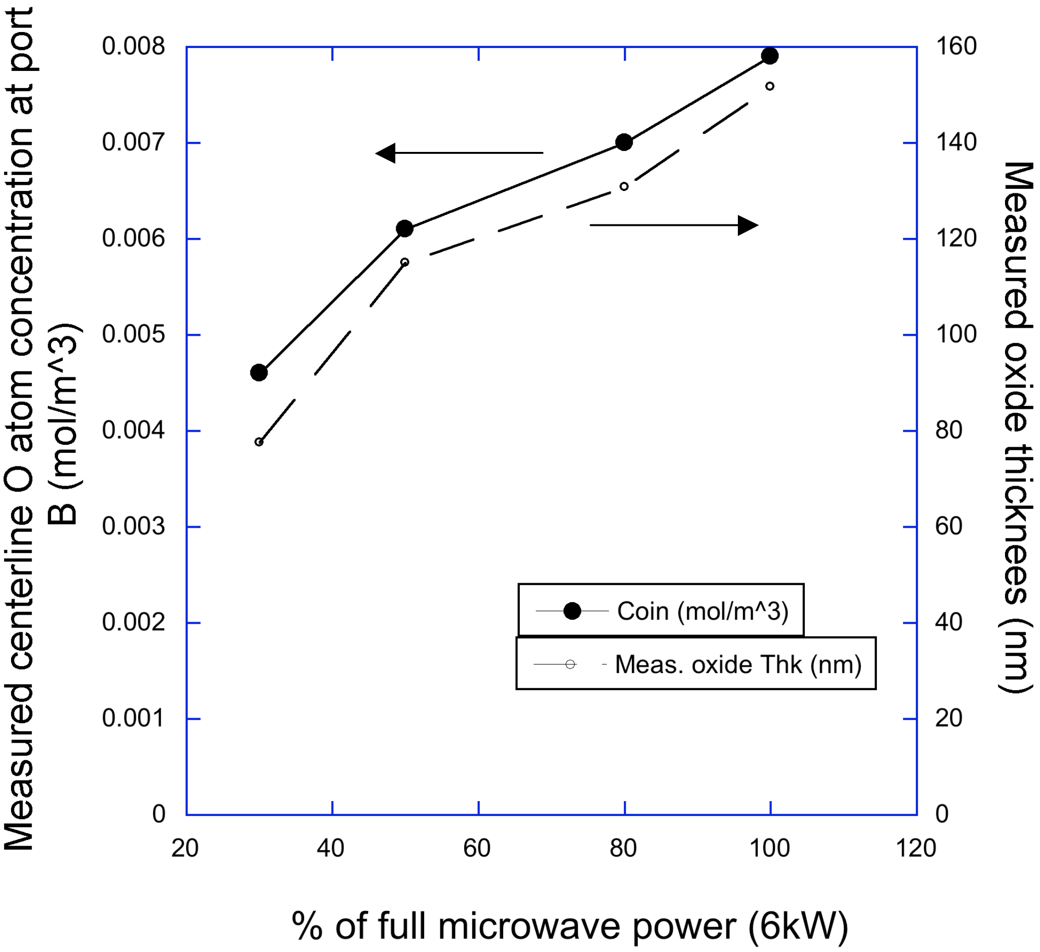

Figure 24: Oxide thickness (for the oxidation of Si (100) for 3 hours) and O atom concentration at the entrance measured for various MWPs, at a mass flow rate of 2300 sccm (of 87% O_2–13% Ar gas mixture), 431.3 Pa outlet pressure, and a furnace temperature of 1323 K.

This result confirms the dependence of oxide thickness on O atom concentration near the oxide surface. This also supports the validity of the model as it predicts the oxide thicknesses resulting from the use of various bulk O atom concentrations accurately, using the parameters extracted from the data set for a constant bulk O atom concentration. Similar analysis performed for an O atom incorporation probability of 0.1 gave identical results as seen in Figure 26. From the above results one can conclude that the number of O atoms available near the oxide surface have the dominant effect on the oxide thickness and not its incorporation probability on the oxide surface.

Table 14: Measured and calculated thicknesses for oxidation of Si (100) for 3 hours at various MWPs, at a mass flow rate of 2300 sccm (of 87% O_2–13% Ar gas mixture), 431.3 Pa outlet pressure, and a furnace temperature of 1323 K.

% of max Microwave power (6 kW)	c_{in_O} **(mol/m^3)**	c_{gas_O} **(mol/m^3)**	**Measured oxide thickness (nm)**	**Calculated oxide thickness (nm)**	**% difference in thickness values**
30	0.0046	0.001	77.6	77.9	0.39
50	0.0061	0.0016	115.06	106.5	7.44
80	0.007	0.0022	130.8	129.46	1.02
100	0.0079	0.0026	151.73	144.98	4.45

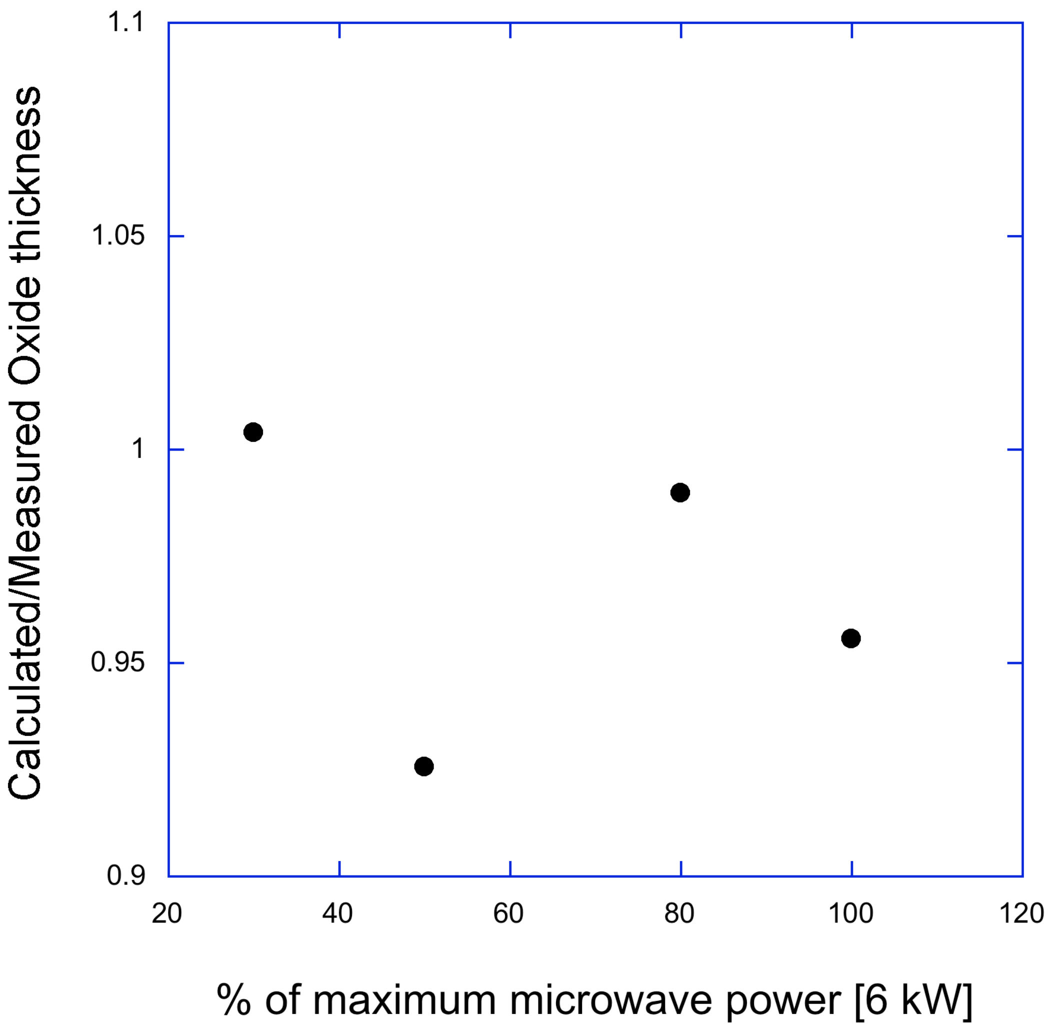

Figure 25: Ratio of calculated/measured SiO_2 thickness for oxidation of Si (100) for 3 hours for various MWPs, at a mass flow rate of 2300 sccm (of 87% O_2 – 13% Ar gas mixture), 431.3 Pa outlet pressure, furnace temperature of 1323 K, and for an α_o of 1.

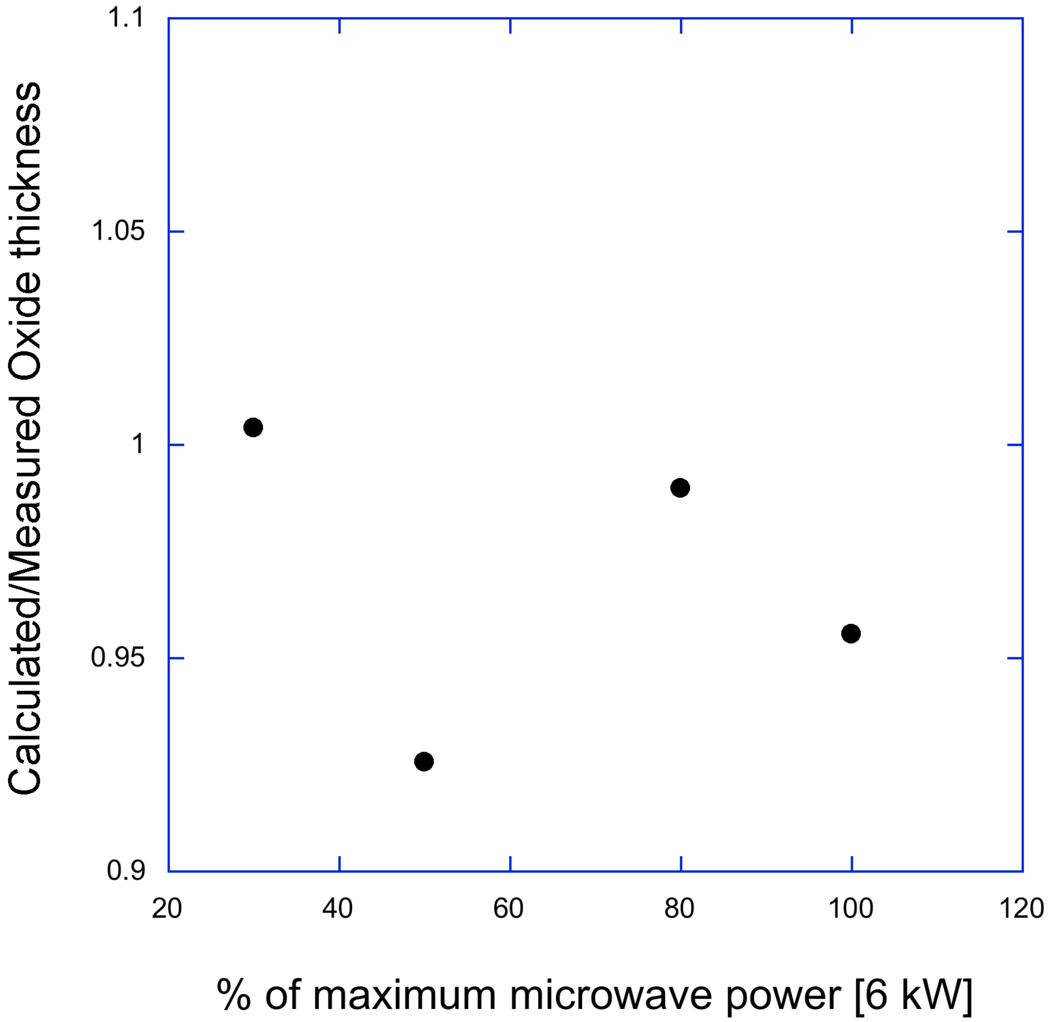

Figure 26: Ratio of calculated/measured oxide thickness for oxidation of Si (100) for 3 hours at various MWPs, at a mass flow rate of 2300 sccm (of 87% O_2–13% Ar gas mixture), 431.3 Pa outlet pressure, furnace temperature of 1323 K, and for an α_o of 0.1.

Effect of O atom diffusion on O_2 solubility

Peeters and coworkers had assumed that diffusing O atoms recombine in the oxide bulk. Hoshino and coworkers [92] using ab initio studies, claimed that two diffusing network O atoms energetically prefer to recombine into molecular O_2 when they are close to each other. Let us consider this case and assume that the molecular O_2 thus formed also has a dominant effect on the oxidation. If that was true, then the oxidation would have been limited by the solubility of O_2 in silica thus limiting the oxidation rate, unless the network modification effect of O atoms [24] increases the solubility of O_2 in the oxide scale. Assuming that the solubility of O_2 in the oxide scale is affected by this network modification, the solubility of O_2 (α_{O2}) was set to be 1 in the model. The diffusivity and reactivity of O_2 were fixed from the literature as shown in Table 10. α_O was set at 1 considering the rapid incorporation of O atoms on the oxide surface as proved in the last section. This model was then fitted to the data collected at 1323 K to determine the diffusivity and reactivity of O atoms. These determined parameters were then used to calculate the oxide thicknesses at various microwave powers using the procedure described earlier.

As shown in Figure 26, although the oxide thickness increases with the microwave power, there is a significant difference (more than 10 %) between the calculated and measured oxide thicknesses especially at lower O atom concentration near the oxide surface. This suggests that the model with increased solubility of oxygen (or significant role of both O and O_2 in the oxidation process) is not valid for predicting oxide thicknesses resulting from using other microwave powers than at which the model parameters were calculated.

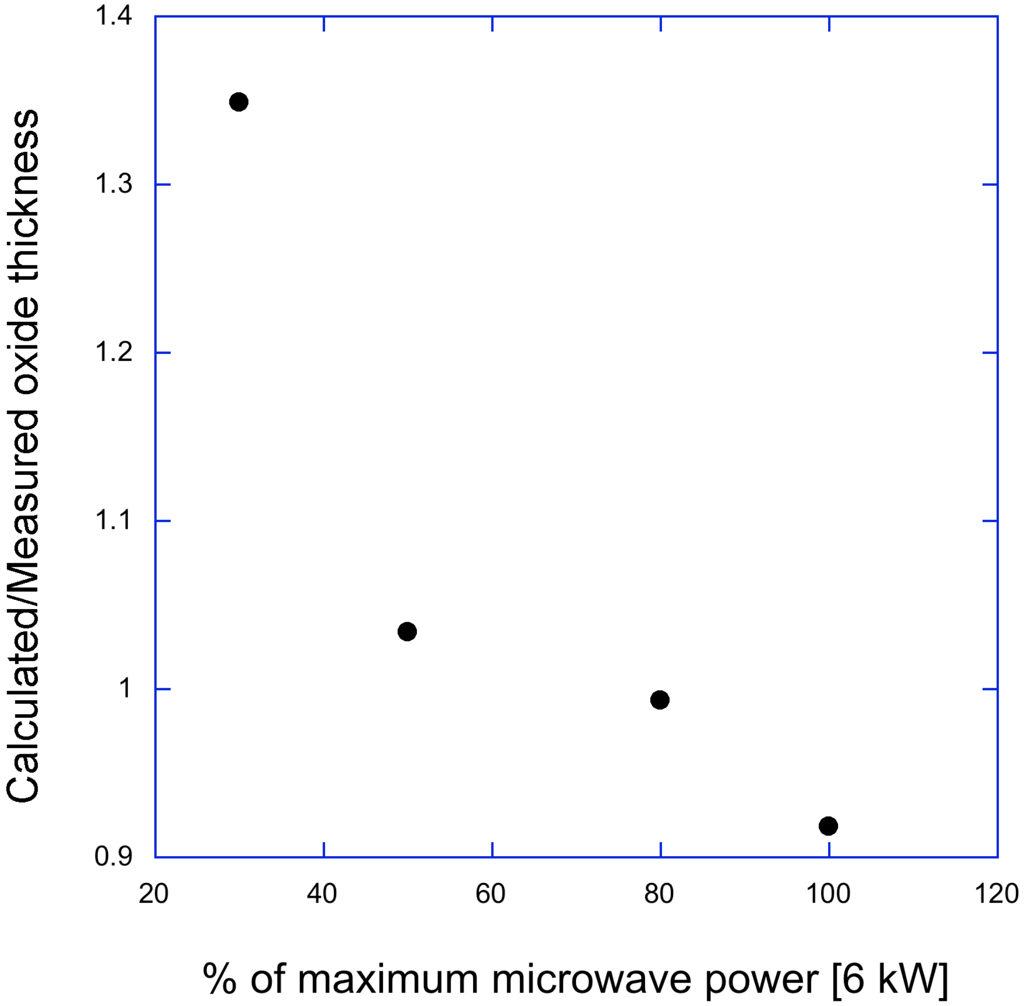

Figure 27: Ratio of calculated/measured oxide thickness (assuming an O_2 solubility of 1) for oxidation of Si (100) for 3 hours at various MWPs, at a mass flow rate of 2300 sccm (of 87% O_2–13% Ar gas mixture), 431.3 Pa outlet pressure, furnace temperature of 1323 K, and for α_o of 1

Above results indicate that atomic oxygen is the dominant oxidizing species in the afterglow region of the oxygen plasma, as was assumed by Peeters et.al [20]. But their assumption of unbound O atoms being responsible for the oxidation process seems unlikely. O atoms are incorporated into the oxide network at the surface and diffuse through the network for subsequent reaction with the Si at the Si/oxide interface. This was seen from the ^{18}O tracer experiments [27] as described earlier. Also, Tatsumura and coworkers [24] used an X-ray diffraction technique to demonstrate that the pre-existing silica network grown in molecular oxygen was modified by exposure to atomic oxygen, beginning at the outer surface and progressing inwards towards the oxide/Si interface, suggesting diffusion through the network.

Various possible mechanisms have been proposed to explain this diffusion of O atoms through the oxide network. Rochet and coworkers [26] qualitatively considered the role of network defects like oxygen vacancies or silicon dangling bonds in the diffusion process. Hamann [93] and Hoshino [92] used density functional theory calculations and proposed peroxyl linkages, an O atom incorporated into a Si-O-Si unit, to be responsible for the network diffusion of O atoms. Regardless of the mechanism of O atom diffusion through the network, it was found that neither the diffusion of O atoms at the surface nor its subsequent reaction with Si was the rate-limiting step as shown in Table 13. So the exaggerated growth can be attributed to the incorporation of the available O atoms on the oxide surface and then fast diffusion of O atoms through the network for subsequent reaction with the silicon.

A parallel can be drawn between the oxidation in presence of O atoms and the exaggerated oxide growth rate seen in the wet thermal oxidation of Si [11,27,94,95]. Kimura and coworkers [27] carried out plasma oxidation and wet thermal oxidation of Si, which was pre-oxidized using ^{18}O tracer plasma. They found decrease in tracer ^{18}O concentration profile throughout the previously grown oxide. This suggests that diffusion of the oxidizing species (O in case of plasma oxidation and OH in case of wet thermal oxidation) through the network for subsequent reaction with Si at the Si/oxide interface seems to be responsible for the higher oxide growth rate in both cases.

A parallel can also be drawn between dry thermal oxidation and oxidation in plasma afterglows. Results from tracer experiments [25,26] in dry $^{18}O_2$ environments suggest that permeation of molecular oxygen through the oxide interstices (without any interaction with the oxide structure) and its subsequent reaction with the Si at the Si/SiO_2 interface is primarily responsible for dry thermal oxidation of silicon, as assumed by the Deal Grove model [11]. But these experiments also showed some exchange of oxygen with the network oxygen close to the oxide/gas interface. Different mechanisms have been proposed to explain this interaction of oxygen with the oxide network [96]. One mechanism suggests exchange between the interstitially diffusing molecular oxygen and the silica network. Based on ab initio studies, Chelikowsky and coworkers [97], proposed the role of ozonyl linkages (Si-O-O-O-Si) in such an exchange. The other mechanism proposes incorporation of O_2 in the gas phase accompanied by dissociation to form O atoms at the oxide surface. The O atom then diffuses into the bulk silica [26]. If the exchange were taking place between the interstitially diffusing O_2 and the network O, it should have resulted in traces of ^{18}O throughout the oxide and just not near the gas/oxide interface. Although, the abrupt decrease in ^{18}O profile near the gas/oxide interface was attributed by the authors [26], to the limitation of the measuring technique. Still the fact remains that the measuring technique detected 7% of the ^{18}O near the gas/oxide interface and the rest near the oxide/Si interface and nothing was detected in between for thick oxides (thicknesses > 50 nm). This might suggests that the ^{18}O found near the surface was due to its incorporation at the oxide surface and subsequent diffusion towards the oxide/Si interface through the network [26]. This mechanism is similar to the diffusion mechanism of O atom in partially dissociated environments. Thus, the oxidation mechanism in dry O_2 seems to be similar to that in partially dissociated oxygen environment, i.e. parallel oxidation by O atom diffusing through the oxide network and O_2 diffusing through the interstitials.

Furthermore, this exchange at SiO_2/gas interface was found to be more significant in thinner films (lower oxidation times). This suggests that the parallel oxidation mechanism is significant in the early stages of the oxide growth. Thus, a parallel oxidation model such as that reported by Hans and coworkers [19] fits the measured oxide thickness vs. time data better than the Deal-Grove model for the entire thickness regime (including for thickness < 20 nm). A possible reason for this behavior might be the high activation energy involved in dissociation of O_2 to O atom on the already grown oxide surface, which limits the amount of O atoms available for diffusion through the network. A more fundamental study needs to be undertaken to understand the incorporation mechanism of O atoms on Si and SiO_2 surfaces. Thus as the oxide thickness increases (with time), the lower activation energy diffusion of O_2 through the interstitials becomes the dominant mechanism for the supply of oxidant to the Si/SiO_2 interface. Thus, in dry thermal oxidation of Si, the high initial oxide growth rate due to network diffusion of O atom stops due to the high-energy step (of dissociation of O_2 to O on the oxide surface) involved, it continues in partially dissociated oxygen environments due to the availability of free O atoms near the oxide surface as suggested by the tracer experiments [27].

Oxidation of LPCVD Si_3N_4

The oxide thicknesses for the oxidation of Si_3N_4 were found to be similar to that for Si oxidation when the oxidation was carried out with the microwave discharge turned *on* as compared to when the discharge was *off* at constant process conditions [36]. The slower oxide growth in dry thermal oxidation of Si_3N_4 has been attributed to the increased resistance to diffusion of O_2 molecules through the interstitials as discussed in Chapter II [40,98]. The fact that such a slow oxide growth is not seen in presence of O atoms in the oxidation environment suggests that the diffusion of O_2 through the interstitial does not play a significant role in case of Si_3N_4. One of the possible reasons for the exaggerated oxide growth rate on Si_3N_4 in oxygen plasma afterglow can be a similar diffusion mechanism of O atoms through the already existing oxide and fast reaction at the Si_3N_4/oxide interface, similar to that in oxidation of Si. So the oxidation in Si_3N_4 was modeled using the same model as that for Si, but considering only O atoms as the oxidizing species.

Tables 15 and 16 show the fitted parameters for 1183 K and 1323 K, respectively. The data colleted at 1183 K and 1323 K and the corresponding fits are shown in Figure 28.

Table 15: Parameters determined by fitting the model to the data for oxidation of LPCVD Si_3N_4 collected at 1183 K, at a mass flow rate of 2300 sccm (of 87% O_2–13% Ar gas mixture), 431.3 Pa outlet pressure, and 80% maximum MWP for various α_o.

Parameter	$\alpha_O = 0.1$	$\alpha_O = 1$
Diffusivity of O, D_O (m^2/s) (with O_2)	1.04×10^{-10}	1.04×10^{-11}
Reactivity of O, K_O (m/s) (with O_2)	8.67×10^{-2}	8.67×10^{-3}

Table 16: Parameters determined by fitting the model to the data for oxidation of LPCVD Si_3N_4 collected at 1323 K, at a mass flow rate of 2300 sccm (of 87% O_2–13% Ar gas mixture), 431.3 Pa outlet pressure, and 80% maximum MWP for various α_o.

Parameter	$\alpha_O = 1$
Diffusivity of O, D_O (m^2/s) (with O_2)	5.08×10^{-11}
Reactivity of O, K_O (m/s) (with O_2)	8.03×10^{-4}

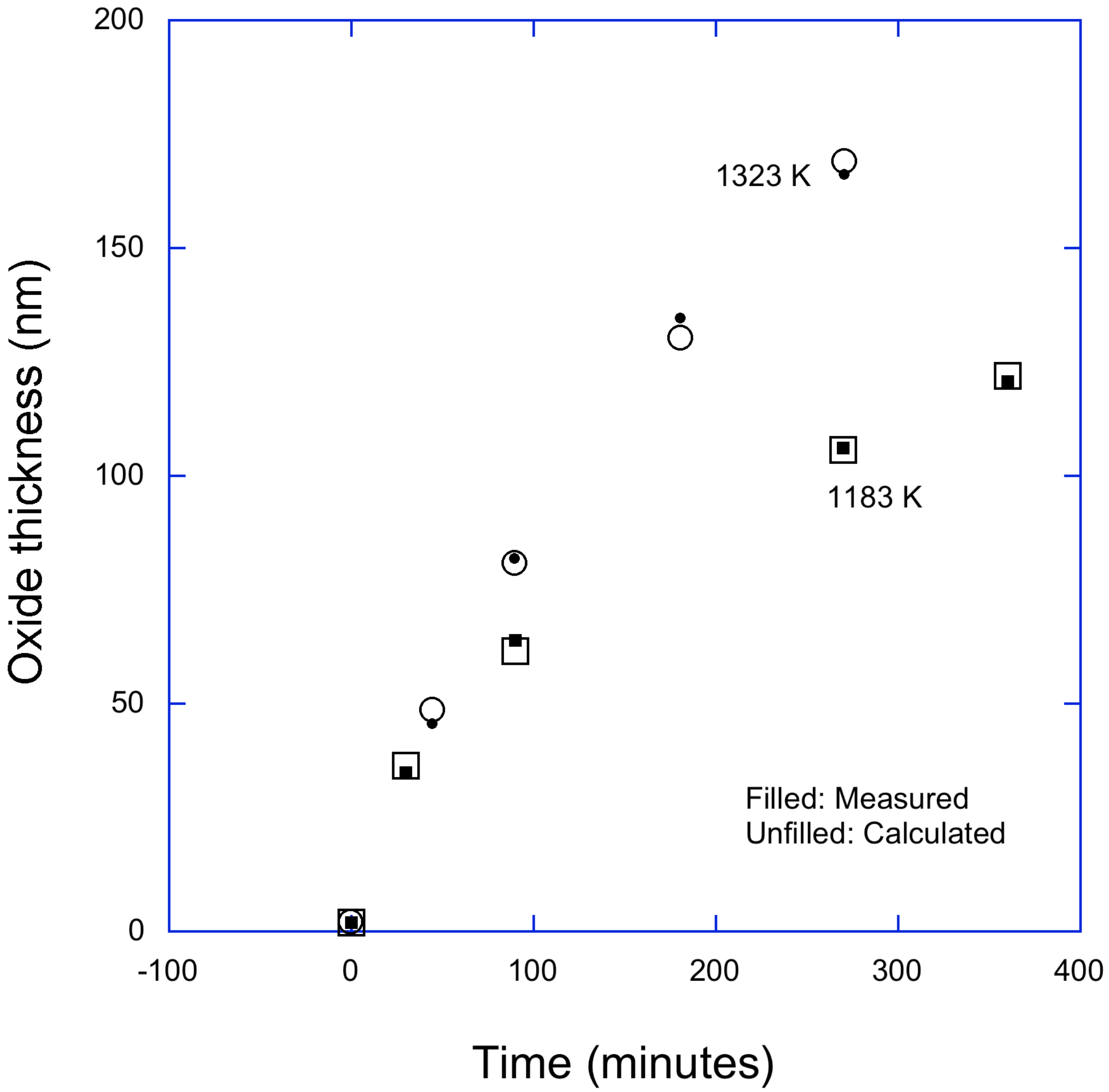

Figure 28: SiO_2 thicknesses for oxidation of LPCVD Si_3N_4 at various time and temperatures at a mass flow rate of 2300 sccm (of 87% O_2–13% Ar) gas mixture, 431.3 Pa outlet pressure, and 80 % of maximum microwave power.

For the data set at 1183 K, the diffusivity (D_o) and reactivity (K_o) of O atoms change with the incorporation probability (α_o) such that the terms '$\alpha_O \times D_O$' and '$\alpha_O \times K_O$' always remain constant. This means in this case too, the oxidation is not limited either by diffusion of O atoms through the oxide surface or the subsequent reaction at the Si/SiO_2 interface but on the amount of O atoms incorporated at the oxide surface. To determine if the oxidation process depends on α_o or on O atom concentration in the gas phase near the oxide surface, oxidation experiments on LPCVD Si_3N_4 should be carried out at different microwave powers at process conditions used for Si (100).

Oxidation of CVD SiC

The oxide thicknesses for the oxidation of CVD SiC was found comparable to that for the oxidation of Si (100) and LPCVD Si_3N_4 when the oxidation was carried out with the microwave discharge turned *on* as compared to when the discharge was *off* at constant process conditions [36]. Table 17 shows the fitted parameters at 1183 K. The data colleted at 1183 K and the corresponding fit are shown in Figure 29.

Table 17: Parameters determined by fitting the model to the data for oxidation of CVD SiC collected at 1183 K, at a mass flow rate of 2300 sccm (of 87% O_2–13% Ar gas mixture), 431.3 Pa outlet pressure, and 80% maximum MWP for various α_o.

Parameter	$\alpha_O = 0.1$	$\alpha_O = 1$
Diffusivity of O, D_O (m^2/s) (with O_2)	1.16×10^{-10}	1.16×10^{-11}
Reactivity of O, K_O (m/s) (with O_2)	50×10^{-2}	45×10^{-3}

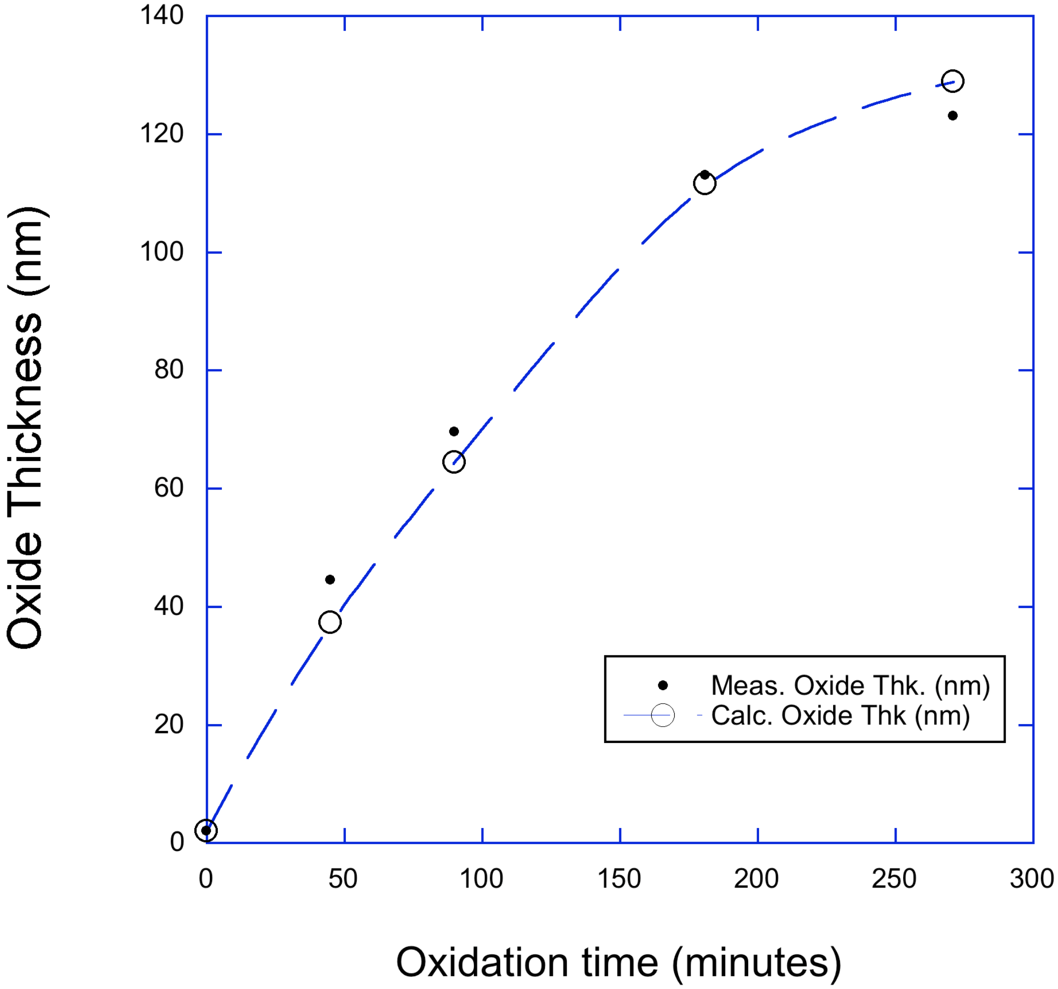

Figure 29: SiO_2 thicknesses for oxidation of CVD SiC at various time at 1183 K for a mass flow rate of 2300 sccm (of 87% O_2 – 13% Ar) gas mixture, 431.3 Pa outlet pressure, and 80 % of maximum microwave power.

The diffusivity (D_o) and reactivity (K_o) of O atoms change with the incorporation probability (α_o) such that the terms '$\alpha_O \times D_O$' and '$\alpha_O \times K_O$' always remain constant. This means in this case too, the oxidation is not limited by the amount of O atoms incorporated at the oxide surface. To determine if the oxidation process depends on α_o or on O atom concentration in the gas phase near the oxide surface, oxidation experiments on CVD SiC should be carried out at different microwave powers at constant process conditions.

CHAPTER VII

SUMMARY & CONCLUSIONS

A semi-empirical method is developed to study the quantitative effect of neutral O atoms on oxidation properties of UHTCs and their base materials at high temperatures and low pressures (133.33 Pa – 1333.33 Pa). The method is based on dissociating O_2 molecules in a microwave discharge and then directing the dissociated flow into a flow reactor equipped with a high-temperature furnace. The high temperature, non-isothermal, flowing oxygen plasma afterglow developed in the reactor is then characterized to determine the O atom density near the sample. The characterization method is based on using the measurements at lower temperatures (near the inlet of the reactor) as inputs to an axis-symmetric finite element model of the interior of the reactor maintained at higher temperatures. The model does that by taking into consideration the rapid temperature changes (both in the axial and radial direction) in the reactor and the effect of subsequent compressibility on the plasma afterglow chemistry and thus on the O atom concentration in the reactor. The model was used to calculate concentration profiles in the afterglow for conditions at which, oxidation experiments on UHTCs are carried out.

From our calculation we can conclude that, at high temperature and low-pressure oxidation conditions, the O atom concentration near the sample was significantly affected by the temperature and pressure (process parameters) rather than the recombination chemistry. The recombination of O atoms on the reactor wall was found to be dominant recombination mechanism. The rate of this recombination of O atoms at the reactor wall depends on the surface recombination coefficient (γ), which is the fraction of incident O atoms (on the wall) recombining to form O_2. Thus the O atom concentration near the sample is sensitive to the γ used.

At oxidation temperatures and pressure, axial diffusion was found to have negligible effect on O atom concentrations. The radial diffusion was fast enough to eliminate any radial concentration gradient resulting from the parabolic velocity profile and the recombination at the wall. Thus, the O atom concentration near the sample (0.3 m – 0.4 m) was found to be constant both in axial and radial direction. This is because of the temperature and pressure dependence of diffusivity (of O atom in O_2) used. This should be checked when using a different composition of the oxidizing gas mixture.

Furthermore, increasing the microwave discharge power resulted in a significant increase in O-atom concentration near the sample without any significant decrease in O_2. Thus, this is a good method to study the combined effect of O atom and O_2 on oxidation properties of a sample and then isolate the effect of O atoms by using different microwave discharge powers.

Using the above method, effect of neutral O atom on the oxidation of n type Si (100), LPCVD Si_3N_4, and CVD SiC was investigated in the temperature range of 900 °C – 1050 °C and at a pressure of 431.3 Pa. Oxide thickness in presence of O atoms was ~20 times that for dry thermal oxidation at similar process conditions [43]. Oxide thickness was found to be influenced predominantly by the bulk O atom concentration near the oxide surface than any other process parameter. Molecular oxygen was found to play an insignificant role in the oxidation process. From these results we can conclude that the availability of free O atoms near the surface, their incorporation at the oxide surface, fast diffusion through the network, and their reaction with Si at the oxide/Si interface is responsible for the high oxide growth rate. This means that the oxide thicknesses on Si in an oxygen plasma afterglow can be controlled by controlling just the dissociation fraction of O_2 at temperatures and pressures considered.

Similar conclusions can be made regarding the oxidation mechanism of LPCVD Si_3N_4 and CVD SiC in presence of O atom, although some more work is required to confirm this.

Future Work

Future efforts should be directed towards confirming the dominant effect of O atom density in the bulk on oxidation of Si_3N_4 and SiC at temperatures and pressures already considered. This can be done by carrying out the oxidation at various microwave powers at constant process conditions.

Furthermore, oxidation of silica formers (base materials for UHTCs) should be carried out at higher temperatures than that considered to determine the active-to-passive transition in this pressure range. This is because the UHTCs are exposed to higher temperatures (than that considered) in their application environment. Thus it is important to know if the silica formers will form a protective oxide scale (passive oxidation) or undergo etching (active transition) at those conditions. Also, this analysis should be carried out on silica formers processed using different processing methods to understand the effect of processing-property relationship on the passive-to-active transition.

The next step should be to understand the oxidation mechanism of ZrB_2/HfB_2 at these conditions of high temperature and low pressure using the method describe in this work and then of the composite (ZrB_2/HfB_2 –SiC) itself.

Appendix A

A1. Mean free path

$$\lambda = \frac{RT}{\sqrt{2}\pi d^2 p N_{Av}}$$

where, λ is the mean free path in m,

R is the universal Gas constant = 8.314 kg-m^2/s^2/mole/K,

T is the temperature in Kelvin,

d_m is the diameter of the atom/molecule in m,

p is the pressure in Pa,

and N_{av} is the Avagadro's number = 6.023×10^{23} /mole

Using the above formula the mean free path for oxygen molecules (87% of the gas mixture) was calculated at a pressure of 3.2 Torr (431.3 Pa) and a temperature of 300 K and 1300 K as follows.

T (K)	**λ_{O2} (m)**	**λ_{O} (m)**	**λ_{Ar} (m)**
300	1.5×10^{-5}	9.4×10^{-5}	5.2×10^{-5}
1500	7.3×10^{-5}	4.7×10^{-4}	2.6×10^{-4}

A2. Knudsen number

$$K_n = \frac{\lambda}{d_l}$$

where, K_n is the Knudsen number,

λ is the mean free path in m,

d_l is characteristic length (diameter of the tube in this case) in m.

Using the above formula the Knudsen number was calculated at a pressure of 3.2 Torr (431.3 Pa) and a temperature of 300 K and 1500 K as follows.

T (K)	Kn_{O2}	Kn_{O}	Kn_{Ar}
300	6.6×10^{-4}	4.3×10^{-3}	2.3×10^{-3}
1500	3.3×10^{-3}	0.021	0.011

Thus, the flow was **continuous** for the conditions considered.

A3. Properties of pure gases – used in following calculations [68]

Property	O_2	Ar	O	O_3
Tc (K)	154.6	150.8	154.3	260.95
Pc (Pa)	5.03×10^{6}	4.87×10^{6}	4.97×10^{6}	5.573×10^{6}
M (gm/mol)	32	40	16	48

A4. Reynolds's Number

Reynolds's number was calculated using the formula,

$$\mathrm{Re} = \frac{\mathrm{D}\mathrm{v}\rho}{\mu}$$

D → Characteristic length (cm)
v → Linear Velocity (cm/sec)
ρ → Mass Density (gm/ cm^3)
μ → Kinematic Viscosity (gm/(cm.sec))

A5. Viscosity – Corresponding States Method – Lucas Method [69]

$$\text{Reduced Viscosity}\left(T_r\right) = \xi\eta = fP\left(T_r\right)$$

where,

$$\xi\eta = \left[0.807\,T_r^{0.618} - 0.357\,e^{-0.449Tr} + 0.340\,e^{-4.058Tr} + 0.018\right]F_p^0 F_Q^0$$

Since O_2, N_2, Ar are non polar, so $F_p^0 = F_Q^0 = 1$

$$\xi = \left[\frac{8314\,T_c\left(No\right)^2}{M^3 P_c{}^4}\right]^{1/6}$$

$$\xi \rightarrow m^2 / N.s$$

$$T_c \rightarrow K$$

$$P_c \rightarrow Pa$$

$$M \rightarrow g/mol$$

$$\eta = \frac{\xi\eta}{\xi}$$

The viscosity of the gas mixture was determined from the viscosities of the individual species by assuming ideal gas mixture. At a pressure of 431.3 Pa (3.2 Torr), the viscosity of the gas mixture, density (calculated using the ideal gas law), and the Reynold's number are as follows,

T (K)	**μ (N.s/m^2)**	**ρ (kg/m^3)**	**Re**
300	2.08×10^{-5}	5.65×10^{-3}	156.5592
1300	5.79×10^{-5}	1.31×10^{-3}	56.2793

So the flow is **continuous, compressible, and laminar**.

A6. Diffusion coefficients in O_2

O_2 (carrier gas) constitutes 87 % of the gas mixture and so only the diffusion of other species in O_2 was considered. Inter-diffusion among species was neglected. Diffusion coefficients of O_3 and Ar in O_2 were determined using the expressions for binary mixture: [69] as described below.

$$D_{AB} = \frac{0.00266\,T^{3/2}}{P\,M_{AB}^{1/2}\,\sigma_{AB}^{2}\,\Omega_D}$$

where,

D_{AB} = diffusion coefficient, cm^2/sec

T = temperature, K

P = pressure, bar

σ_{AB} = characteristic length, A^0

Ω_D = diffusion collision integral, dimensionless

$$\sigma_{AB} = \frac{\sigma_A + \sigma_B}{2}; \qquad \varepsilon_{AB} = \left(\varepsilon_A \varepsilon_B\right)^{1/2}; \qquad T^* = kT/\varepsilon_{AB}$$

$$\Omega_D = \frac{1.06036}{\left(T^*\right)^{0.15610}} + \frac{0.19300}{\exp\left(0.47635\,T^*\right)} + \frac{1.03587}{\exp\left(1.52996\,T^*\right)} + \frac{1.76474}{\exp\left(3.89411\,T^*\right)}$$

Diffusion of O-atoms in O_2 was calculated as a function of temperature and pressure using the empirical relations suggested by Pallix *et.al* [70].

$$D_o = D_{rt}\,(T/T_{rt})^{1.64}\,(P_{atm}/P)$$

where,

D_{rt} is the diffusion coefficient at room temperature (T_{rt} = 298K) and atmospheric pressure (P_{atm} = 760 Torr) = 0.365 cm^2/sec

T is in K, P is in Torr, and

D_o is in cm^2/sec

A7. Heat transfer coefficient of the fluid (h)

Heat transfer coefficient for the forced convection of the gas mixture [67] inside a tube, used for determining the Biot number, was calculated as shown below,

$$\frac{h}{c_{pmix}G} = \frac{1.86}{\left(c_{pmix}\mu_{mix}/k_m\right)^{2/3}\left(D_iG/\mu_{mix}\right)^{2/3}\left(L/D_i\right)^{1/3}\left(\mu_w/\mu_b\right)^{0.14}}$$

where,

h → heat transfer coefficient of the gas mixture in $W/(m^2.K)$,

c_{pmix} → heat capacity of the gas mixture in kJ/(kg).K,

k_m → heat transfer coefficient of the gas mixture in W/m.K,

μ_{mix} → kinematic viscosity of the gas mixture in cP,

μ_w → kinematic viscosity at wall temperature in cP,

μ_b → kinematic viscosity at bulk temperature in cP,

L → Length of the reactor in m,

D_i → Diameter of the reactor in m, and

G → mass velocity in kg/(hr. m^2)

A8. Biot Number

$$B_i = \frac{\text{Solid resistance}}{\text{Fluid resistance}} = \frac{h_f t_r}{k_s}$$

where,

h_f is the heat transfer coefficient in $W/(m^2.K)$

t_r is the thickness of the tube in m, and

k_s is the thermal conductivity of solid in W/(m.K)

For the case when the discharge is on and furnace is off, the centerline temperature at PMT2 for 80% MWP was 560 K and the wall temperature was 345 K. At these temperatures, the heat transfer coefficient for the gas mixture in contact with quartz wall is h_f = 7.587 $W/(m^2.K)$ and thermal conductivity of the quartz wall is k_s = 1.4 W/(m.K). Assuming a wall thickness of 1cm, Biot number was found to be 0.054. This means heat transfer encounters negligible resistance in the solid and so the inner wall temperature is the same as outer wall temperature.

A9. Heat capacity

Heat capacity for O_2, O_3, and Ar were determined using the expression [69] as shown below,

$$c_p = R(a0 + a1T + a2T^2 + a3T^3 + a4T^4)$$

where,

c_p is the heat capacity in J/mol/K,

R is the universal gas constant in J/mol/K, and

a0 - a4 are constants specific to the species under consideration

The constants used are as follows

Species	***a0***	***a1* × 10^3 (1/K)**	***a2* × 10^5 $(1/K)^2$**	***a3* × 10^8 $(1/K)^3$**	***a4* × 10^{11} $(1/K)^4$**
Ar	2.5	0	0	0	0
O_2	3.63	-1.794	0.658	-0.601	0.179
O_3	4.106	-3.809	3.131	-4.3	1.813

Heat capacity of O-atom used (14.72 J/mol/K) was found on the world wide web [99]. The heat capacity of the mixture was then determined from the heat capacities of individual species by assuming ideal gas mixture.

A.10 Thermal conductivity

Thermal conductivity of Ar and O_2 were determined using the following expression [69]:

$$k = A + BT + CT^2 + DT^3$$

where,

k is the thermal conductivity in W/(m.K),

T is in Kelvin, and

A, B, C, and D are the constants specific to the gas being considered

Species	**A (W/m/K)**	**B (W/m/K^2)**	**C (W/m/K^3)**	**D *(W/m/K^4)***
Ar	2.714×10^{-3}	5.54×10^{-5}	-2.18×10^{-8}	5.54×10^{-12}
O_2	-3.273×10^{-4}	9.97×10^{-5}	-3.743×10^{-8}	9.732×10^{-12}

Thermal conductivity of O-atom used (0.027 W/m/K) was found on the world wide web [99]. The thermal conductivity of the mixture was then determined from the thermal conductivity of individual species by assuming ideal gas mixture.

A11. Reaction rates

The rates of consumption/generation of various species as accounted for in the mass balance are as follows,

$$\begin{aligned}
R_O = \frac{dc_O}{dt} = &-2c_O^2\left(K_{1,O}c_O + K_{1,O_2}c_{O2} + K_{1,O_3}c_{O3}K_{1,Ar}c_{Ar}\right)\\
&-c_O c_{O2}\left(K_{2,O}c_O + K_{2,O_2}c_{O2} + K_{2,O_3}c_{O3} + K_{2,Ar}c_{Ar}\right)\\
&-c_O c_{O3}K_3\\
&+c_{O3}\left(K_{4,O}c_O + K_{4,O_2}c_{O2} + K_{4,O_3}c_{O3} + K_{4,Ar}c_{Ar}\right)
\end{aligned}$$

$$\begin{aligned}
R_{O2} = \frac{dc_{O2}}{dt} = &\,c_O^2\left(K_{1,O}c_O + K_{1,O_2}c_{O2} + K_{1,O_3}c_{O3} + K_{1,Ar}c_{Ar}\right)\\
&-c_O c_{O2}\left(K_{2,O}c_O + K_{2,O_2}c_{O2} + K_{2,O_3}c_{O3} + K_{2,Ar}c_{Ar}\right)\\
&+2c_O c_{O3}K_3\\
&+c_{O3}\left(K_{4,O}c_O + K_{4,O_2}c_{O2} + K_{4,O_3}c_{O3} + K_{4,Ar}c_{Ar}\right)
\end{aligned}$$

$$\begin{aligned}
R_{O3} = \frac{dc_{O3}}{dt} = &\,c_O c_{O2}\left(K_{2,O}c_O + K_{2,O_2}c_{O2} + K_{2,O_3}c_{O3} + K_{2,Ar}c_{Ar}\right)\\
&-c_O c_{O3}K_3\\
&-c_{O3}\left(K_{4,O}c_O + K_{4,O_2}c_{O2} + K_{4,O_3}c_{O3} + K_{4,Ar}c_{Ar}\right)
\end{aligned}$$

In the following:

- Bimolecular rate constants are in m^3 $molecule^{-1}$ s^{-1}.
- Termolecular rate constants are in m^6 $molecule^{-2}$ s^{-1}.
- Temperatures is in K

The rate constants reported in the literature are in cm^3 $molecule^{-1}$ s^{-1} and cm^6 $molecule^{-2}$ s^{-1} as tabulated in Table 4. These were converted to m^3 $molecule^{-1}$ s^{-1} and m^6 $molecule^{-2}$ s^{-1} before using them in the model.

APPENDIX B

Reactor Model

In this chapter, various COMSOL MULTIPHYSICS® models used for representing different process conditions are discussed in detail. The governing PDEs are solved in the defined solution region (subdomain) by entering them in the software in their general form as shown,

$\nabla \bullet \Gamma = f$

where, $\nabla \bullet \Gamma(\nabla \bullet tau)$ is the diffusive component of the equation, and

f consists of the convective terms and the source terms

The equations are then solved using the boundary condition, which aree expressed in the following form,

$-n \bullet \Gamma = G1 + \left(\frac{\partial R1}{\partial u}\right)^T \mu$ Neumann boundary condition

$0 = \mathrm{R1}$ Dirchlet boundary condition

where, G1 and R1 are the required inputs,

u is the dependent variable, and

μ is the Lagrange multiplier

The boundary conditions for each governing PDE are entered into the software by specifying G1 and/or R1.

The constants, expressions, and terms *'tau', 'f','G1'*, and '*R1*' used for different equations are discussed in the description of individual models below.

Notes about COMSOL syntax:

- The first and second derivative of a dependent variable (e.g. ‘u’) w.r.t. say ‘x’ is represented as ux and uxx, respectively.
- First and second derivative of any other variable (e.g. ‘var’) w,r,t, say ‘x’ is represented by diff(var,x) and diff((diff(var,x),x), respectively.
- The term ‘k2ar(T)’ means that k2ar is defined as a function of T in the model

Model I. Isothermal flow at 300 K with afterglow chemistry

1. Table of Contents

2. Model description

This model was developed for a isothermal (300 K) reactive flow of 2300 sccm of 87% O_2 – 13% Ar, at an outlet pressure of 431.3 Pa, and 80% of maximum discharge power. Details of the model are as follows:

Inputs:
1. Parabolic entrance velocity (profile) (m/s)
2. Outlet Pressure (Pa)
3. Concentration profile at the entrance (of various species) – measured concentration at the centerline (mol/m^3)
4. Rate constants suggested in the literature for various bulk O-atom recombination reactions

5. Surface recombination coefficient (1e-4) for the heterogeneous recombination of O-atoms at the wall

Outputs:
1. Concentration profiles of various species in the reactor

The model consists of following equations:
1. Momentum Balance to solve for velocity in the x (u) and y (v) direction and pressure (p) represented by equations g, g2, and g3, respectively
2. Individual mass balances to solve for concentrations of O-atoms (co), O_3 (co3), and argon (car) represented by equations g4, g5, and g6, respectively.

3. Constants

Name	Expression	Description
Mo2	0.032	kg/mol – Mol.wt of O_2
Mo	0.016	kg/mol – Mol. Wt of O
Mar	0.040	kg/mol – Mol. Wt of O3
Tco2	154.6	K – Critical T of O_2
Pco2	5040000	Pa – Critical P of O_2

Tco	154.3	K – Critical T of O
Pco	4970000	Pa – Critical P of O
no	6.023e26	molecules/mol – Avogadro’s Number
R	8.314	J/(mol.K) – Universal Gas Constant
Tcar	150.8	K – Critical T of Ar
Pcar	4870000	Pa – Critical p of Ar
Mo3	0.048	kg/mol – Mol.wt of O_3
Tco3	260.95	K – Critical T of O_3
Pco3	5573000	Pa – Critical P of O_3
e_k	(124*113)^0.5	Constant used in the calculation of D2
s_ab	(3.433+3.418)/2	Constant used in the calculation of D2
mab	2/((1/32)+(1/40))	Constant used in the calculation of D2
co3i	1e-5	mol/m^3 – O_3 concentration at the inlet
po	431.3	Pa - Outlet Pressure
um	24.5	m/s – Mean velocity at the inlet
g	9.8	m/s^2 – Acceleration due to gravity
gamma	1e-4	Surface recombination coefficient
T	300 K	Isothermal temperature of the flow
Do	0.365e-4	Constant used for calculating D1

4. Expressions

Name	**Expression**	**Unit**
xo	co/C	mole fraction of O
co2	C-car-co3-co	mol/m^3 – O_2 concentration
xo3	co3/C	mole fraction of O
xar	1-xo-xo3-xo2	mole fraction of Ar
M	xo*Mo+xo2*Mo2+xo3*Mo3+xar*Mar	kg/mol – Mol.wt of the gas mixture
Pcm	xo*Pco+xo2*Pco2+xar*Pcar+xo3*Pco3	Pa – Critical P of the gas mixture
Tcm	xo*Tco+xo2*Tco2+xar*Tcar+xo3*Tco3	K – Critical T of the gas mixture
evis	(8314*Tcm*no^2/(M*1000)^3/Pcm^4)^(1/6)	Used in Viscosity calculation
te	T/Tcm	Used in Viscosity calculation
ne	0.018+0.807*te^0.618-0.357*exp(-0.449*te)+0.34*exp(-4.058*te)	Used in Viscosity calculation
rho	p*M/R/T	kg/m^3 – Density of gas mix.
mu	ne/evis	Pa.s – Viscosity of the gas mix.
D1	Do*760/(25/3333*p)*(T/298)^1.64	m^2/s – Diff. coeff. Of O in O_2
C	p/R/T	mol/m^3 – Total conc.
Ts	T/e_k	Used in calculation of D2
omeg	1.06036/Ts^0.1561+0.193/exp(0.47635*Ts) +1.03587/exp(1.52996*Ts) +1.76474/exp(3.89411*Ts)	Used in calculation of D2
D2	2.66E-7*T^1.5/(1.0E-5*p)/	m^2/s – Diff. Coeff of Ar in O_2

	mab^0.5/s_ab^2/omeg	
k1ar	5.2e-35*exp(900/T) *(6.023e23)^2/(1e6)^2	Rate const. For rxn (1) m^6/mol^2/s
k1o	k1ar	m^6/mol^2/s
k1o2	k1ar	m^6/mol^2/s
k1o3	k1ar	m^6/mol^2/s
k2o2	1.5*k2	m^6/mol^2/s – Rate const. for rxn (2)
k2o	k2o2	m^6/mol^2/s
k2o3	k2o2	m^6/mol^2/s
k4o3	7.16e-10*exp(-11180/T)*6.023e17	m^3/mol/s – Rate const. for rxn(4)
k4ar	0.25*k4o3	m^3/mol/s
k4o2	0.5*k4o3	m^3/mol/s
k4o	k4o2	m^3/mol/s
rxno	-2*co^2*(k1o*co+k1o2*co2+k1o3*co3+k1ar*car)-co*co2*(k2o*co+k2o2*co2+k2o3*co3+k2ar(T)*car)-co*co3*k3+co3*(k4o*co+k4o2*co2+k4o3*co3+k4ar*car)	mol/m^3/s – Rate of formation of O
rxno2	co^2*(k1o*co+k1o2*co2+k1o3*co3+k1ar*car)-co*co2*(k2o*co+k2o2*co2+k2o3*co3+k2ar(T)*car) +2*co*co3*k3+co3*(k4o*co+k4o2*co2+k4o3*co3+k4ar*car)	mol/m^3/s – Rate of formation of O_2
rxno3	co*co2*(k2o*co+k2o2*co2+k2o3*co3 +k2ar(T)*car)-co*co3*k3-co3*(k4o*co+ k4o2*co2+k4o3*co3+k4ar*car)	mol/m^3/s – Rate of formation of O_3
k2	k2ar(T)	Rate const. for rxn (2) as a function of T
k3	(8e-12*exp(-2060/T))*6.023e17	m^3/mol/s – Rate const. for rxn (3)
rso	(gamma*36.39*T^0.5*co/4)	m^2/mol/s - Rate of surface rxn
xo2	co2/C	mole fraction of O_2
coi	3.4e15/6.023e23*1e6	Conc. of O at inlet
cari	0.13*458/R/T	mol/m^3 - Conc. of Ar at inlet
co3avg	co3a/(0.011*0.76)	mol/m^3 - Avg. O_3 conc in the reactor

5. Geometry

Space dimensions: 2D

Independent variables: x, y, z

5.1 Mesh Statistics

Number of degrees of freedom	5750
Number of mesh points	305

Number of elements	240
Triangular	0
Quadrilateral	240
Number of boundary elements	128
Number of vertex elements	4
Minimum element quality	0.415
Element area ratio	1

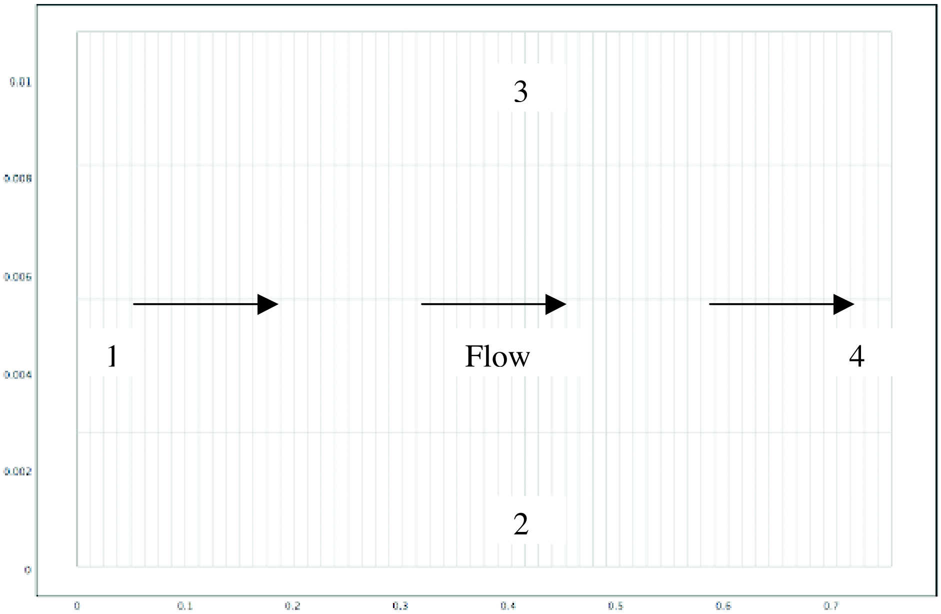

6.1 Application Mode: PDE, General Form (g)

Application mode type: PDE, General Form

Application mode name: g

6.1.1. Application Mode Properties

Property	**Value**
Default element type	Lagrange - Quadratic
Wave extension	Off
Weak constraints	Off

6.1.2. Variables

Dependent variables:	u, u_t – **x- component of the velocity (m/s)**
Shape functions:	shlag(2,'u')

Interior boundaries not active

6.1.3. Boundary Settings

Boundary	3	4	2	1
Type	Dirichlet	Dirichlet	Neumann	Dirichlet
(R1)	-u	**0**	-u	**2*um*(1-(y/0.011)^2)-u**

6.1.4. Subdomain Settings

Subdomain 1

Source term ***(f)*** **mu/3/y*vx-rho*u*ux-(rho*v-mu/y)*uy-px+mu/3*vxy**

Conservative flux source term ***(tau)*** **{{-4/3*mu*ux;-mu*uy}}**

Subdomain initial value 1 u um

6.2. Application Mode: PDE, General Form (g2)

Application mode type: PDE, General Form

Application mode name: g2

6.2.1. Application Mode Properties

Property	**Value**
Default element type	Lagrange - Quadratic
Wave extension	Off
Weak constraints	Off

6.2.2. Variables

Dependent variables: v, v_t – **y– component of the velocity (m/s)**

Shape functions: shlag(2,'v')

Interior boundaries not active

6.2.3. Boundary Settings

Boundary	1,3	2	4
Type	Dirichlet	Neumann	Dirichlet
(R1)	-v	-v	**0**

6.2.4. Subdomain Settings

Subdomain 1

Source term *(f)* **-(rho*u*vx+(rho*v-2/3*mu/y)*vy+py-mu/3*uxyrho*g+2/3*mu/y*ux)**

Conservative flux source term *(tau)* **{{-mu*vx;-4/3*mu*vy}}**

6.3. Application Mode: PDE, General Form (g3)

Application mode type: PDE, General Form

Application mode name: g3

6.3.1. Application Mode Properties

Property	**Value**
Default element type	Lagrange - Quadratic
Wave extension	Off
Weak constraints	Off

6.3.2. Variables

Dependent variables: p, p_t – **pressure (Pa)**

Shape functions: shlag(1,'p')

Interior boundaries not active

6.3.3. Boundary Settings

Boundary	1-3	4
Type	Dirichlet	Dirichlet
(R1)	**0**	**po-p**

6.3.4. Subdomain Settings

Subdomain 1

Source term *(f)*	**C*(ux+vy+v/y)-rxno-rxno2-rxno3**
Conservative flux sourceterm *(tau)*	**{{0;0}}**

Subdomain initial value 1 p po

6.4. Application Mode: PDE, General Form (g4)

Application mode type: PDE, General Form

Application mode name: g4

6.4.1. Application Mode Properties

Property	**Value**
Default element type	Lagrange - Quadratic
Wave extension	Off
Weak constraints	Off

6.4.2. Variables

Dependent variables: co, co_t – **O-atom concentration (mol/m^3)**

Shape functions: shlag(2,'co')

Interior boundaries not active

6.4.3. Boundary Settings

Boundary	4	1	2	3
Type	Dirichlet	Dirchlet	Dirichlet	Neumann
(G1)	0	0	0	**-rso**
(R1)	**0**	**coi-co**	-co	-co

6.4.4. Subdomain Settings

Subdomain 1

Source term *(f)*	**D1*diff(co,y)/y-v*diff(co,y)-u*diff(co,x)+rxno**
Conservative flux source term *(tau)*	**{{-D1*cox;-D1*coy}}**

Subdomain initial value 1 co coi

6.5. Application Mode: PDE, General Form (g5)

Application mode type: PDE, General Form

Application mode name: g5

6.5.1. Application Mode Properties

Property	**Value**
Default element type	Lagrange - Quadratic
Wave extension	Off
Weak constraints	Off

6.5.2. Variables

Dependent variables: co3, co3_t – **O_3 Concentration (mol/m^3)**

Shape functions: shlag(2,'co3')

Interior boundaries not active

6.5.3. Boundary Settings

Boundary	1	4	2-3
Type	Dirichlet	Dirichlet	Neumann
(R1)	**co3i-co3**	**0**	-co3

6.5.4. Subdomain Settings

Subdomain	1
Source term *(f)*	**D2*diff(co3,y)/y-v*diff(co3,y)-u*diff(co3,x)+rxno3**
Conservative flux source term *(tau)*	**{{-D2*co3x;-D2*co3y}}**
Subdomain initial value	1
co3	co3i

6.6. Application Mode: PDE, General Form (g6)

Application mode type: PDE, General Form

Application mode name: g6

6.6.1. Application Mode Properties

Property	**Value**
Default element type	Lagrange - Quadratic
Wave extension	Off
Weak constraints	Off

6.6.2. Variables

Dependent variables: car, car_t – **Ar concentration (mol/m^3)**

Shape functions: shlag(2,'car')

Interior boundaries not active

6.6.3. Boundary Settings

Boundary	4	1	2-3
Type	Dirichlet	Dirichlet	Neumann
(R1)	**0**	**cari-car**	-car

6.6.4. Subdomain Settings

Subdomain	1
Source term *(f)*	**D2*diff(car,y)/y-v*diff(car,y)-u*diff(car,x)**
Conservative flux source term *(tau)*	**{{-D2*carx;-D2*cary}}**
Subdomain initial value	1
car	cari

7. Integration Coupling Variables

7.1. Geom1

7.1.1. Source Subdomain: 1

Name	**Value**
Variable name	co3a
Expression	co3
Order	4
Global	Yes

8. Functions

8.1. Interpolation Function: k2ar – **Rate const. for rxn (2)**

Interpolation method: Piecewise Cubic

Data source type: Table

x	**f(x)**
200	572.56
300	199.52
400	94.44
500	77.85
600	52.46
700	38.64

9. Solver Settings

Solver Stationary

Solution form Automatic

Symmetric Off

Adaption Off

9.1. Direct (UMFPACK)

Solver type: Linear system solver

Parameter	**Value**
Pivot threshold	0.1
Memory allocation factor	0.7

9.2. Stationary

Parameter	**Value**
Linearity	Nonlinear
Relative tolerance	1.0E-6
Maximum number of iterations	25
Manual tuning of damping parameters	Off
Highly nonlinear problem	On
Initial damping factor	1.0E-4
Minimum damping factor	1.0E-8
Restriction for step size update	10.0

Model II. Discharge ON, Furnace OFF condition

1. Table of Contents

2. Model description

This model was developed for a non-isothermal reactive flow of 2300 sccm of 87% O_2 – 13% Ar, at an outlet pressure of 431.3 Pa, 80% of maximum discharge power, and with furnace off. Details of the model are as follows:

Inputs:
1. Entrance velocity (profile) (m/s)
2. Outlet Pressure (Pa)
3. Linear temperature (K) profile at the entrance varying between the measured value at the centerline and 345 K at the wall
4. Empirical temperature profile at the entrance and at the wall (K)
5. Concentration profile at the entrance (of various species) - function of the entrance temperature profile and the measured concentration at the centerline (mol/m^3)
6. Rate constants suggested in the literature for various bulk O-atom recombination reactions
7. Surface recombination coefficient for the heterogeneous recombination of O atoms at the wall

Outputs:
1. Concentration profiles of various species in the reactor
2. Temperature profile in the reactor

The model consists of following equations:
1. Momentum Balance to solve for velocity in the x (u) and y (v) direction and pressure (p) represented by equations g, g2, and g3, respectively
2. Energy Balance to solve for temperature (T) represented by equation g4
3. Individual mass balances to solve for concentrations of O-atoms (co), O_3 (co3), and argon (car) represented by equations g5, g6, and g7, respectively.

3. Constants

Name	Expression	Description
Mo2	0.032	kg/mol – Mol.wt of O_2
Mo	0.016	kg/mol – Mol. Wt of O
Mar	0.040	kg/mol – Mol. Wt of O3
Tco2	154.6	K – Critical T of O_2
Pco2	5040000	Pa – Critical P of O_2
Tco	154.3	K – Critical T of O
Pco	4970000	Pa – Critical P of O
no	6.023e26	molecules/mol – Avogadro's Number
R	8.314	J/(mol.K) – Universal Gas Constant
Tcar	150.8	K – Critical T of Ar
Pcar	4870000	Pa – Critical p of Ar
Mo3	0.048	kg/mol – Mol.wt of O_3
Tco3	260.95	K – Critical T of O_3
Pco3	5573000	Pa – Critical P of O_3
e_k	(124*113)^0.5	Constant used in the calculation of D2
s_ab	(3.433+3.418)/2	Constant used in the calculation of D2
mab	2/((1/32)+(1/40))	Constant used in the calculation of D2
co3i	1e-5	mol/m^3 – O_3 concentration at the inlet
po	431.3	Pa - Outlet Pressure
um	24.5	m/s – Mean velocity at the inlet
g	9.8	m/s^2 – Acceleration due to gravity
gamma	1e-4	Surface recombination coefficient
T	300 K	Isothermal temperature of the flow
Do	0.365e-4	Constant used for calculating D1
ko	0.0264	W/m/K - Thermal conductivity of O
Cpo	920*Mo	J/mol/K – Heat capacity of O
Cpo3	817*Mo3	J/mol/K – Heat capacity of O_3
Cpar	20.8	J/mol/K – Heat capacity of Ar
Tent	560	K – Centerline T at PMT2
pent	459	Pa – Pressure at the inlet
noi	5.4e15	O-atom number density at the inlet
Twin	345	K – Wall temperature at PMT2
xoi	noi/6.023e23*1e6/(pent/R/Tent)	mole fraction of O at the inlet

4. Expressions

Name	Expression	Unit
Tin	(-2515*y^2 - 10.601*y + 1)*Tent	K – T profile at the entrance calc. as described in Chapter V, case III
coi	xoi*p/R/Tin	mol/m^3 – O-atom conc. at the inlet
xo	co/C	mole fraction of O
co2	C-car-co3-co	mol/m^3 – O_2 concentration
xo3	co3/C	mole fraction of O

xar	1-xo-xo3-xo2	mole fraction of Ar
M	xo*Mo+xo2*Mo2+xo3*Mo3+xar*Mar	kg/mol – Mol.wt of the gas mixture
Pcm	xo*Pco+xo2*Pco2+xar*Pcar+xo3*Pco3	Pa – Critical P of the gas mixture
Tcm	xo*Tco+xo2*Tco2+xar*Tcar+xo3*Tco3	K – Critical T of the gas mixture
evis	(8314*Tcm*no^2/(M*1000)^3/Pcm^4)^(1/6)	Used in Viscosity calculation
te	T/Tcm	Used in Viscosity calculation
ne	0.018+0.807*te^0.618-0.357*exp(-0.449*te)+0.34*exp(-4.058*te)	Used in Viscosity calculation
rho	p*M/R/T	kg/m^3 – Density of gas mix.
mu	ne/evis	Pa.s – Viscosity of the gas mix.
Cpo2	(3.63-1.794e-3*T+0.658e-5*T^2-0.601e-8*T^3+0.179e-11*T^4)*R	J/(mol.K) – Heat capacity of O_2
Cpm	xo2*Cpo2+xo*Cpo+xar*Cpar+xo3*Cpo3	J/(mol.K) – Heat capacity of the gas mixture
ko2	-(3.27E-4-9.732E-12*T^3-9.966E-5*T+3.743E-8*T^2)	W/(m.K) – Thermal conductivity of O_2
kar	0.002714+5.54E-5*T-2.178E-8*T^2+5.528E-12*T^3	W/(m.K) – Thermal conductivity of Ar
k	xo2*ko2+xo*ko+xar*ka	W/(m.K) – Thermal conductivity of the gas mixture
D1	Do*760/(25/3333*p)*(T/298)^1.64	m^2/s – Diff. coeff. of O in O_2
C	p/R/T	mol/m^3 – Total conc.
Ts	T/e_k	Used in calculation of D2
omeg	1.06036/Ts^0.1561+0.193/exp(0.47635*Ts)+1.03587/exp(1.52996*Ts)+1.76474/exp(3.89411*Ts)	Used in calculation of D2
D2	2.66E-7*T^1.5/(1.0E-5*p)/mab^0.5/s_ab^2/omeg	m^2/s – Diff. Coeff of Ar in O_2
k1ar	5.2e-35*exp(900/T)*(6.023e23)^2/(1e6)^2	Rate const. For rxn (1) m^6/mol^2/s
k1o	k1ar	m^6/mol^2/s
k1o2	k1ar	m^6/mol^2/s
k1o3	k1ar	m^6/mol^2/s
k2o2	1.5*k2	m^6/mol^2/s – Rate const. for rxn (2)
k2o	k2o2	m^6/mol^2/s
k2o3	k2o2	m^6/mol^2/s
k4o3	7.16e-10*exp(-11180/T)*6.023e17	m^3/mol/s – Rate const. for rxn(4)
k4ar	0.25*k4o3	m^3/mol/s
k4o2	0.5*k4o3	m^3/mol/s
k4o	k4o2	m^3/mol/s

rxno	-2*co^2*(k1o*co+k1o2*co2+k1o3*co3+k1ar*car)-co*co2*(k2o*co+k2o2*co2+k2o3*co3+k2ar(T)*car)-co*co3*k3+co3*(k4o*co+k4o2*co2+k4o3*co3+k4ar*car)	mol/m^3/s – Rate of formation of O
rxno2	co^2*(k1o*co+k1o2*co2+k1o3*co3+k1ar*car)-co*co2*(k2o*co+k2o2*co2+k2o3*co3+k2ar(T)*car)+2*co*co3*k3+co3*(k4o*co+k4o2*co2+k4o3*co3+k4ar*car)	mol/m^3/s – Rate of formation of O_2
rxno3	co*co2*(k2o*co+k2o2*co2+k2o3*co3+k2ar(T)*car)-co*co3*k3-co3*(k4o*co+k4o2*co2+k4o3*co3+k4ar*car)	mol/m^3/s – Rate of formation of O_3
k2	k2ar(T)	Rate const. for rxn (2) as a function of T
k3	(8e-12*exp(-2060/T))*6.023e17	m^3/mol/s – Rate const. for rxn (3)
rso	(gamma*36.39*T^0.5*co/4)	m^2/mol/s - Rate of surface rxn
Narx	car*u-D2*(carx+cary)	mol/(m^2.s) – molar flux of Ar in x direction
Nary	car*v-D2*(carx+cary)	mol/(m^2.s) – molar flux of Ar in y direction
Nox	co*u-D1*(cox+coy)	mol/(m^2.s) – molar flux of O in x direction
Noy	co*v-D1*(cox+coy)	mol/(m^2.s) – molar flux of O in y direction
Ho	-Cpo*(298-T)	J/mol – Enthalpy of O
Har	-Cpar*(298-T)	J/mol – Enthalpy of Ar
NoxHo	Nox*Ho	J/(m^2.s) – Heat flux of O in x-direction
NoyHo	Noy*Ho	J/(m^2.s) – Heat flux of O in y-direction
NarxHar	Narx*Har	J/(m^2.s) – Heat flux of Ar in x-direction
NaryHar	Nary*Har	J/(m^2.s) – Heat flux of Ar in y-direction
No3x	co3*u-D2*(co3x+co3y)	mol/(m^2.s) – molar flux of O_3 in x-direction
No3y	co3*v-D2*(co3x+co3y)	mol/(m^2.s) – molar flux of O_3 in y-direction
Ho3	-Cpo3*(298-T)	J/mol – Enthalpy of O_3
No3xHo3	No3x*Ho3	J/(m^2.s) – Heat flux of O_3 in x-direction
No3yHo3	No3y*Ho3	J/(m^2.s) – Heat flux of O_3 in y-direction

Ho2	-Cpo2*(298-T)	J/mol – Enthalpy of O_3
No2x	C*u-Narx-Nox-No3x	mol/(m^2.s) – molar flux of O_2 in the x-direction
No2y	C*v-Nary-Noy-No3y	mol/(m^2.s) – molar flux of O_2 in the y-direction
No2xHo2	No2x*Ho2	J/(m^2.s) – Heat flux of O_2 in x-direction
No2yHo2	No2y*Ho2	J/(m^2.s) – Heat flux of O_2 in y-direction
xo2	co2/C	mole fraction of O_2
xar	1-xo-xo3-xo2	mole fraction of Ar
cari	0.13*pent/R/Tin	mol/m^3 - Conc. of Ar at inlet
co3avg	co3a/(0.011*0.76)	mol/m^3 - Avg. O_3 conc in the reactor
Tavg	Ta/(0.011*0.665)	K – Average T in the reactor
um	5.65e-5/33.04*1000*(82.1578*(Tent+345)/2/(((pent))*(0.0000099))/(3.14*1.1^2)/100)	m/s - mean velocity at the entrance

5. Geometry

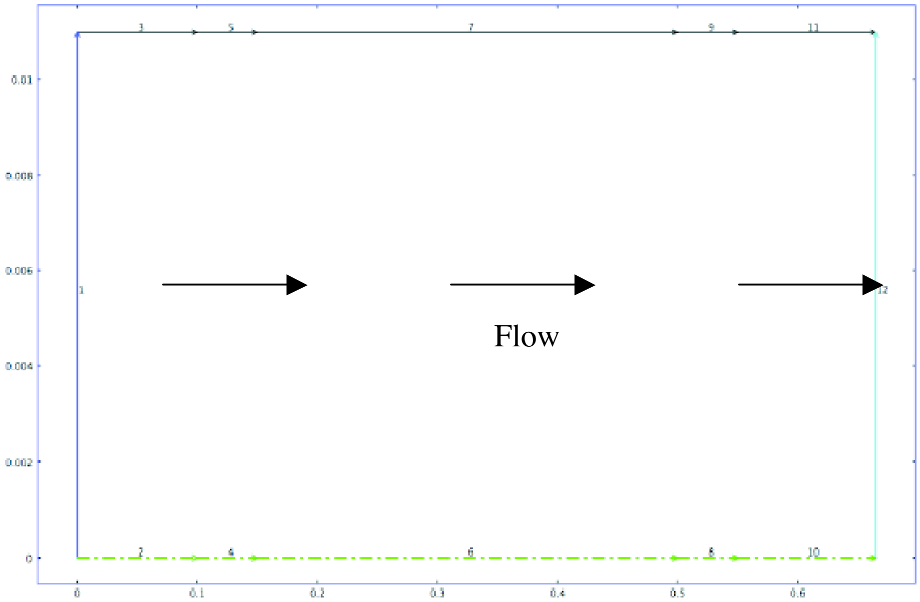

5.2. Mesh

5.2.1. Mesh Statistics

Number of degrees of freedom	10455
Number of mesh points	465
Number of elements	368

Triangular	0
Quadrilateral	368
Number of boundary elements	192
Number of vertex elements	12
Minimum element quality	0.473
Element area ratio	0.286

6.1. Application Mode: PDE, General Form (g)

Application mode type: PDE, General Form

Application mode name: g

6.1.1. Application Mode Properties

Property	**Value**
Default element type	Lagrange - Quadratic
Wave extension	Off
Weak constraints	Off

6.1.2. Variables

Dependent variables: u, u_t – **x- component of the velocity (m/s)**

Shape functions: shlag(2,'u')

Interior boundaries not active

6.1.3. Boundary Settings

Boundary	3	4	2	1
Type	Dirichlet	Dirichlet	Neumann	Dirichlet
(R1)	-u	**0**	-u	**2*um*(1-(y/0.011)^2)-u**

6.1.4. Subdomain Settings

Subdomain 1

Source term *(f)* **mu/3/y*vx-rho*u*ux-(rho*v-mu/y)*uy-px+ mu/3*vxy**

Conservative flux source term *(tau)* **{{-4/3*mu*ux;-mu*uy}}**

Subdomain initial value 1 u um

6.2. Application Mode: PDE, General Form (g2)

Application mode type: PDE, General Form

Application mode name: g2

6.2.1. Application Mode Properties

Property	**Value**
Default element type	Lagrange - Quadratic
Wave extension	Off
Weak constraints	Off

6.2.2. Variables

Dependent variables: v, v_t – **y – component of the velocity (m/s)**

Shape functions: shlag(2,'v')

Interior boundaries not active

6.2.3. Boundary Settings

Boundary	1,3	2	4
Type	Dirichlet	Neumann	Dirichlet

(R1)	-v	-v	**0**

6.2.4. Subdomain Settings

Subdomain	1
Source term *(f)*	**-(rho*u*vx+(rho*v-2/3*mu/y)*vy+py-mu/3*uxyrho*g+2/3*mu/y*ux)**
Conservative flux source term *(tau)*	**{{-mu*vx;-4/3*mu*vy}}**

6.3. Application Mode: PDE, General Form (g3)

Application mode type: PDE, General Form

Application mode name: g3

6.3.1. Application Mode Properties

Property	**Value**
Default element type	Lagrange - Quadratic
Wave extension	Off
Weak constraints	Off

6.3.2. Variables

Dependent variables: p, p_t – **pressure (Pa)**

Shape functions: shlag(1,'p')

Interior boundaries not active

6.3.3. Boundary Settings

Boundary	1-3	4
Type	Dirichlet	Dirichlet
(R1)	**0**	**po-p**

6.3.4. Subdomain Settings

Subdomain	1
Source term *(f)*	**C*(ux+vy+v/y)-rxno-rxno2-rxno3**
Conservative flux sourceterm *(tau)*	**{{0;0}}**

Subdomain initial value 1 p po

6.4. Application Mode: PDE, General Form (g4)

Application mode type: PDE, General Form

Application mode name: g4

6.4.1. Application Mode Properties

Property Value

Default element type Lagrange - Quadratic

Wave extension Off

Weak constraints Off

6.4.2. Variables

Dependent variables: T, T_t – **Temperature in K**

Shape functions: shlag(2,'T')

Interior boundaries not active

6.4.3. Boundary Settings

Boundary	12	1	2, 4, 6, 8, 10
Type	Dirichlet	Dirichlet	Neumann

(R1)	**0**	**Tin-T**	-T

Boundary	3, 5, 7, 9, 11
Type	Dirichlet
(R1)	**Tw(x)-T**

6.4.4. Subdomain Settings

Subdomain	1
Source term *(f)*	**k/y*Ty-diff(No2xHo2,x)-diff(No2yHo2,y)-diff(NarxHar,x)-diff(NaryHar,y)-No2yHo2/y-NaryHar/y-diff(NoxHo,x)-diff(NoyHo,y)-diff(No3xHo3,x)-diff(No3yHo3,y)-NoyHo/y-No3yHo3/y+u*px+v*py-mu*(2*(ux^2+vy^2)+(vx+uy)^2-2/3*(ux+vy)^2)**
Conservative flux source term *(tau)*	**{{-k*Tx;-k*Ty}}**
Subdomain initial value	1
T	500

6.5. Application Mode: PDE, General Form (g5)

Application mode type: PDE, General Form

Application mode name: g5

6.5.1. Application Mode Properties

Property	**Value**
Default element type	Lagrange - Quadratic
Wave extension	Off
Weak constraints	Off

6.5.2. Variables

Dependent variables: co, co_t – **O-atom concentration (mol/m^3)**

Shape functions: shlag(2,'co')

Interior boundaries not active

6.5.3. Boundary Settings

Boundary	4	1	2	3
Type	Dirichlet	Dirchlet	Dirichlet	Neumann
(G1)	0	0	0	**-rso**
(R1)	**0**	**coi-co**	-co	-co

6.5.4. Subdomain Settings

Subdomain	1
Source term *(f)*	**D1*diff(co,y)/y-v*diff(co,y)-u*diff(co,x)+rxno**
Conservative flux source term *(tau)*	**{{-D1*cox;-D1*coy}}**
Subdomain initial value	1
co	coi

6.6. Application Mode: PDE, General Form (g6)

Application mode type: PDE, General Form

Application mode name: g6

6.6.1. Application Mode Properties

Property	**Value**
Default element type	Lagrange - Quadratic
Wave extension	Off
Weak constraints	Off

6.6.2. Variables

Dependent variables: co3, co3_t – **O_3 Concentration (mol/m^3)**

Shape functions: shlag(2,'co3')

Interior boundaries not active

6.6.3. Boundary Settings

Boundary	1	4	2-3
Type	Dirichlet	Dirichlet	Neumann
(R1)	**co3i-co3**	**0**	-co3

6.6.4. Subdomain Settings

Subdomain	1
Source term *(f)*	**D2*diff(co3,y)/y-v*diff(co3,y)-u*diff(co3,x)+rxno3**
Conservative flux source term *(tau)*	**{{-D2*co3x;-D2*co3y}}**

Subdomain initial value 1 co3 co3i

6.7. Application Mode: PDE, General Form (g7)

Application mode type: PDE, General Form

Application mode name: g7

6.7.1. Application Mode Properties

Property	**Value**
Default element type	Lagrange - Quadratic
Wave extension	Off
Weak constraints	Off

6.7.2. Variables

Dependent variables: car, car_t – **Ar concentration (mol/m^3)**

Shape functions: shlag(2,'car')

Interior boundaries not active

6.7.3. Boundary Settings

Boundary	4	1	2-3
Type	Dirichlet	Dirichlet	Neumann
(R1)	**0**	**cari-car**	-car

6.7.4. Subdomain Settings

Subdomain	1
Source term *(f)*	**D2*diff(car,y)/y-v*diff(car,y)-u*diff(car,x)**
Conservative flux source term *(tau)*	**{{-D2*carx;-D2*cary}}**

Subdomain initial value 1 car cari

7. Integration Coupling Variables

7.1 Source Subdomain: 1

Name Value

Variable name	co3a
Expression	co3
Order	4
Global	Yes

7.2 Source Subdomain: 1

Name	**Value**
Variable name	Ta
Expression	T
Order	4
Global	Yes

8. Interpolation Functions

8.1. Interpolation Function: k2ar

Interpolation method: Piecewise Cubic

Data source type: Table

x	**f(x)**
200	572.56
250	320.52
300	199.52
350	133.64
400	94.44
450	99.65
500	77.85
550	63.03
600	52.46
650	44.62
700	38.64

8.2. Interpolation Function: Tw

Interpolation method: Piecewise Cubic

Data source type: Table

x	**f(x)**
0	345
0.2	320
0.43	312
0.66	305

9. Solver Settings

Solver Stationary

Solution form Automatic

Symmetric Off

Adaption Off

9.1. Direct (UMFPACK)

Solver type: Linear system solver

Parameter	**Value**
Pivot threshold	0.1

Memory allocation factor 0.7

9.2. Stationary

Parameter	**Value**
Linearity	Nonlinear
Relative tolerance	1.0E-6
Maximum number of iterations	25
Manual tuning of damping parameters	Off
Highly nonlinear problem	On
Initial damping factor	1.0E-4
Minimum damping factor	1.0E-8
Restriction for step size update	10.0

Model III. Discharge ON, Furnace ON (1323 K)

1. Table of Contents

2. Model description

This model was developed for a non-isothermal reactive flow of 2300 sccm of 87% O_2 – 13% Ar, at an outlet pressure of 431.3 Pa, 80% of maximum discharge power, and with furnace maintained at 1323 K. Some details of the model are as follows:

Inputs:
1. Entrance velocity (profile) (m/s)
2. Outlet Pressure (Pa)
3. Linear temperature (K) profile at the entrance varying between the measured value at the centerline and 345 K at the wall
4. Empirical temperature profile at the entrance and at the wall (K)
5. Concentration profile at the entrance (of various species) - function of the entrance temperature profile and the measured concentration at the centerline (mol/m^3)
6. Rate constants suggested in the literature for various bulk O-atom recombination reactions
7. Surface recombination coefficient for the heterogeneous recombination of O atoms at the wall

Outputs:
1. Concentration profiles of various species in the reactor
2. Temperature profile in the reactor

The model consists of following equations:
1. Momentum Balance to solve for velocity in the x (u) and y (v) direction and pressure (p) represented by equations g, g2, and g3, respectively
2. Energy Balance to solve for temperature (T) represented by equation g4
3. Individual mass balances to solve for concentrations of O-atoms (co), O_3 (co3), and argon (car) represented by equations g5, g6, and g7, respectively.

3. Constants

Name	Expression	Description
Mo2	0.032	kg/mol – Mol.wt of O_2
Mo	0.016	kg/mol – Mol. Wt of O
Mar	0.040	kg/mol – Mol. Wt of O3
Tco2	154.6	K – Critical T of O_2
Pco2	5040000	Pa – Critical P of O_2
Tco	154.3	K – Critical T of O
Pco	4970000	Pa – Critical P of O
no	6.023e26	molecules/mol – Avogadro's Number
R	8.314	J/(mol.K) – Universal Gas Constant
Tcar	150.8	K – Critical T of Ar
Pcar	4870000	Pa – Critical p of Ar
Mo3	0.048	kg/mol – Mol.wt of O_3
Tco3	260.95	K – Critical T of O_3
Pco3	5573000	Pa – Critical P of O_3
e_k	(124*113)^0.5	Constant used in the calculation of D2
s_ab	(3.433+3.418)/2	Constant used in the calculation of D2
mab	2/((1/32)+(1/40))	Constant used in the calculation of D2
co3i	1e-5	mol/m^3 – O_3 concentration at the inlet
po	431.3	Pa - Outlet Pressure
um	24.5	m/s – Mean velocity at the inlet
g	9.8	m/s^2 – Acceleration due to gravity
gamma	1e-4	Surface recombination coefficient
T	300 K	Isothermal temperature of the flow
Do	0.365e-4	Constant used for calculating D1
ko	0.0264	W/m/K - Thermal conductivity of O
Cpo	920*Mo	J/mol/K – Heat capacity of O
Cpo3	817*Mo3	J/mol/K – Heat capacity of O_3
Cpar	20.8	J/mol/K – Heat capacity of Ar
Tent	560	K – Centerline T at PMT2
pent	568	Pa – Pressure at the inlet
Twin	345	K – Wall temperature at PMT2
xoi	0.067	mole fraction of O at the inlet
Twout	380	K
Tf	1323	K

4. Expressions

Name	Expression	Unit
Tin	(-2515*y^2 - 10.601*y + 1)*Tent	K – T profile at the entrance calc. as described in Chapter V, case III
coi	xoi*p/R/Tin	mol/m^3 – O-atom conc. at the inlet
xo	co/C	mole fraction of O
co2	C-car-co3-co	mol/m^3 – O_2 concentration

xo3	co3/C	mole fraction of O
xar	1-xo-xo3-xo2	mole fraction of Ar
M	xo*Mo+xo2*Mo2+xo3*Mo3+xar*Mar	kg/mol – Mol.wt of the gas mixture
Pcm	xo*Pco+xo2*Pco2+xar*Pcar+xo3*Pco3	Pa – Critical P of the gas mixture
Tcm	xo*Tco+xo2*Tco2+xar*Tcar+xo3*Tco3	K – Critical T of the gas mixture
evis	(8314*Tcm*no^2/(M*1000)^3/Pcm^4)^(1/6)	Used in Viscosity calculation
te	T/Tcm	Used in Viscosity calculation
ne	0.018+0.807*te^0.618-0.357*exp(-0.449*te)+0.34*exp(-4.058*te)	Used in Viscosity calculation
rho	p*M/R/T	kg/m^3 – Density of gas mix.
mu	ne/evis	Pa.s – Viscosity of the gas mix.
Cpo2	(3.63-1.794e-3*T+0.658e-5*T^2-0.601e-8*T^3+0.179e-11*T^4)*R	J/(mol.K) – Heat capacity of O_2
Cpm	xo2*Cpo2+xo*Cpo+xar*Cpar+xo3*Cpo3	J/(mol.K) – Heat capacity of the gas mixture
ko2	-(3.27E-4-9.732E-12*T^3-9.966E-5*T+3.743E-8*T^2)	W/(m.K) – Thermal conductivity of O_2
kar	0.002714+5.54E-5*T-2.178E-8*T^2+5.528E-12*T^3	W/(m.K) – Thermal conductivity of Ar
k	xo2*ko2+xo*ko+xar*ka	W/(m.K) – Thermal conductivity of the gas mixture
D1	Do*760/(25/3333*p)*(T/298)^1.64	m^2/s – Diff. coeff. of O in O_2
C	p/R/T	mol/m^3 – Total conc.
Ts	T/e_k	Used in calculation of D2
omeg	1.06036/Ts^0.1561+0.193/exp(0.47635*Ts)+1.03587/exp(1.52996*Ts)+1.76474/exp(3.89411*Ts)	Used in calculation of D2
D2	2.66E-7*T^1.5/(1.0E-5*p)/mab^0.5/s_ab^2/omeg	m^2/s – Diff. Coeff of Ar in O_2
k1ar	5.2e-35*exp(900/T)*(6.023e23)^2/(1e6)^2	Rate const. For rxn (1) m^6/mol^2/s
k1o	k1ar	m^6/mol^2/s
k1o2	k1ar	m^6/mol^2/s
k1o3	k1ar	m^6/mol^2/s
k2o2	1.5*k2	m^6/mol^2/s – Rate const. for rxn (2)
k2o	k2o2	m^6/mol^2/s
k2o3	k2o2	m^6/mol^2/s
k4o3	7.16e-10*exp(-11180/T)*6.023e17	m^3/mol/s – Rate const. for rxn(4)
k4ar	0.25*k4o3	m^3/mol/s
k4o2	0.5*k4o3	m^3/mol/s

k4o	k4o2	m^3/mol/s
rxno	-2*co^2*(k1o*co+k1o2*co2+k1o3*co3+k1ar*car)-co*co2*(k2o*co+k2o2*co2+k2o3*co3+k2ar(T)*car)-co*co3*k3+co3*(k4o*co+k4o2*co2+k4o3*co3+k4ar*car)	mol/m^3/s – Rate of formation of O
rxno2	co^2*(k1o*co+k1o2*co2+k1o3*co3+k1ar*car)-co*co2*(k2o*co+k2o2*co2+k2o3*co3+k2ar(T)*car)+2*co*co3*k3+co3*(k4o*co+k4o2*co2+k4o3*co3+k4ar*car)	mol/m^3/s – Rate of formation of O_2
rxno3	co*co2*(k2o*co+k2o2*co2+k2o3*co3+k2ar(T)*car)-co*co3*k3-co3*(k4o*co+k4o2*co2+k4o3*co3+k4ar*car)	mol/m^3/s – Rate of formation of O_3
k2	k2ar(T)	Rate const. for rxn (2) as a function of T
k3	(8e-12*exp(-2060/T))*6.023e17	m^3/mol/s – Rate const. for rxn (3)
rso	(gamma*36.39*T^0.5*co/4)	m^2/mol/s - Rate of surface rxn
Narx	car*u-D2*(carx+cary)	mol/(m^2.s) – molar flux of Ar in x direction
Nary	car*v-D2*(carx+cary)	mol/(m^2.s) – molar flux of Ar in y direction
Nox	co*u-D1*(cox+coy)	mol/(m^2.s) – molar flux of O in x direction
Noy	co*v-D1*(cox+coy)	mol/(m^2.s) – molar flux of O in y direction
Ho	-Cpo*(298-T)	J/mol – Enthalpy of O
Har	-Cpar*(298-T)	J/mol – Enthalpy of Ar
NoxHo	Nox*Ho	J/(m^2.s) – Heat flux of O in x-direction
NoyHo	Noy*Ho	J/(m^2.s) – Heat flux of O in y-direction
NarxHar	Narx*Har	J/(m^2.s) – Heat flux of Ar in x-direction
NaryHar	Nary*Har	J/(m^2.s) – Heat flux of Ar in y-direction
No3x	co3*u-D2*(co3x+co3y)	mol/(m^2.s) – molar flux of O_3 in x-direction
No3y	co3*v-D2*(co3x+co3y)	mol/(m^2.s) – molar flux of O_3 in y-direction
Ho3	-Cpo3*(298-T)	J/mol – Enthalpy of O_3
No3xHo3	No3x*Ho3	J/(m^2.s) – Heat flux of O_3 in x-direction
No3yHo3	No3y*Ho3	J/(m^2.s) – Heat flux of O_3 in

		y-direction
Ho2	-Cpo2*(298-T)	J/mol – Enthalpy of O_3
No2x	C*u-Narx-Nox-No3x	mol/(m^2.s) – molar flux of O_2 in the x-direction
No2y	C*v-Nary-Noy-No3y	mol/(m^2.s) – molar flux of O_2 in the y-direction
No2xHo2	No2x*Ho2	J/(m^2.s) – Heat flux of O_2 in x-direction
No2yHo2	No2y*Ho2	J/(m^2.s) – Heat flux of O_2 in y-direction
xo2	co2/C	mole fraction of O_2
xar	1-xo-xo3-xo2	mole fraction of Ar
cari	0.13*pent/R/Tin	mol/m^3 - Conc. of Ar at inlet
co3avg	co3a/(0.011*0.76)	mol/m^3 - Avg. O_3 conc in the reactor
Tavg	Ta/(0.011*0.665)	K – Average T in the reactor
um	5.65e-5/33.04*1000*(82.1578*(Tent+345)/2/(((pent))*(0.0000099))/(3.14*1.1^2)/100)	m/s - mean velocity at the entrance

5. Geometry

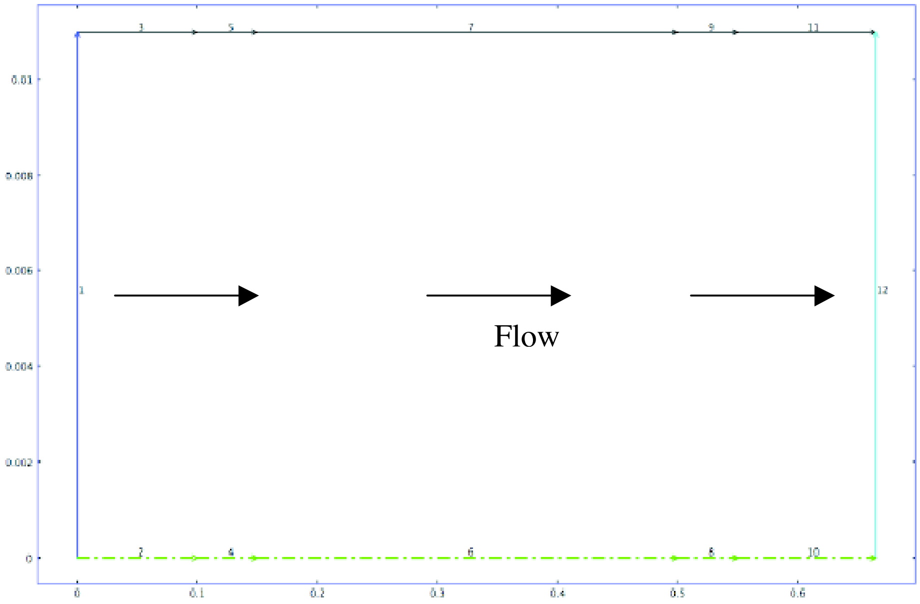

5.2. Mesh

5.2.1. Mesh Statistics

Number of degrees of freedom	10455
Number of mesh points	465
Number of elements	368
Triangular	0

Quadrilateral	368
Number of boundary elements	192
Number of vertex elements	12
Minimum element quality	0.473
Element area ratio	0.286

6.1. Application Mode: PDE, General Form (g)

Application mode type: PDE, General Form

Application mode name: g

6.1.1. Application Mode Properties

Property	**Value**
Default element type	Lagrange - Quadratic
Wave extension	Off
Weak constraints	Off

6.1.2. Variables

Dependent variables: u, u_t – **x- component of the velocity (m/s)**

Shape functions: shlag(2,'u')

Interior boundaries not active

6.1.3. Boundary Settings

Boundary	3	4	2	1
Type	Dirichlet	Dirichlet	Neumann	Dirichlet
(R1)	-u	**0**	-u	**2*um*(1-(y/0.011)^2)-u**

6.1.4. Subdomain Settings

Subdomain 1

Source term *(f)* **mu/3/y*vx-rho*u*ux-(rho*v-mu/y)*uy-px+ mu/3*vxy**

Conservative flux source term *(tau)* **{{-4/3*mu*ux;-mu*uy}}**

Subdomain initial value 1 u um

6.2. Application Mode: PDE, General Form (g2)

Application mode type: PDE, General Form

Application mode name: g2

6.2.1. Application Mode Properties

Property	**Value**
Default element type	Lagrange - Quadratic
Wave extension	Off
Weak constraints	Off

6.2.2. Variables

Dependent variables: v, v_t – **y – component of the velocity (m/s)**

Shape functions: shlag(2,'v')

Interior boundaries not active

6.2.3. Boundary Settings

Boundary	1,3	2	4
Type	Dirichlet	Neumann	Dirichlet
(R1)	-v	-v	**0**

6.2.4. Subdomain Settings

Subdomain 1

Source term *(f)*	**-(rho*u*vx+(rho*v-2/3*mu/y)*vy+py-mu/ 3*uxyrho*g+2/3*mu/y*ux)**
Conservative flux source term *(tau)*	**{{-mu*vx;-4/3*mu*vy}}**

6.3. Application Mode: PDE, General Form (g3)

Application mode type: PDE, General Form

Application mode name: g3

6.3.1. Application Mode Properties

Property	**Value**
Default element type	Lagrange - Quadratic
Wave extension	Off
Weak constraints	Off

6.3.2. Variables

Dependent variables: p, p_t – **pressure (Pa)**

Shape functions: shlag(1,'p')

Interior boundaries not active

6.3.3. Boundary Settings

Boundary	1-3	4
Type	Dirichlet	Dirichlet
(R1)	**0**	**po-p**

6.3.4. Subdomain Settings

Subdomain 1

Source term *(f)*	**C*(ux+vy+v/y)-rxno-rxno2-rxno3**
Conservative flux sourceterm *(tau)*	**{{0;0}}**

Subdomain initial value 1 p po

6.4. Application Mode: PDE, General Form (g4)

Application mode type: PDE, General Form

Application mode name: g4

6.4.1. Application Mode Properties

Property	**Value**
Default element type	Lagrange - Quadratic
Wave extension	Off
Weak constraints	Off

6.4.2. Variables

Dependent variables: T, T_t – **Temperature in K**

Shape functions: shlag(2,'T')

Interior boundaries not active

6.4.3. Boundary Settings

Boundary	12	1	2, 4, 6, 8, 10
Type	Dirichlet	Dirichlet	Neumann

(R1)	**0**	**Tin-T**	-T

Boundary	11	3	5
Type	Dirichlet	Dirichlet	Dirichlet
(R1)	**Twout-T**	**Twin-T**	**(Twin+(Tf-Twin)/0.05 *(x-0.1))-T**

Boundary	7	9
Type	Dirichlet	Dirichlet
(R1)	**Tf-T**	**(Tf-(Tf-Twout)/0.05*(x-0.5))-T**

6.4.4. Subdomain Settings

Subdomain 1

Source term *(f)*	**k/y*Ty-diff(No2xHo2,x)-diff(No2yHo2,y)-diff (NarxHar,x)-diff(NaryHar,y)-No2yHo2/y-NaryHar/y-diff(NoxHo,x)-diff(NoyHo,y)-diff (No3xHo3,x)-diff(No3yHo3,y)-NoyHo/y-No3yHo3/y+u*px+v*py-mu*(2*(ux^2+vy^2)+ (vx+uy)^2-2/3*(ux+vy)^2)**
Conservative flux source term *(tau)*	**{{-k*Tx;-k*Ty}}**

Subdomain initial value 1 T 500

6.5. Application Mode: PDE, General Form (g5)

Application mode type: PDE, General Form

Application mode name: g5

6.5.1. Application Mode Properties

Property	**Value**
Default element type	Lagrange - Quadratic
Wave extension	Off
Weak constraints	Off

6.5.2. Variables

Dependent variables: co, co_t – **O-atom concentration (mol/m^3)**

Shape functions: shlag(2,'co')

Interior boundaries not active

6.5.3. Boundary Settings

Boundary	4	1	2	3
Type	Dirichlet	Dirchlet	Dirichlet	Neumann
(G1)	0	0	0	**-rso**
(R1)	**0**	**coi-co**	-co	-co

6.5.4. Subdomain Settings

Subdomain 1

Source term *(f)*	**D1*diff(co,y)/y-v*diff(co,y)-u*diff(co,x)+rxno**
Conservative flux source term *(tau)*	**{{-D1*cox;-D1*coy}}**

Subdomain initial value 1 co coi

6.6. Application Mode: PDE, General Form (g6)

Application mode type: PDE, General Form

Application mode name: g6

6.6.1. Application Mode Properties

Property	**Value**
Default element type	Lagrange - Quadratic
Wave extension	Off
Weak constraints	Off

6.6.2. Variables

Dependent variables: co3, co3_t – **O_3 Concentration (mol/m^3)**

Shape functions: shlag(2,'co3')

Interior boundaries not active

6.6.3. Boundary Settings

Boundary	1	4	2-3
Type	Dirichlet	Dirichlet	Neumann
(R1)	**co3i-co3**	**0**	-co3

6.6.4. Subdomain Settings

Subdomain 1

Source term *(f)*	**D2*diff(co3,y)/y-v*diff(co3,y)-u*diff(co3,x)+rxno3**
Conservative flux source term *(tau)*	**{{-D2*co3x;-D2*co3y}}**

Subdomain initial value 1 co3 co3i

6.7. Application Mode: PDE, General Form (g7)

Application mode type: PDE, General Form

Application mode name: g7

6.7.1. Application Mode Properties

Property	**Value**
Default element type	Lagrange - Quadratic
Wave extension	Off
Weak constraints	Off

6.7.2. Variables

Dependent variables: car, car_t – **Ar concentration (mol/m^3)**

Shape functions: shlag(2,'car')

Interior boundaries not active

6.7.3. Boundary Settings

Boundary	4	1	2-3
Type	Dirichlet	Dirichlet	Neumann
(R1)	**0**	**cari-car**	-car

6.7.4. Subdomain Settings

Subdomain 1

Source term *(f)*	**D2*diff(car,y)/y-v*diff(car,y)-u*diff(car,x)**
Conservative flux source term *(tau)*	**{{-D2*carx;-D2*cary}}**

Subdomain initial value 1 car cari

7. Integration Coupling Variables

7.1 Source Subdomain: 1

Name	**Value**
Variable name	co3a
Expression	co3
Order	4
Global	Yes

7.2 Source Subdomain: 1

Name	**Value**
Variable name	Ta
Expression	T
Order	4
Global	Yes

8. Interpolation Functions

8.1. Interpolation Function: k2ar

Interpolation method: Piecewise Cubic

Data source type: Table

x	**f(x)**
200	572.56
250	320.52
300	199.52
350	133.64
400	94.44
450	99.65
500	77.85
550	63.03
600	52.46
650	44.62
700	38.64

9. Solver Settings

Solver Stationary

Solution form Automatic

Symmetric Off

Adaption Off

9.1. Direct (UMFPACK)

Solver type: Linear system solver

Parameter	**Value**
Pivot threshold	0.1
Memory allocation factor	0.7

9.2. Stationary

Parameter	**Value**
Linearity	Nonlinear

Relative tolerance	1.0E-6
Maximum number of iterations	25
Manual tuning of damping parameters	Off
Highly nonlinear problem	On
Initial damping factor	1.0E-4
Minimum damping factor	1.0E-8
Restriction for step size update	10.0

Oxidation Model

The steady state oxidation model described in Chapter II (Equations 3 & 4) was solved using COMSOL MULTIPHYSICS®. The model was solved for various oxidation times using a time step of 10 seconds by importing the COMSOL model to Matlab by saving it as an 'mfile'.

The initial thickness of the oxide layer at time = 0, was assumed to be 1.93 nm (native oxide layer on the substrates used). This initial thickness was then used to calculate the increase in thickness after the first time step. The thickness calculated was then added to the thickness before that time step to calculate the new 'total thickness'. This geometry used for the next step was then updated to the 'total thickness' and the thickness calculated was then again added to the 'total thickness'. This procedure was used to calculate oxide thicknesses for various oxidation times.

The model was fitted to the data at fixed D_{o2}, K_{o2}, α_{o2}, and α_o to determine D_o and K_o. Model was fitting was carried out using the Optimization Toolbox in Matlab, which uses a trust-region method for non-linear least squares curve fitting. The procedure followed was to call the following function in the Matlab Command Window.

```
[FP]=lsqcurvefit(@F_ss_1050,para,xdata,ydata,lb)
```

where,

FP is the array of fitted parameters,

lsqcurvefit is the command used to perform the non-linear curv-fitting,

para is the array of parameters that will be varied for curve-fitting, xdata is the array of independent variables (oxidation times in our case),

ydata is the array of dependent variables (Oxide thicknesses in our case),

lb is the lower bound on the parameters to be varied (0 in our case), and

F_ss_1050 is the function that calculates the oxide thicknesses

The curve-fitting algorithm calls the function ‘F_ss_1050’ and provides ‘para’ and ‘xdata’ as inputs to it. The function ‘F_ss_1050’ uses these inputs to calculate the oxide thicknesses for various times using the procedure described above and returns the same back to the curve-fitting algorithm. The algorithm then calculates the summation of the squares of the differences between the calculated and measured values (array ‘ydata’). It then calculates the next guess and updates the array ‘para’. The algorithm then calls the function ‘F_ss_1050’ again and provides ‘xdata’ and the updated ‘para’ as the inputs. This procedure is continued until the summation of the squares is minimized.

The function used ‘F_ss_1050’ used to calculate oxide thicknesses at 1050 °C (1323 K) and 431.3 Pa is as shown below,

```
function F = F_ss_1050(para,xdata)

% COMSOL Multiphysics Model M-file
% Generated by COMSOL 3.3 (COMSOL 3.3.0.405, $Date: 2006/08/31 18:03:47 $)
guess=para
flclear fem
n=length(xdata);   % No. of data points
dt=10;             % Time step in seconds
t = xdata(n)/dt;    % No. of times the steady state model will be solved
time = 0;          % Initializing time
oxthk = 1.93e-9;   % Native oxide thickness

for i=1:t          % Start solving the steady state model

time = time + dt;  % Set the time for which the model needs to be solved
```

```
thk=oxthk;          % Set the thickness (of the oxide layer) for which
                    % the model was solved.

% COMSOL version
clear vrsn
vrsn.name = 'COMSOL 3.3';
vrsn.ext = '';
vrsn.major = 0;
vrsn.build = 405;
vrsn.rcs = '$Name:  $';
vrsn.date = '$Date: 2006/08/31 18:03:47 $';
fem.version = vrsn;

% Geometry
g1=solid1([0,oxthk]); % Add the thickness from last time step to the
                      % geometry

% Analyzed geometry
clear s
s.objs={g1};
s.name={'I1'};
s.tags={'g1'};

fem.draw=struct('s',s);
fem.geom=geomcsg(fem);



% Constants
fem.const = {'Do2','5e-13', ...    % Diffusivity of O2 in m^2/s
  'Do',para(1)*1e-11, ...          % Diffusivity of O in m^2/s
  'ko2','1e-5', ...                % Reactivity of O2 in m/s
  'ko',para(2)*1e-3, ...           % Reactivity of O in m/s
  'alphao2','0.002', ...           % Solubility of O2 in SiO2
  'alphao','1', ...                % Solubility of O in SiO2
  'cgaso','2.17e-3' ...            % Conc. of O in the bulk (mol/m^3)
  'cgaso2','0.04' ...              % Conc. of O2 in the bulk (mol/m^3)
  'cos','alphao*cgaso', ...        % Conc. of O at the oxide surface (mol/m^3)
  'co2s','alphao2*cgaso2'};        % Conc. of O2 at the oxide surface (mol/m^3)

% Initialize mesh
fem.mesh=meshinit(fem, ...
           'hmax',[], ...
           'hmaxfact',1, ...
           'hgrad',1.3, ...
```

```
              'xscale',1.0);

% Refine mesh
fem.mesh=meshrefine(fem, ...
               'mcase',0);

% Refine mesh
fem.mesh=meshrefine(fem, ...
               'mcase',0);

% Refine mesh
fem.mesh=meshrefine(fem, ...
               'mcase',0);

% Application mode 1 - Solving for co (O-atom concentration)
clear appl
appl.mode.class = 'FlPDEG';
appl.mode.type = 'cartesian';
appl.dim = {'co','co_t'};
appl.sdim = {'x','y','z'};
appl.name = 'g';
appl.shape = {'shlag(2,''co'')'};
appl.gporder = 4;
appl.cporder = 2;
appl.sshape = 2;
appl.border = 'off';
appl.assignsuffix = '_g';
clear prop
prop.elemdefault='Lag2';
prop.wave='off';
prop.frame='ref';
clear weakconstr
weakconstr.value = 'off';
weakconstr.dim = {'lm1','lm2'};
prop.weakconstr = weakconstr;
appl.prop = prop;
clear bnd
bnd.type = {'dir','neu'};
bnd.r = {'cos-co','-co'};
bnd.weak = 0;
bnd.dweak = 0;
bnd.constr = 0;
bnd.g = {0,'-ko*co'};
bnd.name = '';
bnd.ind = [1,2];
appl.bnd = bnd;
```

```
clear equ
equ.init = {{'cos';0}};
equ.shape = 1;
equ.dweak = 0;
equ.constr = 0;
equ.ea = 0;
equ.cporder = 1;
equ.da = 0;
equ.gporder = 1;
equ.weak = 0;
equ.f = '-k1*co^2+2*k2*co2';
equ.usage = 1;
equ.ga = '-Do*cox';
equ.dinit = 0;
equ.ind = [1];
equ.bnd.gporder = 1;
equ.bnd.weak = 0;
equ.bnd.ind = [1];
appl.equ = equ;
fem.appl{1} = appl;

% Application mode 2- Solving for co2 (O2 concentration)
clear appl
appl.mode.class = 'FlPDEG';
appl.mode.type = 'cartesian';
appl.dim = {'co2','co2_t'};
appl.sdim = {'x','y','z'};
appl.name = 'g2';
appl.shape = {'shlag(2,''co2'')'};
appl.gporder = 4;
appl.cporder = 2;
appl.sshape = 2;
appl.border = 'off';
appl.assignsuffix = '_g2';
clear prop
prop.elemdefault='Lag2';
prop.wave='off';
prop.frame='ref';
clear weakconstr
weakconstr.value = 'off';
weakconstr.dim = {'lm3','lm4'};
prop.weakconstr = weakconstr;
appl.prop = prop;
clear bnd
bnd.type = {'dir','neu'};
bnd.r = {'co2s-co2','-co2'};
```

```
bnd.weak = 0;
bnd.dweak = 0;
bnd.constr = 0;
bnd.g = {0,'-ko2*co2'};
bnd.name = '';
bnd.ind = [1,2];
appl.bnd = bnd;
clear equ
equ.init = {{'co2s';0}};
equ.shape = 1;
equ.dweak = 0;
equ.constr = 0;
equ.ea = 0;
equ.cporder = 1;
equ.da = 0;
equ.gporder = 1;
equ.weak = 0;
equ.f = '-k2*co2+0.5*k1*co^2';
equ.usage = 1;
equ.ga = '-Do2*co2x';
equ.dinit = 0;
equ.ind = [1];
equ.bnd.gporder = 1;
equ.bnd.weak = 0;
equ.bnd.ind = [1];
appl.equ = equ;
fem.appl{2} = appl;
fem.sdim = {'x'};
fem.frame = {'ref'};

% Simplify expressions
fem.simplify = 'on';
fem.border = 1;

% Scalar expressions
fem.expr = {};

% Global expressions
fem.globalexpr = {};

% Functions
clear fcns
fem.functions = {};

% Solution form
fem.solform = 'weak';
```

```
% Multiphysics
fem=multiphysics(fem);

% Extend mesh
fem.xmesh=meshextend(fem,'geoms',[1],'eqvars','on','cplbndeq','on','cplbndsh','off');

% Solve problem
fem.sol=femstatic(fem, ...
                'method','eliminate', ...
                'nullfun','auto', ...
                'blocksize',5000, ...
                'complexfun','off', ...
                'matherr','on', ...
                'solfile','off', ...
                'conjugate','off', ...
                'symmetric','auto', ...
                'solcomp',{'co','co2'}, ...
                'outcomp',{'co','co2'}, ...
                'rowscale','on', ...
                'ntol',1.0E-6, ...
                'maxiter',25, ...
                'nonlin','auto', ...
                'hnlin','off', ...
                'linsolver','umfpack', ...
                'thresh',0.1, ...
                'umfalloc',0.7, ...
                'uscale','auto', ...
                'mcase',0);

% Save current fem structure for restart purposes
fem0=fem;

Jo=postinterp(fem, '-Do*cox', [oxthk]);          % Calculate the flux of O at the
                                                 % Si/oxidde interface
Jo2=postinterp(fem, '-Do2*co2x', [oxthk]);        % Calculate the flux of O2 at
                                                  % the Si/oxidde interface

oxthk=(60.08/2.2e6)*(Jo2+Jo/2)*dt+thk;            % Calc thickness from the fluxes
oxtime(i)=time;
thkox(i)=oxthk;
end

% Compare the calculated and measured thicknesses at various times
thickness(1)=1.93e-9;
for j=2:n
```

```
    timeox=xdata(j)/dt;
    thickness(j)=thkox(timeox);
end
F = thickness*1e9

thkexp=[1.93 52.1 63.8 79.2 130.8];
sum=0;

for j=1:n
    sum=sum+(thickness(j)*1e9-thkexp(j))^2;
end
```

APPENDIX C

Reactor Characterization

Experiment RC1: Pressure measurements for an 87% O_2-13% Ar mixture at 300 K with the discharge *off*.

m (kg/s)	**$Pin_{meas.}$ (Pa)**	**$Pout_{meas.}$ (Pa)**	Calc. **$U_{mean\text{-}in.}$ (m/s)**	**Pin_{calc} (Pa)**	**Pin_{Calc} / $Pin_{meas.}$**	**$\Delta P_{meas.}$ (Pa)**	**ΔP_{calc} (Pa)**	**$\Delta P_{calc}/\Delta P_{meas.}$**
5.65×10^{-5}	315.44	277.31	35.5	314.67	0.99	38.13	37.35	0.98
2.82×10^{-5}	212.38	182.65	26.4	210.22	0.99	29.73	27.56	0.92
1.41×10^{-5}	147.58	126.12	19	145.91	0.99	21.46	19.78	0.92
5.65×10^{-5}	570.48	550.22	19.6	570.81	1	20.26	20.58	1.01
2.82×10^{-5}	337.57	319.44	16.6	336.74	0.99	18.13	17.29	0.95
1.41×10^{-5}	207.31	192.91	13.5	207.04	0.99	14.39	14.12	0.98
5.65×10^{-5}	1114.3	1103.9	10.1	1114.4	1	10.39	10.57	1.01
2.82×10^{-5}	688.61	679.94	8.13	688.37	0.99	8.66	8.42	0.97
1.41×10^{-5}	437.29	430.23	6.4	436.92	0.99	7.06	6.68	0.94

Experiment RC2: Pressure measurements for an 87% O_2-13% Ar mixture at 1323 K with the discharge *off*

m (kg/s)	**Pin$_{meas.}$ (Pa)**	**Pout$_{meas.}$ (Pa)**	Calc. **U$_{mean-in.}$ (m/s)**	**Pin$_{calc}$ (Pa)**	**Pin$_{Calc}$/ Pin$_{meas.}$**	**ΔP$_{meas.}$ (Pa)**	**ΔP$_{calc}$ (Pa)**	**ΔP$_{calc}$/ΔP$_{meas.}$**
5.65×10-^{5}	503.56	277.31	22.2	495.01	0.98	226.25	217.69	0.96
2.82×10-^{5}	345.04	183.05	16.2	342.96	0.99	161.99	159.91	0.99
1.41×10-^{5}	237.58	125.46	11.8	239.58	1.01	112.12	114.12	1.02
5.65×10-^{5}	691.01	551.95	16.2	683.5	0.99	139.06	131.54	0.95
2.82×10-^{5}	431.83	317.04	13	427.42	0.99	114.79	110.37	0.96
1.41×10-^{5}	279.97	191.85	10	278.51	0.99	88.13	86.66	0.98
5.65×10-^{5}	1179.50	1104.57	9.5	1174.95	0.99	74.93	70.37	0.94
2.82×10-^{5}	741.54	679.81	7.55	736.65	0.99	61.73	56.84	0.92
1.41×10-^{5}	476.63	428.63	5.88	473.36	0.99	47.99	44.73	0.93

Experiment RC3: Pressure measurements for a 5.65×10^{-5} kg/s (2300 sccm) 87% O_2-13% Ar mixture at various microwave powers and furnace *off*.

m (kg/s)	**Pin$_{meas.}$ (Pa)**	**Pout$_{meas.}$ (Pa)**	Calc. **U$_{mean-in.}$ (m/s)**	**Pin$_{calc}$ (Pa)**	**Pin$_{Calc}$/ Pin$_{meas.}$**	**ΔP$_{meas.}$ (Pa)**	**ΔP$_{calc}$ (Pa)**	**ΔP$_{calc}$/ ΔP$_{meas.}$**	**Tavg (K)**
99	456.46	430.9	39.258	457.84	1.0029	25.162	26.544	0.95	350.36
90	456.33	431.3	38.381	457.65	1.003	25.032	26.35	0.95	348.54
80	456.16	431.3	37.414	457.49	1.0029	24.998	26.328	0.95	344.58
70	455.71	431.17	36.362	456.99	1.0029	24.945	26.227	0.95	343.92
60	455.51	430.76	35.243	456.73	1.0028	24.879	26.096	0.95	341.29
50	455.27	430.63	34.025	456.47	1.0027	24.772	25.968	0.95	338.24
40	454.97	430.5	32.706	456.07	1.0026	24.739	25.839	0.96	335.03
30	456.21	430.23	31.297	457.55	1.0024	25.312	26.655	0.95	331.46

Experiment RC4: Pressure measurements for a 5.65×10^{-5} kg/s (2300 sccm) 87% O_2-13% Ar mixture at various microwave powers and furnace maintained at 1323 K.

m (kg/s)	**$Pin_{meas.}$ (Pa)**	**$Pout_{meas.}$ (Pa)**	Calc. **$U_{mean-in.}$ (m/s)**	**Pin_{calc} (Pa)**	**Pin_{Calc}/ $Pin_{meas.}$**	**$\Delta P_{meas.}$ (Pa)**	**ΔP_{calc} (Pa)**	**ΔP_{calc}/ $\Delta P_{meas.}$**	**Tavg (K)**
99	591.9	431.7	39.258	603.55	1.02	160.2	171.85	0.93	934
90	591.67	431.56	38.381	603.05	1.02	160.11	171.49	0.93	932
80	591.09	431.56	37.414	602.32	1.02	159.53	170.76	0.93	929
70	591.05	431.56	36.362	602.18	1.02	159.49	170.62	0.93	928
60	590.57	431.3	35.243	601.53	1.02	159.27	170.23	0.94	926
50	590.34	431.43	34.025	601.1	1.02	158.91	169.67	0.94	924
40	589.56	431.3	32.706	600.65	1.02	158.26	169.35	0.93	921
30	589.11	431.3	31.297	600.23	1.02	157.81	168.93	0.93	918

Experiment RC5: Comparison of measured and calculated ratios of centerline O-atom concentrations at the outlet to that of the inlet at various MWPs at a mass flow rate of 2300 sccm (87% O_2-13% Ar gas mixture) and an outlet pressure of 293.3 Pa.

% of max MWP	Measured $co_{(in)}$(/cm^3)	Measured $co_{(out)}$ (/cm^3)	Measured $c_{o(out)}/c_{o(in)}$	Calculated $c_{o(out)}/c_{o(in)}$	Calculated $c_{o(out)}/c_{o(in)}$ ($\gamma=3\times10^{-3}$)	Calculated $c_{o(out)}/c_{o(in)}$ (K2×50)
20	1.30×10^{15}	3.40×10^{14}	0.26154	0.95189	0.31171	0.16195
30	1.80×10^{15}	4.80×10^{14}	0.26667	1.0486	0.34888	0.18403
40	2.05×10^{15}	5.60×10^{14}	0.27317	1.1387	0.38475	0.20733
50	2.35×10^{15}	6.00×10^{14}	0.25532	1.2212	0.41860	0.22771
60	2.52×10^{15}	6.80×10^{14}	0.26984	1.3013	0.45118	0.24862
70	2.65×10^{15}	7.50×10^{14}	0.28302	1.3718	0.48132	0.26851
80	2.73×10^{15}	7.90×10^{14}	0.28938	1.4398	0.50994	0.28800
90	2.80×10^{15}	8.30×10^{14}	0.29643	1.5003	0.53605	0.30600
100	3.05×10^{15}	9.50×10^{14}	0.31148	1.5478	0.55715	0.31775

Experiment RC6: Comparison of measured and calculated ratios of centerline O-atom concentrations at the outlet to that of the inlet at a mass flow rate of 2300 sccm (87% O_2-13% Ar gas mixture) 80% MWP, at an outlet pressure of 431.3 Pa

Furnace Temperature (K)	Measured $c_{o(out)}/c_{o(in)}$	Calculated $c_{o(out)}/c_{o(in)}$
300	0.25	1.4096
325	0.22	1.3956
335	0.208	1.3692
350	0.193	1.3254
370	0.16	1.2562
390	0.14	1.1858
410	0.135	1.1441
425	0.122	1.1057
445	0.117	1.0803
465	0.117	1.0516
480	0.11	1.0239
505	0.097	0.98136
530	0.105	0.87973
560	0.106	0.80771
590	0.092	0.77736
620	0.1	0.75186
660	0.09	0.73913
705	0.09	0.72169
750	0.09	1.4096
790	0.09	1.3956
810	0.09	1.3692
840	0.09	1.3254
465	0.25	1.2562
480	0.22	1.1858
505	0.208	1.1441
530	0.193	1.1057

Furnace Temperature (K)	Measured $c_{o(out)}/c_{o(in)}$	Calculated $c_{o(out)}/c_{o(in)}$
560	0.16	1.0803
590	0.092	1.0239
620	0.1	0.98136
660	0.09	0.87973
705	0.09	0.80771
750	0.09	0.77736
790	0.09	0.75186
810	0.09	0.73913
840	0.09	0.72169

Experiment C1: Comparison of measured and calculated ratios of centerline O-atom concentrations at various axial locations to that of the inlet at 80 % of maximum discharge power at a mass flow rate of 2300 sccm (87% O_2-13% Ar gas mixture), 300 K, and an outlet pressure of 466.63 Pa.

Distance from PMT2 (m)	**Measured $c_o/c_{o(in)}$**	**Calculated $c_{o(out)}/c_{o(in)}$**	**Calculated $c_{o(out)}/c_{o(in)}$ ($\gamma=7\times10^{-4}$)**	**Calculated $c_{o(out)}/c_{o(in)}$ (K2×2)**
0	1	1	1	1
0.205	0.84529	0.92022	0.81415	0.83867
0.43	0.7065	0.82029	0.60856	0.65334
0.66	0.45924	0.72518	0.44873	0.49804

Experiment C2: Comparison of measured and calculated ratios of centerline O-atom concentrations at various axial locations to that of the inlet at 80 % of maximum discharge power at a mass flow rate of 2300 sccm (87% O_2-13% Ar gas mixture), 300 K, and an outlet pressure of 346.6 Pa.

Distance from PMT2 (m)	**Measured $c_o/c_{o(in)}$**	**Calculated $c_{o(out)}/c_{o(in)}$**	**Calculated $c_{o(out)}/c_{o(in)}$ ($\gamma=1\times10^{-3}$)**	**Calculated $c_{o(out)}/c_{o(in)}$ (K2×5)**
0	1	1	1	1
0.205	0.86877	0.9646	0.85264	0.86122
0.43	0.73784	0.9198	0.68036	0.70517
0.66	0.53099	0.87595	0.53937	0.57061

Experiment C3: Comparison of measured and calculated ratios of centerline O-atom concentrations at various axial locations to that of the inlet at 80 % of maximum discharge power at a mass flow rate of 767 sccm (87% O_2-13% Ar gas mixture), 300 K, and an outlet pressure of 173.3 Pa.

Distance from PMT2 (m)	**Measured $c_o/c_{o(in)}$**	**Calculated $c_{o(out)}/c_{o(in)}$**	**Calculated $c_{o(out)}/c_{o(in)}$ ($\gamma=1\times10^{-3}$)**	**Calculated $c_{o(out)}/c_{o(in)}$ (K2×15)**
0	1	1	1	1
0.205	0.89652	0.95966	0.83094	0.8333
0.43	0.76348	0.91447	0.6659	0.67056
0.66	0.54616	0.87089	0.53119	0.53607

Experiment C4: Comparison of measured and calculated ratios of centerline O-atom concentrations at various axial locations to that of the inlet at 80 % of maximum discharge power at a mass flow rate of 767 sccm (87% O_2-13% Ar gas mixture), 300 K, and an outlet pressure of 346.6 Pa.

Distance from PMT2 (m)	**Measured $c_o/c_{o(in)}$**	**Calculated $c_{o(out)}/c_{o(in)}$**	**Calculated $c_{o(out)}/c_{o(in)}$ ($\gamma=3\times10^{-4}$)**	**Calculated $c_{o(out)}/c_{o(in)}$ (K2×2)**
0	1	1	1	1
0.205	0.78979	0.86624	0.79336	0.80124
0.43	0.65586	0.72084	0.59477	0.59788
0.66	0.45851	0.59276	0.43995	0.43556

Experiment C5: Comparison of measured and calculated ratios of centerline O-atom concentrations at various axial locations to that of the inlet at 80 % of maximum discharge power at a mass flow rate of 767 sccm (87% O_2-13% Ar gas mixture), 300 K, and an outlet pressure of 466.63 Pa.

Distance from PMT2 (m)	**Measured $c_o/c_{o(in)}$**	**Calculated $c_{o(out)}/c_{o(in)}$**
0	1	1
0.205	0.7152	0.70153
0.43	0.49189	0.43907
0.66	0.30904	0.26738

Oxidation

Experiment SI: Oxide thicknesses for oxidation of Si (100) as a function of time at 1183 K and 1323 K, 431.3 Pa outlet pressure, a flow rate of 2300 sccm (87 % O_2 and 13 % Ar), and 80 % discharge power.

1183 K			1323 K		
Time (min)	**Measured Oxide thickness (nm)**	**Calculated Oxide thickness (nm)**	**Time (min)**	**Measured Oxide thickness (nm)**	**Calculated Oxide thickness (nm)**
0	1.93	1.93	0	1.93	1.93
30	30.1	28.743	45	52.1	50.860
60	40	41.261	90	79.2	62.450
124	59.6	60.028	184	130.8	82.580
270	88.4	89.408	300	153.5	129.78
360	103.9	103.52			

Experiment SN: Oxide thicknesses for oxidation of LPCVD Si_3N_4 as a function of time at 1183 K and 1323 K, 431.3 Pa outlet pressure, a flow rate of 2300 sccm (87 % O_2 and 13 % Ar), and 80 % discharge power.

1183 K			1323 K		
Time (min)	**Measured Oxide thickness (nm)**	**Calculated Oxide thickness (nm)**	**Time (min)**	**Measured Oxide thickness (nm)**	**Calculated Oxide thickness (nm)**
0	1.93	1.93	0	0.0000	1.93
30	34.9	36.41	45	45.000	45.41
90	63.9	61.47	90	90.000	81.7
270	106.2	105.72	184	181.00	134.47
360	120.8	122	300	271.00	166

Experiment SC: Oxide thickness for oxidation of CVD SiC as a function of time at 1183 K, 431.3 Pa outlet pressure, a flow rate of 2300 sccm (87 % O_2 and 13 % Ar), and 80 % discharge power.

Time (min)	**Measured Oxide thickness (nm)**	**Calculated Oxide thickness (nm)**
0	1.93	1.93
30	44.5	37.2
90	69.5	64.39
270	113	111.56
360	123	128.83

REFERENCES

1. Santos, W.F.N. (2005) Flat-faced leading-edge effects in low-density hypersonic wedge flow. *Journal of Spacecraft and Rockets*, **42**, 22-29.

2. J.V. Rakich, D.A.S., M.J. Lanfranco (1982) Results of a flight experiment on the catalytic efficiency of the space shuttle heat shield. *AIAA/ASME 3rd Joint Thermophysics, Fluids, Plasma and Heat Transfer Conference*, St. Louis, Missouri, vol. 82-0944.

3. Tanaka, R. (2000) Research and development of ultra-high temperature materials in Japan (Reprinted from proceedings of High-Temperature Corrosion and Protection 2000). *Materials at High Temperatures*, **17**, 457-464.

4. Nguyen, Q. and Opila, E. (2004) Oxidation of ultra-high temperature ceramics in water vapor. *Abstracts of Papers of the American Chemical Society*, **227**, U1418-U1418.

5. Gasch, M., Ellerby, D., Irby, E., Beckman, S., Gusman, M. and Johnson, S. (2004) Processing, properties and arc jet oxidation of hafnium diboride/silicon carbide ultra high temperature ceramics. *Journal of Materials Science*, **39**, 5925-5937.

6. W. C. Tripp, H.H.D., and H. C. Graham (1973) Effect of an SiC addition on the Oxidation of ZrB2. *Ceramic Bulletin*, **52**, 612-616.

7. E. V. Clougherty, R.L.P., and L. Kaufman (1968) Synthesis of oxidation resistant metal diboride composites. *Transactions of the Mettalurgical Society of AIME*, **242**, 1077-1082.

8. Elizabeth J. Opilla, a.M.C.H. (2001) Oxidation of ZrB_2 - SiC. *Ceramic Engineering and Science Proceedings*, **22**, 221-229.

9. Fahrenholtz, W.G. (2007) Thermodynamic analysis of ZrB2-SiC oxidation: Formation of a SiC-depleted region. *Journal of the American Ceramic Society*, **90**, 143-148.

10. Opilla E. J., a.H.M.C. (2001) Oxidation of ZrB_2 - SiC. *Ceramic Engineering and Science Proceedings*, **22**, 221-229.

11. Deal, B.E. and Grove, A.S. (1965) General relationship for the thermal oxidation of silicon. *Journal of Applied Physics*, **36**, 3770.

12. Irene, E.A. (1983) Silicon oxidation studies - a revised model for thermal-oxidation. *Journal of Applied Physics*, **54**, 5416-5420.

13. Irene, E.A. (1978) Silicon oxidation studies: some aspects of initial growth regime. *Journal of Electrochemical Society*, **125**, 1708.

14. Doremus, R.H. (1984) Oxidation of silicon: strain and linear kinetics. *Thin Solid Films*, **122**, 191-196.

15. de Almeida, R.M.C., Goncalves, S., Baumvol, I.J.R. and Stedile, F.C. (2000) Dynamics of thermal growth of silicon oxide films on Si. *Physical Review B*, **61**, 12992-12999.

16. Stoneham, A.M., Grovenor, C.R.M. and Cerezo, A. (1987) Oxidation and the structure of the silicon-oxide interface. *Philosophical Magazine B-Physics of Condensed Matter Statistical Mechanics Electronic Optical and Magnetic Properties*, **55**, 201-210.

17. M. A. Hopper, R.A.C., and L. Young (1975) Thermal oxidation of silicon: In situ measurement of the growth rate using ellipsometry. *Journal of Electrochemical Society*, **122**, 1216.

18. Revesz, A.G., Mrstik, B.J., Hughes, H.L. and Mccarthy, D. (1986) Structure of SiO_2-films on silicon as revealed by oxygen-transport. *Journal of the Electrochemical Society*, **133**, 586-592.

19. Han, C.J.a.H., C. R. (1987) Parallel oxidation mechanism for Si oxidation in dry O_2. *Journal of Electrochemical Society*, **134**, 1297-1302.

20. Peeters, J. and Li, L. (1993) Oxidation of silicon in plasma afterglows - New model of oxide-growth including recombination of diffusing O-atoms. *Journal of Applied Physics*, **73**, 2477-2485.

21. Bongiorno, A. and Pasquarello, A. (2002) Energetics of oxygen species in crystalline and amorphous SiO_2: a first-principles investigation. *Solid-State Electronics*, **46**, 1873-1878.

22. Hoshino, T., Hata, M., Neya, S., Nishioka, Y., Watanabe, T., Tatsumura, K. and Ohdomari, L. (2003) Diffusion of molecular and atomic oxygen in silicon oxide. *Japanese Journal of Applied Physics Part 1-Regular Papers Short Notes & Review Papers*, **42**, 3560-3565.

23. Szymanski, M.A., Stoneham, A.M. and Shluger, A. (2001) The different roles of charged and neutral atomic and molecular oxidising species in silicon oxidation from Ab initio calculations. *Solid-State Electronics*, **45**, 1233-1240.

24. Tatsumura, K., Shimura, T., Mishima, E., Kawamura, K., Yamasaki, D., Yamamoto, H., Watanabe, T., Umeno, M. and Ohdomari, I. (2005) Reactions and diffusion of atomic and molecular oxygen in the SiO_2 network. *Physical Review B*, **72**, -.

25. Rosencher, E., Straboni, A., Rigo, S. and Amsel, G. (1979) An ^{18}O study of the thermal oxidation of silicon in oxygen. *Applied Physics Letters*, **34**, 254.

26. Rochet, F., Agius, B. and Rigo, S. (1984) An ^{18}O study of the oxidation mechanism of silicon in dry oxygen. *Journal of the Electrochemical Society*, **131**, 914-923.

27. Kimura, S.-i., Murakami, E., Warabisako, T., Mitani, E. and Sunami, H. (1988) An ^{18}O study of oxygen exchange phenomena during microwave-discharge plasma oxidation of silicon. *Journal of Applied Physics*, **63**, 4655.

28. Hoff, A.M. and Ruzyllo, J. (1988) Thermal oxidation of silicon in an afterglow gas. *Journal of the Electrochemical Society*, **135**, C135-C135.

29. Du, H.H., Houser, C.A., Tressler, R.E., Spear, K.E. and Pantano, C.G. (1990) Isotopic Studies of Oxidation of Si_3N_4 and Si Using Sims. *Journal of the Electrochemical Society*, **137**, 741-742.

30. Du, H.H., Tressler, R.E. and Spear, K.E. (1989) Thermodynamics of the Si-N-O system and kinetic modeling of oxidation of Si_3N_4. *Journal of the Electrochemical Society*, **136**, 3210-3215.

31. Du, H.H., Tressler, R.E., Spear, K.E. and Pantano, C.G. (1989) Oxidation studies of crystalline CVD silicon-nitride. *Journal of the Electrochemical Society*, **136**, 1527-1536.

32. Ogbuji, L.U.J.T. (1995) The SiO_2-Si_3N_4 Interface .2. O_2 permeation and oxidation reaction. *Journal of the American Ceramic Society*, **78**, 1279-1284.

33. Ogbuji, L.U.J.T. and Bryan, S.R. (1995) The SiO_2-Si_3N_4 Interface, 1. Nature of the interphase. *Journal of the American Ceramic Society*, **78**, 1272-1278.

34. Singhal, S.C. (1976) Thermodynamics and kinetics of oxidation of hot-pressed silicon-nitride. *Journal of Materials Science*, **11**, 500-509.

35. Ogbuji, L.U.T. and Jayne, D.T. (1993) Mechanism of incipient oxidation of bulk chemical vapor-deposited Si_3N_4. *Journal of the Electrochemical Society*, **140**, 759-766.

36. B. R. Rogers, Z.S., J. Marschall, N. Queraltó, and C. A. Zorman (2005) The effect of dissociated oxygen on the oxidation of Si, polycrystalline SiC and LPCVD Si_3N_4. . In *High Temperature Corrosion and Materials Chemistry V*. The Electrochemical Society Proceedings Series, Pennington, New Jersey.

37. Luthra, K.L. (1991) Some new perspectives on oxidation of silicon-carbide and silicon-nitride. *Journal of the American Ceramic Society*, **74**, 1095-1103.

38. Luthra, K.L. (1991) A mixed interface reaction diffusion control model for oxidation of Si_3N_4. *Journal of the Electrochemical Society*, **138**, 3001-3007.

39. Ogbuji, L.U.J.T. (1992) Role of Si_2N_2O in the passive oxidation of chemically-vapor-deposited Si_3N_4. *Journal of the American Ceramic Society*, **75**, 2995-3000.

40. Sheldon, B.W. (1996) Silicon nitride oxidation based on oxynitride interlayers with graded stoichiometry. *Journal of the American Ceramic Society*, **79**, 2993-2996.

41. Kennedy, G.P., Buiu, O. and Taylor, S. (1999) Oxidation of silicon nitride films in an oxygen plasma. *Journal of Applied Physics*, **85**, 3319.

42. Jimenez, C., Perriere, J., Vickridge, I., Enard, J.P. and Albella, J.M. (1991) Transformation of silicon-nitride in oxygen plasma. *Surface & Coatings Technology*, **45**, 147-154.

43. B. R. Rogers, Z.S., J. Marschall, N. Queraltó, and C. A. Zorman (2005) The effect of dissociated oxygen on the oxidation of Si, polycrystalline SiC and LPCVD Si_3N_4. In Opila, E. (ed.), *High Temperature Corrosion and Materials Chemistry*. Pennington, New Jersey, vol. V.

44. Wallace L. Vaughn, H.G.M. (1990) Active-to-passive transition in the oxidation of silicon carbide and silicon nitride in air. *Journal of American Ceramic Society*, **73**, 1540-1543.

45. Balat, M.J.H. (1996) Determination of the active-to-passive transition in the oxidation of silicon carbide in standard and microwave-excited air. *Journal of the European Ceramic Society*, **16**, 55.

46. Balat, M., Flamant, G., Male, G. and Pichelin, G. (1992) Active to passive transition in the oxidation of silicon-carbide at high-temperature and low-pressure in molecular and atomic oxygen. *Journal of Materials Science*, **27**, 697-703.

47. Goto, T. and Homma, H. (2002) High-temperature active/passive oxidation and bubble formation of CVD SiC in O-2 and CO2 atmospheres. *Journal of the European Ceramic Society*, **22**, 2749-2756.

48. Schneider, B., Guette, A., Naslain, R., Cataldi, M. and Costecalde, A. (1998) A theoretical and experimental approach to the active-to-passive transition in the oxidation of silicon carbide - Experiments at high temperatures and low total pressures. *Journal of Materials Science*, **33**, 535-547.

49. Wang, J.J., Zhang, L.T., Zeng, Q.F., Vignoles, G.L. and Guette, A. (2008) Theoretical investigation for the active-to-passive transition in the oxidation of silicon carbide. *Journal of the American Ceramic Society*, **91**, 1665-1673.

50. Berton, B., Bacos, M.P., Demange, D. and Lahaye, J. (1992) High-Temperature Oxidation of Silicon-Carbide in Simulated Atmospheric Reentry Conditions. *Journal of Materials Science*, **27**, 3206-3210.

51. Ogbuji, L.U.J.T. and Opila, E.J. (1995) A comparison of the oxidation-kinetics of SiC and Si_3N_4. *Journal of the Electrochemical Society*, **142**, 925-930.

52. Fox, D.S. (1998) Oxidation behavior of chemically-vapor-deposited silicon carbide and silicon nitride from 1200 degrees to 1600 degrees C. *Journal of the American Ceramic Society*, **81**, 945-950.

53. P Vaˇsina, V.K., A T´alsk´y, P Botoˇs, M Mr´azkov and and Mesko, M. (2004) Simultaneous measurement of N and O densities in plasma afterglow by means of NO titration. *Plasma Sources Science & Technology*, **13**, 668 - 674.

54. Bischel, W.K., Perry, B. E. and Crosley D. R. (1981) Two-photon laser-induced fluorescence in oxygen and nitrogen atoms. *Chemical Physics Letters*, **82**, 85-88.

55. Marschall, J. (1997) Experimental determination of oxygen and nitrogen recombination coefficients at elevated temperatures using laser-induced flouroscence. *AIAA Annual Conference*. American Institute of Aeronautics and Astronautics, Inc., pp. 97-3879.

56. Bischel, W.K., Perry, B.E. and Crosley, D.R. (1981) Two-Photon Laser-Induced Fluorescence in Oxygen and Nitrogen Atoms. *Chemical Physics Letters*, **82**, 85-88.

57. Bischel, W.K., Perry, B.E. and Crosley, D.R. (1982) Detection of Fluorescence from O and N atoms Induced by Two-Photon Absorption. *Applied Optics*, **21**, 1419-1428.

58. Niemi, K., Schulz-von der Gathen, V. and Dobele, H.F. (2005) Absolute atomic oxygen density measurements by two-photon absorption laser-induced fluorescence spectroscopy in an RF-excited atmospheric pressure plasma jet. *Plasma Sources Science & Technology*, **14**, 375-386.

59. Niemi, K., Schulz-von der Gathen, V. and Dobele, H.F. (2001) Absolute calibration of atomic density measurements by laser-induced fluorescence spectroscopy with two-photon excitation. *Journal of Physics D-Applied Physics*, **34**, 2330-2335.

60. Niemi, K., Gathen, V.S.-v.d. and Döbele, H.F. (2005) Absolute Atomic Oxygen Density Measurements by Two-Photon Absorption Laser-Induced Fluorescence Spectroscopy in an RF-Excited Atmospheric Pressure Plasma Jet. *Plasma Sources Science and Technology*, **14**, 375-386.

61. Herman, I.P. (1996) *Optical diagnostics for thin film processing*. Academic Press, Inc., San Diego.

62. Jackson, J.D. (1962) *Classical Electrodynamics*. John Wiley & Sons, New York.

63. Woollam, J.A.J., B D.; Herzinger, C M.; Hilfiker, J N.; Synowicki, R A.; Bungay, C L. (1999) Overview of variable-angle spectroscopic ellipsometry (VASE): I. Basic theory and typical applications. In Al-Jumaily, G.A. (ed.), *Optical Metrology*. SPIE, vol. CR72, pp. 3-28.

64. Leavitt, J.A., McIntyre, L.C., and Weller, M.R. (1995) Backscattering Spectrometry. In Nastasi, J.R.T.a.M.A. (ed.), *Handbook of modern ion beam materials analysis*. Material Research Society, Pittsburgh.

65. Weller, R.A. (1999) General Purpose Computational tools for Simulation and Analysis of Medium-Energy Backscattering Spectra. *Applications of Accelerators in Research and Industry*., 596-599.

66. Gartling, J.N.R.a.D.K. (2001) *The finite element method in heat transfer and fluid dynamics*. CRC Press LLC, New york.

67. Chopey, N.P. (2004) *Handbook of Chemical Engineering Calculations*. Mc-Graw Hill, New York.

68. Perry, R.H. (1997) *Perry's Chemical Engineering Handbook*. Mc-Graw Hill, New York.

69. R. C. Reid, J.M.P., and B. E. Poling (1987) *Properties of Gases & Liquids*. Mc-Graw Hill, New York.

70. Pallix, J.B. and Copeland, R.A. (1996) Measurement of catalytic recombination coefficients on quartz using laser-induced fluorescence. *Journal of Thermophysics and Heat Transfer*, **10**, 224-233.

71. Kaufman, F. (1961) Reactions of Atomic Oxygen. In Porter, G. (ed.), *Progress in Reaction Kinetics* Oxford: Pengamon vol. 1, pp. 1-39.

72. Baulch, D.L., Drysdale, D. D., Duxbury, J. and Grant, S. J. (1976) *Evaluated kinetic data for high temperature reactions.* Buttersworth, London-Boston.

73. Francis, P.D. (1969) The production of oxygen atoms in a microwave discharge and the recombination kinetics in a gas flow system. *Journal of Physics D: Applied Physics*, 1717.

74. Atkinson, R., Baulch D.L., Cox R.A., Crowley J.N., Hampson Jr. R.F., Kerr J.A., Rossi M.J., and Troe J. (2006) Summary of evaluated kinetic and photochemical data for atmospheric chemistry. IUPAC.

75. Berkowitz, J. (1968) *The structure and chemistry of solid surfaces*. John Wiley & Sons, Inc., New York.

76. Endo, H., Glanzer, K. and Troe, J. (1979) Shock-wave study of collisional energy-transfer in the dissociation of NO_2, O_3, and N_2O. *Journal of Physical Chemistry*, **83**, 2083-2090.

77. Greaves, J.C.a.L., J.W. (1959) Recombination of atoms at surfaces, Part 6 - Recombination of oxygen atoms on silica from 20 °C to 600 °C. *Transactions of the Faraday Society*, **55**, 1355 - 1361.

78. Heimerl, J.M. and Coffee, T.P. (1979) Unimolecular ozone decomposition reaction. *Combustion and Flame*, **35**, 117-123.

79. Hippler, H., Rahn, R. and Troe, J. (1990) Temperature and pressure dependence of ozone formation rates in the range 1--1000 bar and 90--370 K. *The Journal of Chemical Physics*, **93**, 6560.

80. Sander, S.P., Friedl, R.R., Golden, D.M., Kurylo, M.J., Huie, R.E., Orkin, V.L., Moortgat, G.K., Ravishankara, A.R., Kolb, C.E., Molina, M.J., and Finlayson-Pitts, B.J. (Feb 2003) Chemical kinetics and photochemical data for use in atmospheric studies: Evaluation number 14. JPL: California Institute of Technology.

81. Zimmerman, W.B.J. (2005) *Process Modelling and Simulation with Finite Element Methods.* World Scientific, New Jersey.

82. O.C. Zienkiewicz, R.L.T., and J.Z. Zhu (2005) *The finite element method, its basis & fundamentals*. Elsevier Butterworth-Heinemann, Burlington, MA.

83. Deuflhard, P. (1974) A modified Newton method for the solution of ill-conditioned systems of nonlinear equations with application to multiple shooting. *Numerische Mathematik*, **22**, 289.

84. Roache, P.J. (1998) *Verification and Validation in Computational Science and Engineering*. Hermosa Publishers, Albuquerque, New Mexico.

85. D. S. Hacker, S.A.M., and M. Steinberg (1961) Recombination of atomic oxygen on surfaces. *The Journal of Chemical Physics*, **35**, 1788-1792.

86. Boudart, Y.C.K.a.M. (1991) Recombination of O, N, and H atoms on silica: Kinetics and mechanism. *Langmuir*, **7**, 2999-3005.

87. Brovikova, I.N. and Rybkin, V.V. (1993) Temperature-dependence of the heterogeneous recombination probability for $\mathrm{O}^{\mathrm{P}}_{3}$ atoms on a quartz glass-surface. *High Energy Chemistry*, **27**, 324-326.

88. Gromov, A.R., Antipenko, E.E. and Strakhov, B.V. (1990) Kinetics of heterogeneous recombination of the oxygen and hydrogen-atoms on quartz. *Vestnik Moskovskogo Universiteta Seriya 2 Khimiya*, **31**, 245-251.

89. J. W. Linnett, F.R.S.a.D.G.H.M. (1956) The kinetics of the recombination of oxygen atoms at a glass surface. *Proceedings of the Royal Society of London, A*, **234**, 489-504.

90. Reeves, R.R., Mannella, G. and Harteck, P. (1960) Rate of Recombination of Oxygen Atoms. *The Journal of Chemical Physics*, **32**, 632.

91. Norton, F.J. (1962) Gas permeation through the vacuum envelope. *National symposium on vacuum technology transactions*, **8**, 8-16.

92. Hoshino, T., Hata, M., Neya, S., Nishioka, Y., Watanabe, T., Tatsumura, K. and Ohdomari, I. (2003) Probability of atomic or molecular oxygen species in silicon and silicon dioxide. *Japanese Journal of Applied Physics Part 1-Regular Papers Short Notes & Review Papers*, **42**, 6535-6542.

93. Hamann, D.R. (1998) Diffusion of atomic oxygen in SiO_2. *Physical Review Letters*, **81**, 3447-3450.

94. Uematsu, M., Kageshima, H. and Shiraishi, K. (2001) Simulation of wet oxidation of silicon based on the interfacial silicon emission model and comparison with dry oxidation. *Journal of Applied Physics*, **89**, 1948-1953.

95. Bishop, B.A. and Hogarth, C.A. (1967) Thermal Oxidation of silicon using wet oxygen. *International Journal of Electronics*, **22**, 455-&.

96. Doremus, R.H. (2004) Transport of oxygen in silicate glasses. *Journal of Non-Crystalline Solids*, **349**, 242-247.

97. J. R. Chelikowsky, D.J.C., and N. Binggeli (2000) Oxygen configurations in silica. *Physical Review B*, **62**, R2251 - R2254.

98. Song, Y., Dhar, S., Feldman, L.C., Chung, G. and Williams, J.R. (2004) Modified Deal Grove model for the thermal oxidation of silicon carbide. *Journal of Applied Physics*, **95**, 4953.

99. Barbalace, K. (1995-2008) Periodic Table of Elements - Oxygen – O. EnvironmentalChemistry.com.